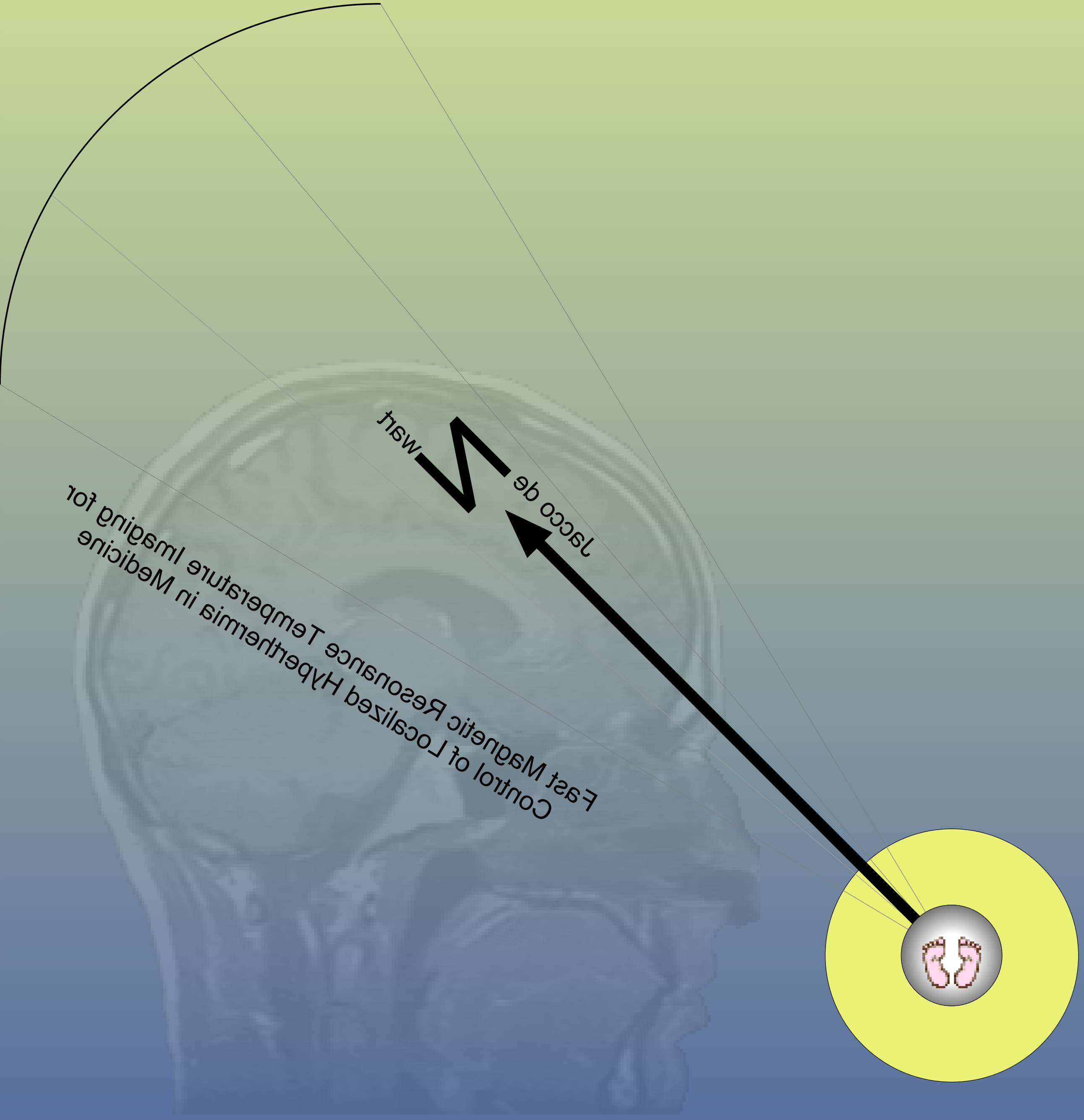
Jacco de Zwart
Fast Magnetic Resonance Temperature Imaging for Control of Localized Hyperthermia in Medicine

ISBN 90-393-2362-3

Fast Magnetic Resonance Temperature Imaging for Control of Localized Hyperthermia in Medicine

Jacco de Zwart

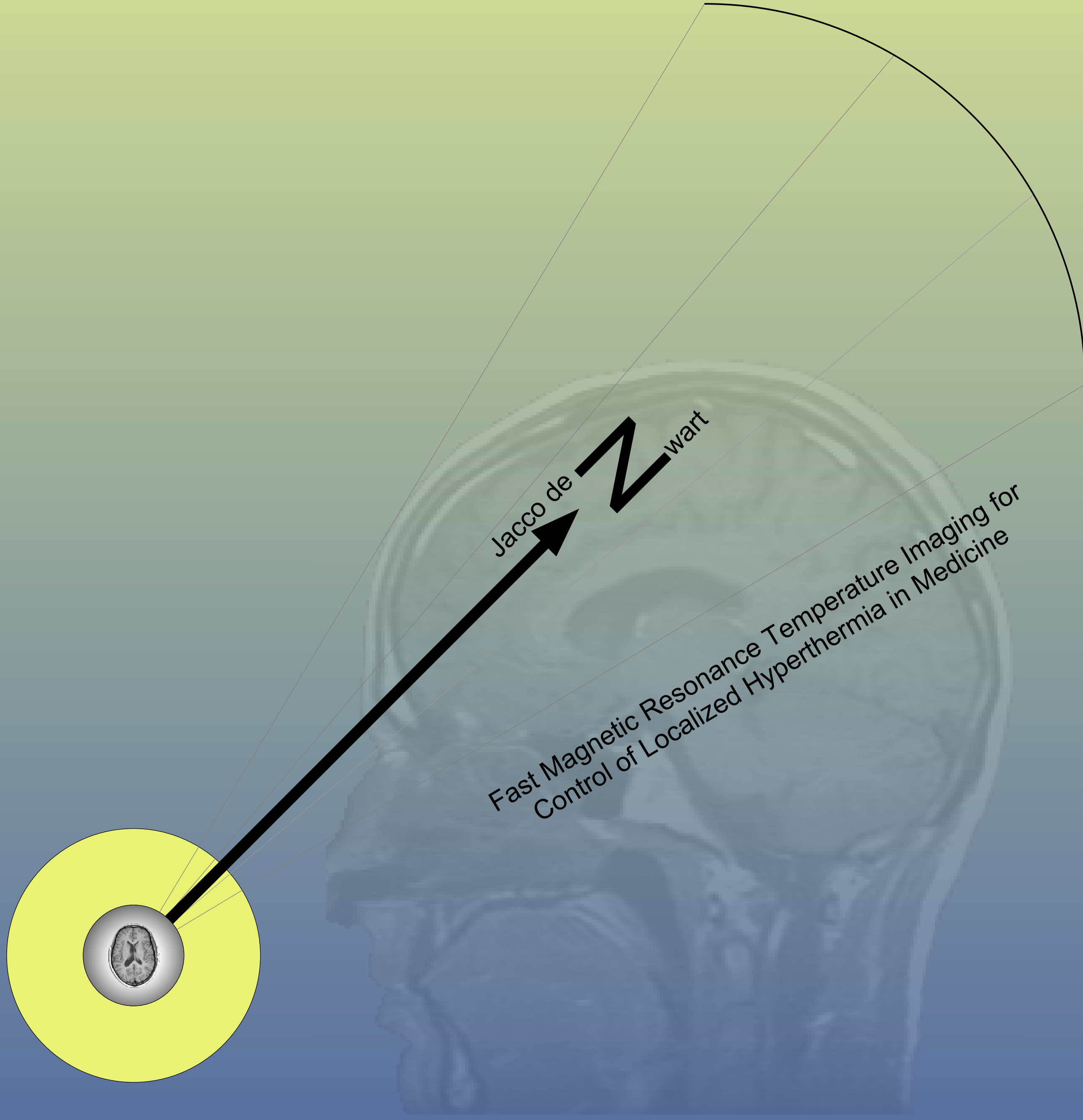

Jacco de Zwart

# Fast Magnetic Resonance Temperature Imaging for Control of Localized Hyperthermia in Medicine

Université Victor Segalen Bordeaux 2

Année 2000 Thèse n$^o$ 713

THESE

pour le

DOCTORAT DE L'UNIVERSITE BORDEAUX 2

Mention: Sciences Biologiques et Médicales
Option: Biologie-Santé

Présentée et soutenue publiquement le

4 février 2000

par

Jacobus Adrianus DE ZWART

# Fast Magnetic Resonance Temperature Imaging for Control of Localized Hyperthermia in Medicine

Membres du jury:

Prof. Jean-Marie CAILLE, Président
Prof. R. Mark HENKELMAN, Rapporteur
Dr. Michel DECORPS, Rapporteur
Dr. Chrit T.W. MOONEN
Prof. Max A. VIERGEVER
Prof. Paul CANIONI

© Jacco de Zwart, 1999/2000

No part of this work may be reproduced in any form or by any means without prior written permission of the author.

Cover: Gerda M. de Zwart - Minkman

ISBN 90-393-2362-3

# Fast Magnetic Resonance Temperature Imaging for Control of Localized Hyperthermia in Medicine

IRM Rapide de Température pour Contrôler
l'Hyperthermie Locale en Médecine

(avec un résumé en Français)

Snelle MR Temperatuurimaging voor Controle
van Gelocaliseerde Hyperthermie in de Geneeskunde

(met een samenvatting in het Nederlands)

Proefschrift
ter verkrijging van de graad van doctor aan de Universiteit Utrecht
op gezag van de Rector Magnificus, Prof.dr. H.O. Voorma,
ingevolge het besluit van het College voor Promoties
in het openbaar te verdedigen op
woensdag 24 mei 2000 des middags te 4:15 uur
door

Jacobus Adrianus de Zwart

geboren op 26 september 1971
te Rheden, Nederland

Promotor:

Prof.dr.ir. M.A. Viergever
Instituut voor Beeldwetenschappen, Faculteit der Geneeskunde, Universiteit Utrecht, Nederland

Co-promotor:

Dr.ir. C.T.W. Moonen
Résonance Magnétique des Systèmes Biologiques, Université Victor Segalen, Bordeaux, France

This thesis was made possible thanks to TMR Marie Curie Research Training Grant ERBFMBICT961733 from the European Commission.
Philips Medical Systems (Best, the Netherlands) and Nycomed Amersham (Nycomed Innovation AB, Malmö, Sweden) are greatfully acknowledged for financially supporting printing of this thesis.

In memory of my grandmother
Helena Johanna de Zwart - Neerings

# Contents

**Preface** **11**

**I Introduction** **13**

**1 Medical Applications of Hyperthermia** **15**
1.1 Medical potential of hyperthermia 16
1.2 Tissue ablation 17
1.3 Induction of transgene expression 18
1.4 Local drug delivery 20

**2 Introduction to MR Temperature Imaging** **25**
2.1 Magnetic resonance: a single nucleus 27
2.2 An ensemble of spins 27
2.3 MR thermometry 32
2.4 Comparison of MR thermometry methods 36

**3 Focused Ultrasound** **41**
3.1 Ultrasound properties 42
3.2 Focused ultrasound 43
3.3 FUS guidance 44

**II Methodology: Developments in MR Temperature Imaging** **47**

**4 Fast Temperature Imaging** **49**

**5 Lipid Suppression** **59**
5.1 Introduction 61
5.2 Materials and methods 61
5.3 Results and discussion 66
5.4 Conclusions 70

**6 Real-time Correction of Displacement** **75**
6.1 Introduction 77
6.2 Materials and methods 77
6.3 Results and discussion 83

6.4 Conclusions 90

**III Methodology: Controlling the Hyperthermia Procedure 93**

**7 FUS heating under MR Control 95**
7.1 Introduction 96
7.2 Materials and methods 96
7.3 Results 97
7.4 Discussion and conclusion 101

**8 MR-Controlled Hyperthermia Based on a Physical Model 103**
8.1 Introduction 104
8.2 Theory 104
8.3 Materials and methods 106
8.4 Results and discussion 108
8.5 Conclusion 112

**9 Implementation on a Clinical Scanner 115**
9.1 Introduction 116
9.2 FUS transducer and setup 116
9.3 MR sequences 116
9.4 Data handling 116
9.5 Heating trajectories 118
9.6 Discussion 119

**IV Applications: Tissue Ablation 121**

**10 On the Feasibility of On-Line Necrosis Prediction 123**
10.1 Introduction 124
10.2 Materials and methods 124
10.3 Results and discussion 127
10.4 Conclusion 127

**V Applications: Induction of Gene Therapy 131**

**11 Induction of gene expression 133**
11.1 Introduction 135
11.2 Methods 135
11.3 Results 137
11.4 Discussion 138

**12 Induction of Localized Exogenous Gene Expression In Vivo 141**
12.1 Introduction 142
12.2 Materials and methods 142
12.3 Results and discussion 144

12.4 Conclusion 147

VI Applications: Local Drug Delivery 153

13 Thermo-sensitive liposomes for local drug delivery 155
13.1 Introduction 156
13.2 Materials and methods 156
13.3 Results and discussion 157
13.4 Conclusions 158

VII Conclusion 161

14 Concluding Discussion 163
14.1 Temperature dependent magnetic susceptibility changes 165
14.2 Spatial and temporal resolution of temperature imaging 165
14.3 Phased-array FUS transducers 165

VIII Curriculum Vitae and Publications 167

Curriculum Vitae 169

Papers 171

Peer-Reviewed Abstracts 173

IX Summaries 175

Summary 177

Résumé 181

Samenvatting 185

# Preface

I want to start my thesis with an overview of all the people that made the past five years a success, not only from a scientific, but also from a personal point-of-view. Without direct and indirect contributions from a lot of people this thesis would not have its present form. Please ask friends and family for translations...

My girlfriend Anouk has certainly played an important role in the period in my life which led to this thesis. Anyone can imagine that it is not always easy to support a boyfriend that is living 1150 km away, but she did. Lieve Anouk, ik weet dat je het niet altijd even makkelijk had met zo'n "ver weg"-vriendje. Dit boekje sluit dat hoofdstuk in onze geschiedenis af moet je maar denken!

The man in charge of this project was of course Chrit Moonen. He was first twice my supervisor at the NIH, then my "directeur de thèse" in Bordeaux. Thanks not only for your contributions to this thesis, but also for simply being one of the nicest guys I know. En het blijft natuurlijk leuk om zo af en toe eens nederlands te kunnen praten!

Since the MR thermometry project originated at the NIH, some people there should be mentioned here. Peter van Gelderen was often subject to lots of questions. He was the helping hand with my physics/math problems (in praktijk getest met lemmings), which I guess is a field in which Wageningen-graduates lack important knowledge. After lunch there often was time for a Dutch "koffie pauze" with, apart from Peter, Sjef Duijn (Jeff Duyn), Chrit en Jan-Willem. Jeff provided the necessary physical exercise during the weekends, interrupted by pizza, concluded with BBQ. Alan Olson knows tons about MR electronics. He teams up with Scott Chesnick, who might hold the world record coil building, ready while you wait (no joke). I still use the towel, Daryl. After my return to Europe, the temperature project at NIH was for a while successfully carried on by David Madio.

7909 Tilbury St., Bethesda. Thanks to Josef, Carlo, Paolo, Nicolai, Andrea "pieno di aqua" and Marek "after-Jarka" for a great year. How top-level scientists and businessmen can change when they close the front door behind them...

Then, after seven months of temporary jobs involving ponds, plastic foil and jar-lids, printing paper bags and loading trucks, the story continues in Bordeaux, France. November 1996. My french: close to nothing. But, everybody at the RMSB remained patient and finally... ça marche! (allez un peu quand même) Grâce à tout l'RMSB j'ai appris la langue que j'ai détesté le plus à l'ecole... A great support during the first part of my stay in France was Sylvie, Chrit's wife, who stands at the basis of my decent French. The remaining very useful part of the language was supplied by Lionel, my neighbor at V1, and his friend "Max" (Rénald). Je suis encore convaincu que c'est "bonne" qu'il faut dire!

The name Fred (Frédéric) appears regularly in this thesis. He was not only the colleague with whom I worked most closely together, but in addition he became a friend. On était dans le même appart pendant 2 ans, d'abord avec Mario, maintenant avec Bixente, sans une seule dispute je pense (not even when I logged him out of jago to be able to play HalfLife with Mario recently). Xtof, with the help of Bruno and Eric, introduced me to the world of Bugs & Bruker. The experiments I've performed with Jean (and Fred) were a culinary adventure, the best meals of my life I've enjoyed next to a 1.5 T scanner. Since last year there's Rares "allez background", with him this project will fly high (n'oublies pas de m'inviter pour la fête quand tu gagneras un prix Nobel!), and Bruno, who joined the lab again, this time as Mr. RF. Nothing would be possible without the "big boss", Paul Canioni, and Catherine, la seule gestionnaire qui fait plus des heures par semaine qu'un PostDoc chinois.

Pierre Voisin, Antoine Vekris, Emanuelle Guilhon and Cédric Maurange are thanked for their help in gene-control experiments. They were responsible for the successful modification and implementation of tumors that were used for temperature-controlled local gene activation.

Max Viergever asked me in Philadelphia (ISMRM 1999) if it would interest me to defend my thesis a second time at Utrecht University in the Netherlands. My response was, a bit hesitant initially: YES! Bedankt voor je inzet om dit van de grond te krijgen en voor het vertrouwen in iemand die maar een beperkte tijd in je lab heeft doorgebracht. Het ziet er naar uit dat het gaat lukken, al is de "agreement" tussen Université Victor Segalen en de Universiteit Utrecht nog niet door Bordeaux ondertekend.

And, of course, Pa & Ma (mom & dad), Rob & Herma, Rogier, grandparents (including "Oma Zus"). Thanks for many kilo's of Dutch cheese, dropjes, haring, speculaas, pepernoten and I don't know what else I've received by mail or otherwise. Om over per caravan aangesleepte afgedankte stoelen en koelkasten maar niet te spreken. A whole Dutch invasion would every now and then come to Bordeaux to keep my Dutch alive: Roland (mien bruur) & Jolanda, Arnoud & Tamara, Enrico "'t is een groene", Mariska, Edwin, Tamara "mag ik nog effu belluh".

Philips in general is thanked for support, but special thanks go to Vic Hartog for providing custom-made software, and for his various visits to Bordeaux to boost the transfer of the thermometry software to the whole-body Philips scanner. Erik Dumont was an ongoing supply of Macintosh parts and software on his weekly visits (Je te dois une bouteille de vin au fait). Thanks to Jean Pergrale, Pierre Lelong and Maurice Gauchet for their beautiful FUS setup, and Mathias Fink for helpful discussions.

Jo Klaveness and Knut (whose last name is impossible to track down, Chrit wasted fax-messages, emails and telephone calls on this) from Nycomed/Oslo University in Norway are acknowledged for providing the temperature sensitive liposomes, and for incorporating them in gels.

Finally, this thesis was made possible thanks to generous support from the European Commission in the form of Marie Curie TMR grant ERBFMBICT961733.

Let's hope that some of the following will serve a purpose...

Jacco

# Part I

# Introduction

# Chapter 1

# Medical Applications of Hyperthermia

## Contents

**1.1 Medical potential of hyperthermia 16**

**1.2 Tissue ablation 17**

1.2.1 Mechanisms of cell death 17

1.2.2 The thermal dose concept 18

**1.3 Induction of transgene expression 18**

1.3.1 The heat-shock protein system 19

1.3.2 Hsp70 promoters 19

1.3.3 The hsp70 induction pathway 19

**1.4 Local drug delivery 20**

## 1.1 Medical potential of hyperthermia

Cancer remains a frequent cause of death, especially in the western world. Currently, surgery, chemotherapy and radiotherapy are generally employed to fight cancer. Depending on the location of the tumor, surgery is not always possible. Chemotherapy is often applied systemically, and most of the often toxic drugs used lack specificity, thus limiting the concentrations which can be applied. Even though localized radiotherapy can be achieved (e.g. $\gamma$-knife [1]), tissue damage in the beam path may occur.

Thermotherapy applications have been suggested for less-invasive surgery [2] as well as local delivery of therapeutic agents [3]. Less-invasive surgery will accelerate patient recovery, leading to cost-reduction of medical care and improving the quality of health care. Two potential applications of hyperthermia for local drug delivery have been suggested, increasing spatial and temporal control of chemotherapy. First, hyperthermia might provide a tool for local drug activation, e.g. gene therapy using a temperature sensitive promoter [4]. Second, it has been suggested for the control of local drug release, for example the induction of release from thermosensitive drug carriers [3].

Well controlled local hyperthermia is difficult to achieve in vivo. A number of devices capable of inducing localized hyperthermia have been proposed, based on either laser, radiofrequency, microwave or focused ultrasound (FUS). Since tissues are not homogeneous, heat delivery and distribution are difficult to anticipate. Heat flow in and around the target volume has been found to depend strongly on tissue composition and blood perfusion in and around the target region. A thermometry system which controls heat delivery is therefore essential. To allow accurate control of the heating procedure, volumetric temperature information about the zone surrounding the target should be available at a time-scale shorter than that of the heat diffusion processes.

Cell death depends non-linearly on the product of temperature and time, and can be predicted using the so-called “thermal dose” [5]. Reliable measurement of the applied thermal dose during treatment requires thermometry with an accuracy which should typically be on the order of 1°C. Measurement of the thermal dose can be used to monitor the progress of the intervention as well as to determine the exposure of surrounding healthy tissue. In addition, temperature monitoring allows assessment of the viability of healthy tissue surrounding the target area.

In the work described in this thesis, control of the hyperthermia intervention was achieved using magnetic resonance imaging (MRI). Magnetic resonance imaging provides target visualization with a high spatial resolution, and is temperature sensitive. Magnetic resonance (MR) temperature images were used to monitor temperature evolution in and around the target tissue. Based on the on-line analysis of MR data and subsequent feedback to the device which generates hyperthermia permitted control of temperature. In addition, various physiological parameters may be monitored directly (e.g. molecular diffusion [6]) or indirectly (for example through a change in relaxation time [7]) by MR, which may help to evaluate the intervention [8].

Hyperthermia was induced using focused ultrasound, which has two major advantages over laser- and RF-based hyperthermia devices. First, focused ultrasound is non-invasive, it is applied using an ultrasound source outside of the body. Second, the FUS focal point location within the tissue can be modified either mechanically or electronically, facilitating coverage of arbitrarily-shaped or larger target volumes. The size of the FUS focal point is on the order of a few millimeters, depending on the transducer and ultrasound frequency used (see chapter 3), thus allowing hyperthermia with a high spatial resolution.

In this thesis, methods are presented which improve the quality and reliability of MR thermometry. In addition, control of the hyperthermia procedure on the basis of on-line analyzed MR temperature images is described. Feasibility studies of three potential localized hyperthermia applications were performed, respectively thermal ablation of tissue, control of gene activation, and control of local drug release. These three applications will be introduced in the remainder of this chapter. In the second and third chapter of the introduction, magnetic resonance temperature imaging and focused ultrasound are introduced.

## 1.2 Tissue ablation

### 1.2.1 Mechanisms of cell death

Elevated tissue temperature leads to cell death, depending on both temperature and duration of the hyperthermia. The mechanisms of cell killing due to hyperthermia are less clear than due to for example ionizing radiation, where DNA damage is the most important effect leading to cell death [9]. At molecular and metabolic level, heat predominantly induces two effects [10]. It leads to conformational changes and destabilization of macromolecules and multi-molecular structures. Conformation is generally essential for the biological activity of macromolecules.

The conformation of DNA is irreversibly changed only at temperatures far above those leading to cell death [11]. However, disturbances of protein conformation have been shown to occur in temperature ranges which are near to or overlapping with those leading to cell death [12, 13]. The conformation of biological macromolecules depends on covalent bonds, hydrogen bridges, electrical interactions of ionic groups and hydrophilic/hydrophobic interactions. These last two classes of interactions are relatively weak and can be altered easily, for example by an increase in temperature.

Protein conformation strongly depends on the pH-value, since the pH-value determines whether various ionic groups exist in protonated or deprotonated state [14]. Quite a number of groups which stabilize protein conformation by ionic interactions have pK-values (which are temperature dependent) near the pH of the cellular compartment in which they reside. Therefore, a change in temperature will also alter the protonation, and thus influence these interactions.

Finally, the stability and function of biological membranes is influenced by their “fluidity”. Temperature changes increase the fluidity of biological membranes, also playing a role in cellular killing [15].

Cell death occurs through either necrosis or apoptosis. In contrast to necrosis, apoptosis is not a passive phenomenon, but is gene-directed, usually requiring ongoing protein synthesis [16]. Although the thermosensitivity of apoptotic induction varies from cell type to cell type, apoptotic cell death occurs at temperatures lower than those inducing necrosis [17]. Apoptosis can be morphologically characterized by shrinkage of cellular contents within their membranes and condensation of chromatin [18], while necrosis induces swelling of the cells and their organelles, leading to disruption of the cell membrane.

### 1.2.2 The thermal dose concept

The relation between cell death and temperature has been found to be strongly non-linear. Sapareto and Dewey have presented an empirical model which allows the effect of a given temperature-time trajectory to be estimated. This model has led to the concept of "thermal dose" [5]. Based on data from literature, the authors found that the majority of biological systems exhibit approximately the same exponential relationship between cell death, time and temperature:

$$\begin{aligned} t_{eq,T_r} &= \int_0^t R^{T_r - T(t)} dt \qquad (1.1) \\ where: \ & R = 0.25 \ \ (T < 43°C) \\ & R = 0.50 \ \ (T > 43°C) \end{aligned}$$

Equation 1.1 is used to calculate the equivalent time of exposure, $t_{eq,T_r}$, at temperature $T_r$ for an arbitrary temperature evolution in time, $T(t)$. This does not imply that all cells exhibit the same sensitivity to heat, but only that a consistent relationship between time and temperature was found for many cell types. An equivalent time of 240 minutes at 43°C is often used as a threshold for tissue necrosis [19].

## 1.3 Induction of transgene expression

One possible strategy for achieving local drug delivery is gene therapy, where the desired protein is synthesized at the target location. For tumor treatment, gene therapy based on the expression of a suicide gene, like thymidine kinase [20], or immuno-stimulating proteins, like TNF-$\alpha$ [21], have been suggested.

However, one of the major difficulties in the development of gene therapy is the spatial and temporal control of gene expression [22]. Spatial control of gene delivery can be accomplished using cellular targeting strategies [23], but these require the availability of cell surface receptors which are typical for the target cell type [24].

Even when delivery of the gene to the target site has been realized, temporal control of its expression remains difficult. Physical activation of gene expression has been proposed based on $\gamma$-radiation in combination with the EGR-1 promoter [21, 25]. Targeting was obtained by either radiotherapy or by systemic injection of radioisotopes that accumulate in the tumor. The use of hyperthermia for the induction of gene expression under control of a thermosensitive promoter has recently been suggested [4]. A heat-shock protein (hsp) promoter appears to be a good candidate for thermally-induced gene therapy, since the heat-shock protein system is highly conserved between organisms and is activated at temperatures a few degrees above body temperature. Induction of endogenous hsp70 (a 70 kDa heat-shock protein) in a small volume within muscle has been demonstrated in vivo [4] (see chapter 11), using focused ultrasound to induce hyperthermia. Expression of suicide genes under control of the hsp70-promoter has been accomplished in prostate carcinoma cells [26]. Initial experiments have shown the feasibility of in situ activation of such a construct [27].

### 1.3.1 The heat-shock protein system

Heat shock proteins are found in every organism, and the hsp-system is highly conserved. For example, hsps from the bacteria *E. Coli* and human cells exhibit as much as 50% sequence identity [28]. Some members of the hsp-family are expressed constitutively and appear to be involved as chaperones in basic cellular processes such as protein synthesis and maturation, assembly of protein complexes, and intracellular trafficking. Others are normally silent or are expressed at low levels. Expression of the latter genes is enhanced when cells are subject to stressful conditions such as elevated temperature or the presence of toxic substances [28].

The 70 kDa family of hsps (hsp70) is the most abundant and conserved subset of eukaryotic stress proteins. Hsp70 is the major inducible heat-shock protein found in all living cells [29]. Following heat shock, its synthesis increases to a point where it becomes the most abundant single protein in a cell. Hsp70 is synthesized in response to heat, heavy metals, toxins and ischemia [30].

Induction of hsp mRNA (messenger ribonucleic acid) occurs very rapidly and is detectable within minutes of heat exposure [31]. In vivo experiments strongly suggest that heat treatment enhances the transcriptional activity of hsp genes [32, 33], which in large part accounts for the drastic increase in hsp mRNA-levels.

### 1.3.2 Hsp70 promoters

The major components of the transcriptional mechanism for heat regulation of hsp-genes are highly conserved. Heat activation of a *Drosophila* hsp70 gene, introduced in mammalian cells, occurred at the same temperature at which mammalian genes were activated, rather than at the *Drosophila* activation temperature. This suggests that the introduced *Drosophila* gene was regulated by the same mechanisms that control endogenous hsp in the mammalian cell [28].

Fig. 1.1a shows the minimal *Drosophila* hsp70 promoter [28]. Only three elements are known to be essential for its function, two heat shock elements, HSEI and HSEII, and a so-called TATA-box. The heat shock elements are binding sites for heat shock transcription factor, HSF. It was found that deletion of either of the heat shock elements reduced promoter activity in heat-treated cells by 90% or more [34]. TATA-like elements bind RNA-polymerase, thus indicating where transcription is started. The simplicity of this promoter made it the ideal model system to determine the elements that are essential for its functioning. Cooperative binding interactions between a promoter element and heat shock factor (see below) seem to play a role in the regulation of promoter activity in the cell, as was suggested by in vitro studies [35, 36].

The promoter of human hsp70 genes has been intensively studied. The non-constitutive minimal hsp70-promoter is strictly heat-regulated, its base-sequence is shown in Fig. 1.1b [28]. Its transcripts are prominent in heat-stressed cells, but barely detectable in unstressed cells [37]. Deletion analysis suggests that the activity of the promoter depends on the presence of at least two of the three HSE-sequences [38] (see Fig. 1.1b). Heat-stress was found to increase expression by up to several thousand fold [39].

### 1.3.3 The hsp70 induction pathway

At least three distinct heat shock factors (HSFs) have been found in higher vertebrates [40]. The role of HSF1 in the induction of hsp gene expression is described here. In non-stressed cells, the transcription factor is kept in an inactive form by the association of one or more members

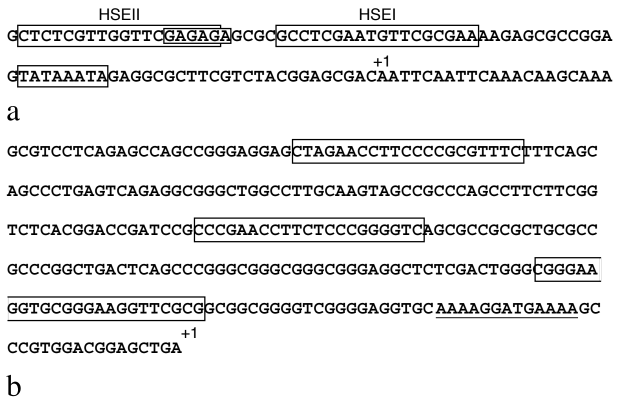
HSEII
HSEI
GCTCTCGTTGGTTCGAGAGAGCGCGCCTCGAATGTTCGCGAAAAGAGCGCCGGA
+1
GTATAAATAGAGGCGCTTCGTCTACGGAGCGACAATTCAATTCAAACAAGCAAA
a
GCGTCCTCAGAGCCAGCCGGGAGGAGCTAGAACCTTCCCCGCGTTTCTTTCAGC
AGCCCTGAGTCAGAGGCGGGCTGGCCTTGCAAGTAGCCGCCCAGCCTTCTTCGG
TCTCACGGACCGATCCGCCCGAACCTTCTCCCGGGGTCAGCGCCGCGCTGCGCC
GCCCGGCTGACTCAGCCCGGGCGGGCGGGCGGGAGGCTCTCGACTGGGCGGGAA
GGTGCGGGAAGGTTCGCGGCGGCGGGGTCGGGGAGGTGCAAAAGGATGAAAAGC
+1
CCGTGGACGGAGCTGA
b

Figure 1.1: *a) The base sequence of the minimal Drosophila hsp70 promoter, containing HSEII, HSEI, and TATA elements (boxed). +1 refers to the transcription start site. b) Nucleotide sequence of the human hsp70B promoter. HSE-sequences are boxed, the region normally occupied by a TATA-like element is underlined. See text for details.*

of the hsp70-family with HSF1. Although no evidence of a stable complex between hsp70 or hsc70 (constitutive hsp70) and the inactive form of HSF1 has been reported, it has been shown that exogenous hsp70 inhibits activation of HSF1 in vitro [41].

Heat shock causes unfolding and denaturation of proteins. The unfolded proteins bind to hsc70, thus reducing the concentration of free hsc70 in the cytoplasm. This change in concentration in cytoplasm causes depletion of the nuclear hsc70-pool, which causes dissolving of hsc70/HSF1-complexes, thus leading to activation of HSF1. HSF1 forms trimers, which accumulate in the nucleus [40] and bind to the heat shock element (HSE) in the promoter of the heat shock gene, thus activating gene expression.

## 1.4 Local drug delivery

In chemotherapy, a drug is frequently administered systemically. Since anti-cancer drugs often have a low specificity and toxic side-effects, its efficacy is limited. Local drug release increases the drug concentration locally and limits toxic side-effects. Liposomes, microscopic particles of lipid bilayer membrane that enclose aqueous internal compartments, have been suggested as a drug delivery system. Liposome membranes are composed of amphipathic lipids, identical to those in cell membranes. Therefore, hydrophilic drugs can be encapsulated in the aqueous internal chambers and hydrophobic drugs in the lipid bilayer.

The use of liposomes as pharmacological capsules has however been limited by the inability to direct them to the target site. Much of the effort in liposome research has therefore been directed at tumor targeting [42]. Attachment of specific antibodies or other proteins to the liposome surface may be used for specific targeting [43, 44]. An alternative is the use of local hyperthermia in combination with heat sensitive liposomes to increase drug release within the tumor, as was first suggested two decades ago [3].

Lipid bilayer membranes become “leaky” when they pass through their liquid-crystalline phase transition temperature ($T_c$), which depends on the composition of the bilayer membrane.

At temperatures well below their $T_c$, liposomes are relatively stable, but as $T_c$ is approached the phase transition of its membrane renders them leaky for small molecules. Liposomes with a $T_c$ a few degrees above body temperature can therefore be used for local drug delivery if the target zone is locally heated.

Well controlled localized hyperthermia might thus provide both spatial and temporal control of local drug release from thermosensitive liposomes.

## References

[1] D.G. Leksell, Stereotactic radiosurgery. Present status and future trends. *Neurol. Res.* **9**, 60-68 (1987)

[2] F.J. Fry, F. Dunn, Tumor irradiation with intense ultrasound. *Ultrasound Med. Biol.* **4**, 337-341 (1978)

[3] J.N. Weinstein, R.L. Magin, M.B. Yatvin, D.S. Zaharko, Liposomes and local hyperthermia: selective delivery of methotrexate to heated tumors. *Science* **204**, 188-191 (1979)

[4] D.P. Madio, P. van Gelderen, D. DesPres, A. Olson, J.A. de Zwart, T.W. Fawcett, N.J. Holbrook, M. Mandel, C.T.W. Moonen, On the feasibility of MRI-guided focused ultrasound for local induction of gene expression. *J. Magn. Res. Imaging* **8**, 101-104 (1998)

[5] S.A. Sapareto, W.C. Dewey, Thermal dose determination in cancer therapy. *Int. J. Radiation Oncology Biol. Phys.* **10**, 787-800 (1984)

[6] D. Le Bihan, R. Turner, C.T. Moonen, J. Pekar, Imaging of diffusion and microcirculation with gradient sensitization: design, strategy, and significance. *J. Magn. Reson. Imaging* **15**, 7-28 (1991)

[7] P.A. Bottomley, T.H. Foster, R.E. Argersiger, L.M. Pfeifer, A review of normal tissue hydrogen NMR relaxation times and relaxation mechanisms from 1-100 MHz: dependence on tissue type, NMR frequency, temperature, species, excision, and age. *Med. Phys.* **11**, 425-447 (1984)

[8] S.J. Graham, G.J. Stanisz, A. Kecojevic, M.J. Bronskill, R.M. Henkelman, Analysis of changes in MR properties of tissues after heat treatment. *Magn. Reson. Med.* **42**, 1061-1071 (1999)

[9] T. Alpher, Cellular radiobiology, Cambridge University Press, Cambridge (1979)

[10] C. Streffer, Metabolic changes during and after hyperthermia. *Int. J. Hyperthermia* **1**, 305-319 (1985)

[11] J.R. Lepock, Protein denaturation: its role in thermal killing. In: W.C. Dewey, M. Eddington, R.J.M. Fry, E.J. Hall, G.F. Whitmore (eds), Radiation research: a twentieth-century perspective. Academic press, New York, 992-998 (1991)

[12] P.L. Privalov, Stability of proteins. *Adv. Protein Chem.* **33**, 167-241 (1979)

[13] J.R. Lepock, Involvement of membranes in cellular responses to hyperthermia. *Radiat. Res.* **92**, 433-438 (1982)

[14] C. Streffer, Reaktivität und Struktur von Aminosäuren und Proteinen (Cystein und β-Galaktosidase). Dissertation, Universität Freiburg (1963)

[15] M.B. Yatvin, The influence of membrane lipid composition and procaine on hyperthermic death of cells. *Int. J. Radiat. Biol.* **32**, 513-521 (1977)

[16] M.R. Allison, C.E. Sarraf, Apoptosis: a gene-directed programme of cell death. *J. R. Coll. Physicians Lond.* **26**, 25-35 (1992)

[17] T. Honma, [Characteristics of hyperthermia-induced apoptotic cell death.] (in japanese) *Nippon Rinsho* **54**, 1949-1954 (1996)

[18] M.J. Edwards, Apoptosis, the heat shock response, hyperthermia, birth defects, disease and cancer. Where are the common links? *Cell Stress Chaperones* **3**, 213-220 (1998)

[19] D.R. Daum, K. Hynynen, Thermal dose optimalization via temporal switching in ultrasound surgery. *IEEE Trans. Ultrason., Ferroelect., Freq. Contr.* **43**, 208-215 (1998)

[20] A.J. Vincent, R. Vogels, G.V. Someren, M.C. Esandi, J.L. Noteboom, C.J. Avezaat, C. Vecht, D.W. Bekkum, D. Valerio, A Bout, P.M. Hoogerbrugge, Herpes simplex virus thymidine kinase gene therapy for malignant brain tumors. *Gene Ther.* **7**, 197-205 (1996)

[21] D.E. Hallahan, H.J. Mauceri, L.P. Seung, E.J. Dunphy, J.D. Wayne, N.N. Hanna, A. Toledano, S. Hellman, D.W. Kufe, R.R. Weichselbaum, Spatial and temporal control of gene therapy using ionizing radiation. *Nature Medicine* **1**, 786-791 (1995)

[22] R.G. Crystal, Transfer of genes to humans: early lessons and obstacles to success. *Science* **270**, 404-410 (1995)

[23] D.D. Spragg, D.R. Alford, R. Greferath, C.E. Larsen, K.D. Lee, G.C. Gurtner, M.I. Cybulsky, P.F. Tosi, C. Nicolau, M.A. Gimbrone, Immunotargeting of liposomes to activated vascular endothelial cells: a strategy for site-selective delivery in the cardiovascular system. *PNAS* **94**, 8795-8800 (1997)

[24] M.A. Barry, W.J. Dower, S.A. Johnston, Toward cell-targeting gene therapy vectors: selection of cell-binding peptides from random peptide-presenting phage libraries. *Nat. Med.* **2**, 299-305 (1996)

[25] T. Takahashi, Y. Namiki, T. Ohno, Induction of suicide HSV-TK gene by activation of egr-1 promoter with radioisotopes. *Hum. Gene Ther.* **8**, 827-833 (1997)

[26] R.V. Blackburn, S.S. Galoforo, P.M. Corry, Y.J. Lee, Adenoviral-mediated transfer of a heat-inducible double suicide gene into prostate carcinoma cells. *Cancer Res.* **58**, 1358-1362 (1998)

[27] A. Vekris, C. Maurange, C. Moonen, F. Mazurier, H. De Verneuil, P. Canioni, P. Voisin, Control of transgene expression using local hyperthermia in combination with a heat-sensitive promoter. *J. Gene Medicine*, [in press]

[28] R. Voellmy, Transduction of the stress signal mechanisms of transcriptional regulation of heat shock/stress protein gene expression in higher eukaryotes. *Critical Reviews in Eukaryotic Gene Expression* **4(4)**, 357-401 (1994)

[29] M.A. Yenari, S.L. Fink, G.H. Sun, L.K. Chang, M.K. Patel, D.M. Kunis, D. Onley, D.Y. Ho, R.M. Sapolsky, G.K. Steinberg, Gene therapy with hsp72 is neuroprotective in rat models of stroke and epilepsy. *Ann. Neurol.* **44**, 584-591 (1998)

[30] W.J. Welch, C.R. Brown, Influence of molecular and chemical chaperones on protein folding. *Cell Stress Chaperones* **1**, 109-115 (1996)

[31] R.C. Findly, T. Pederson, Regulated transcription of the genes for actin and heat shock protein in cultured *Drosophila* cells. *J. Cell. Biol.* **88**, 231 (1981)

[32] J. Vazquez, D. Pauli, A. Tissieres, Transcriptional regulation in *Drosophila* during heat shock: a nuclear run-on analysis. *Chromosoma* **102**, 233 (1993)

[33] D.D. Mosser, N.G. Theodorakis, R.I. Morimoto, Coordinate changes in heat shock element binding activity and hsp70 gene transcription rates in human cells. *Mol. Cell. Biol.* **8**, 4736 (1988)

[34] J. Amin, R. Mestril, P. Schiller, M. Dreano, R. Voellmy, Organization of the *Drosophila melanogaster* hsp70 heat shock regulation unit. *Mol. Cell. Biol.* **5**, 197 (1985)

[35] J. Topol, D.M. Ruden, C.S. Parker, Sequences required for in vitro transcriptional activation of a *Drosophila* hsp70 gene. *Cell* **42**, 527-, (1985)

[36] H. Xiao, O. Perisic, J.T. Lis, Fine structure analysis of the *Drosophila* heat shock factor to arrays of a conserved 5bp unit. *Cell* **64**, 585- (1991)

[37] R. Voellmy, A. Ahmed, P. Schiller, P. Bromley, D. Rungger, Isolation and functional analysis of a human 70,000 dalton heat shock protein segment. *Proc. Natl. Acad. Sci. U.S.A.* **82**, 4949 (1985)

[38] P. Schiller, J. Amin, J. Ananthan, M.E. Brown, W.A. Scott, R. Voellmy, Cis-acting elements involved in the regulated expression of a human hsp70 gene. *J. Mol. Biol.* **203**, 97 (1988)

[39] M. Dreano, J. Brochot, A. Meyers, C. Cheng-Meyer, D. Rungger, R. Voellmy, P. Bromley, High-level, heat-regulated synthesis of proteins in eukaryotic cells. *Gene* **49**, 1 (1986)

[40] R.J. Mayer, I.R. Brown (editors), Heat shock proteins in the nervous system. Academic Press, ISBN 0-12-480960-X (1994)

[41] K. Abravaya, M.P. Myers, S.P. Murphy, R. Morimoto, The human heat shock protein hsp70 interacts with HSF, the transcription factor that regulates heat shock-gene expression. *Genes & Devel.* **6**, 1153-1164 (1992)

[42] S. Kim, Liposomes as carriers of cancer chemotherapy: current status and future prospects. *Drugs* **46**, 618-638 (1993)

[43] A. Rahman, M. Panneerselvam, R. Guirguis, V. Castronovo, M.E. Sobel, K. Abraham, P.E. Daddona, L.A. Liotta, Anti-laminin receptor antibody targeting of liposomes with encapsulated doxorubicin to human breast cancer cells in vitro. *J. Natl. Cancer Inst.* **81**, 1794-1800 (1989)

[44] M. Singh, T. Ghose, M. Mezei, P. Belitsky, Inhibition of human renal cancer by monoclonal antibody targeted methotrexate-containing liposomes in an ascites tumor model. *Cancer Letters* **56**, 97-102 (1991)

# Chapter 2

# Introduction to MR Temperature Imaging

## Contents

**2.1 Magnetic resonance: a single nucleus** **27**

**2.2 An ensemble of spins** **27**

- 2.2.1 Selective excitation 28
- 2.2.2 Acquisition of an image 29
- 2.2.3 Relaxation 30
- 2.2.4 Signal intensity 31

**2.3 MR thermometry** **32**

- 2.3.1 Temperature dependence of the diffusion constant 33
- 2.3.2 Temperature dependence of $T_1$ relaxation time 34
- 2.3.3 Temperature dependence of water proton resonance frequency 35

**2.4 Comparison of MR thermometry methods** **36**

The basic principles underlying nuclear magnetic resonance (NMR) and its imaging offspring, magnetic resonance imaging (MRI), will be discussed only briefly in this thesis. For more information, the reader is kindly referred to "Basics of Magnetic Resonance Imaging" by Oldendorf [1] (basic level) or Callaghan's "Principles of Nuclear Magnetic Resonance Microscopy" [2] (higher level).

## 2.1 Magnetic resonance: a single nucleus

Depending on the number of neutrons and protons of which it is composed, a nucleus can have a net spin, its spin quantum number, $I$, is non-zero. The rotation of a nucleus with non-zero spin quantum number generates a magnetic dipole around its rotation axis, called nuclear magnetic moment ($\vec{\mu}$). In quantum mechanical terms, this magnetic moment can align in only $2I+1$ ways with an external magnetic field, the magnetic moment can only occupy discrete states which have different energy levels. For hydrogen ($^1$H), a nucleus with spin $\frac{1}{2}$, only two spin states exist. The energy difference between the lower and higher level, $\Delta E$, depends on the gyromagnetic ratio ($\gamma$) of the nucleus and the strength of the local magnetic field $B_0$:

$$\Delta E = \frac{\gamma h B_0}{2\pi} \tag{2.1}$$

where $h$ is Plancks constant. The gyromagnetic ratio is an unique value for each nucleus, which depends on $\vec{\mu}$ and $I$:

$$\gamma = \frac{2\pi\vec{\mu}}{hI} \tag{2.2}$$

The rotation-axis of the spinning nucleus will precess around the magnetic field lines. The frequency of this precession motion depends on the strength of the magnetic field and the gyromagnetic ratio of the nucleus:

$$\omega_0 = \gamma B_0 \tag{2.3}$$

where $\omega_0$ the frequency of precession, called Larmor frequency.

## 2.2 An ensemble of spins

The magnetic resonance experiment exploits the unequal distribution of spins between the spin-states which correspond to the different alignments of the magnetic moment $\vec{\mu}$ with respect to the external magnetic field. For spin-$\frac{1}{2}$ nuclei, the relative population of the two existing spin-states is determined by the Boltzmann-distribution:

$$\frac{n_2}{n_1} = e^{-\frac{\Delta E}{kT}} \tag{2.4}$$

where $k$ is the Boltzmann constant and $\Delta E$ the energy difference between the two states, given by Eq. 2.1. Since $\Delta E$ increases linearly with the magnetic field, the population difference between the two spin states increases with the strength of the magnetic field.

In living tissue, water hydrogen spins represent the largest group of MR-observable nuclei. Hydrogen spins in water behave largely independently. Even though the orientation of a single atomic nucleus in a magnetic field is one of a discrete set of possibilities, in most aspects of the MR experiment the group of nuclei under observation appears to behave continuously, so called ensemble behavior. The behavior of an ensemble of spin-$\frac{1}{2}$ nuclei in an MR experiment can be described from a "classical" point of view. The net magnetization of an ensemble of spin-$\frac{1}{2}$ nuclei can be represented by a magnetization vector.

The Boltzman distribution is disturbed when energy is absorbed by the spin system. A disturbance with frequency $\omega_0$ will cause a proton to change to another spin state. E.g. a spin-$\frac{1}{2}$ nucleus "flips" from the low energy state, where its magnetic moment aligns with the magnetic field, to the higher energy state, where it opposes the $B_0$-field. Since in equilibrium state a larger fraction of the spins occupies the lower energy level (see Eq. 2.4), more spins will be excited to the higher energy state than down to the lower energy level. If irradiation continues, the population occupying the higher energy level approaches the population of the lower energy level. If population of both levels is equal ($n_1$=$n_2$) the spin system is saturated, no net change of populations is induced upon disturbance.

From the classical viewpoint, the resonance phenomenon occurs when a magnetic field ($B_1$), perpendicular to the $B_0$-field and oscillating at frequency $\omega_0$, is applied. The perpendicular field is generally produced by application of a short burst of resonant RF-field (short with respect to MR relaxation processes) to a transmission coil. In the presence of $B_1$, the magnetization will precess simultaneously about the main magnetic field $B_0$ with frequency $\omega_0$, and about the perpendicular RF-field $B_1$ with frequency $\omega_1$, where $\omega_1 = \gamma_H B_1$.

When the oscillation frequency of the $B_1$-field is not equal to $\omega_0$ (off-resonance excitation), the effective $B_1$-field ($B_{eff}$) is no longer perpendicular to the $B_0$-field, the longitudinal component is no longer zero but has the value ($B_0$-$\omega/\gamma$). In this case, $B_{eff}$ is thus not perpendicular to $B_0$. The off-resonance magnetization will then precess simultaneously about $B_0$ and $B_{eff}$. For a given RF pulse, the rotation of the magnetization vector of off-resonance spins will thus be lower than for on-resonance spins.

In general, the state of the nuclear magnetization vector is not described relative to the fixed laboratory frame, but with respect to a rotating frame of reference, which rotates at frequency $\omega_0$, the spectrometer reference frequency. Relative to the rotating frame of reference, the magnetization of on-resonance spins precesses, during excitation, about the $B_1$-field only. The angle of rotation that the magnetization vector travels about $B_1$ during application of the pulse is generally referred to as the "flip angle" of the pulse.

### 2.2.1 Selective excitation

Off-resonant behavior is important because of its role in selective excitation. Selective excitation involves the application of an RF pulse that affects only a part of the NMR frequency spectrum. Spatial labeling of spins is achieved when selective excitation is combined with a magnetic field gradient. A magnetic field gradient causes a spatially varying magnetic field and therefore a spatial dependence of the Larmor frequency. Selective excitation is the basis of most magnetic resonance imaging techniques. Since the strength of the field gradients is much smaller than that of the polarizing field $B_0$, the Larmor frequency depends approximately linearly on the strength of the applied field gradient:

$$\omega_0(\vec{r}) = \gamma B_0 + \gamma G(\vec{r})\vec{r} \tag{2.5}$$

where $\vec{r}$ are the coordinates of the nuclear spin in the gradient direction. This equation lies at the heart of the MR imaging principle, first proposed in 1973 [3, 4].

For flip angles of less than or equal to 90°, the frequency spectrum of a pulse is given by its Fourier transform. For a pulse with a rectangular time domain profile (constant power for a given duration), the corresponding frequency spectrum is a sinc-function ($sin(x)/x$). However, the selection of spins in a slice with rectangular spatial profile is generally preferred for imaging applications. This is typically achieved using a pulse with sinc-shaped time domain profile, in combination with a linear magnetic field gradient. A sinc-pulse based on a sinus with period $\tau$ will excite spins in a frequency band with a width of $2/\tau$ [2]. For a given duration of the sinc-pulse, the thickness of the slice is determined by the amplitude of the gradient, since the frequency change in the gradient direction is proportional to the gradient amplitude (see Eq. 2.5).

### 2.2.2 Acquisition of an image

After selective excitation has been employed to excite spins in a slice of the object, the selected spins should be separated according to their location in the slice plane. This is typically done using magnetic field gradients. The phase of the transverse magnetization will be dispersed in the presence of a field gradient, depending on the location of the spins along the gradient. The level of dispersion depends on the product of gradient strength and duration, and on the size of the sample.

A schematic representation of a simple gradient-echo experiment is shown in Fig. 2.1. When data are acquired in the presence a constant-amplitude gradient, the phase dispersion in the gradient direction can be registered as a function of time (see the G$_{read}$- and signal-axes). A similar encoding strategy can be applied in the perpendicular slice-plane direction. This is generally done by loop-wise repetition of selective excitation and data acquisition in the presence of a gradient, perpendicular to both the slice selection and read-out gradients. This additional gradient is applied between excitation and data acquisition (G$_{phase}$ in Fig. 2.1), and has a different strength in each repetition. The acquired signal thus depends on the phase-encode and read-out gradients, and on the spin-density distribution within the slice:

$$S(t) = \int_{-\infty}^{\infty} M(x,y) \cdot e^{i\gamma(G_x x + G_y y)t} dxdy \tag{2.6}$$

where $G_x$ and $G_y$ are the gradients applied in perpendicular directions in the image plane (for example G$_{read}$ and G$_{phase}$ in Fig. 2.1). The spatial spin-density distribution ($M(x,y)$) is determined through Fourier-transformation of the NMR signal. The map of MR signal is referred to as frequency domain or, because of the relationship between resonance frequency and spatial location, k-space ($k_i = (2\pi)^{-1}\gamma G_i t$, where $i \in \{x,y,z\}$). An example of a k-space map and the corresponding MR image is shown in Fig. 2.2.

Note that acquisition of the MR signal is typically done with phase sensitive detection oscillating at resonance frequency: the detected signal is mixed with a reference oscillation. This process is known as heterodyne mixing, and the result is a signal at the difference frequency. If $\gamma B_0$ was chosen as the frequency of the resonance oscillation and a homogeneous magnetic field is assumed, the detected signal will oscillate at $\gamma G(\vec{r})\vec{r}$ (see Eq. 2.5).

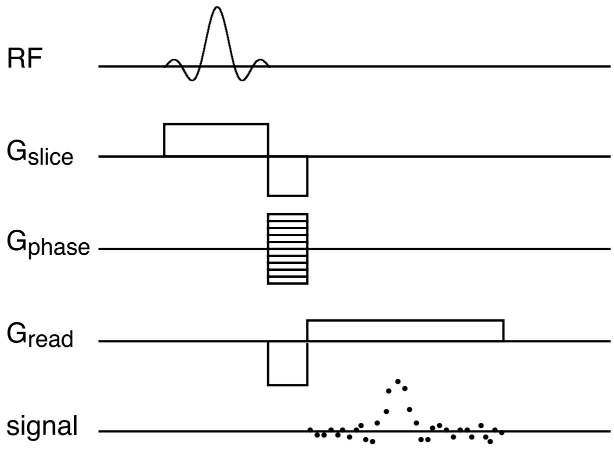

Figure 2.1: *Simple gradient echo MR imaging sequence. A sinc-shaped RF pulse in the presence of a linear magnetic field gradient selectively excites a slice with rectangular profile in the object. Data are acquired in presence of a magnetic field gradient perpendicular to the slice selection gradient. The experiment is repeated in the presence of a gradient of varying strength, applied between slice selection and data acquisition, perpendicular to both slice select and read-out gradient. The gradients dephase magnetization as a function of the spatial location of the spins within the object, thus permitting the reconstruction of a map of the spatial spin-density distribution.*

The phase of the MR signal does not only evolve because of the applied gradient pulses, but in addition due to magnetic field inhomogeneities. Loss of phase coherence due to field inhomogeneities can be refocused by the application of an RF pulse between slice excitation and data acquisition. Such an experiment is called a spin-echo experiment and will not be further discussed here.

### 2.2.3 Relaxation

A resonant RF pulse causes distortion of the spin system from its thermal equilibrium state. This equilibrium will be restored by a process known as spin-lattice relaxation. Spin-lattice relaxation involves an exchange of energy between the spin system and the surrounding thermal reservoir, with which it is in equilibrium. The equilibrium is characterized by a state of polarization with magnetization $M_0$ along the polarizing field $B_0$. The restoration of the equilibrium is exponential, characterized a time constant known as $T_1$.

In addition to the effect of $T_1$-relaxation, the NMR signal will decrease due to a second relaxation process, spin-spin relaxation. Spin-spin relaxation is the process where nuclear spins exchange energy amongst themselves. Due to this process, there is no net change in the population of the energy levels which correspond to the different spin states, it leads however to a loss of phase coherence. The time constant of this relaxation process is called $T_2$. It is obvious that $T_2 \leq T_1$. As was mentioned previously, magnetic field inhomogeneities will contribute to loss of phase coherence. If these are not refocused, this will lead to a signal decay with a time

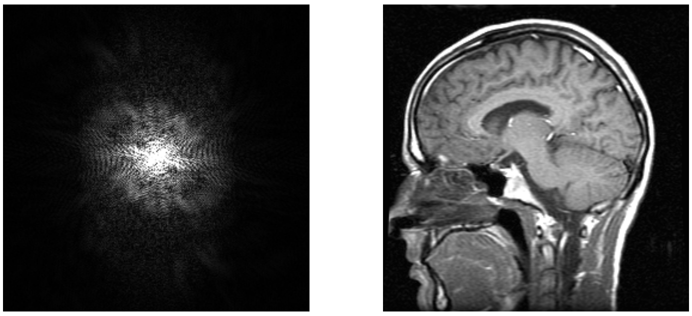

a b

Figure 2.2: *(a) Signal intensity map (k-space) and (b) corresponding MR intensity image. Note that the intensity in the center of the k-space map has been clipped to improve figure clarity.*

constant that is shorter than the $T_2$ of the spin system, which is generally referred to as $T_2^*$.

The evolution of the nuclear magnetization along the three axes of the rotating frame (at reference frequency $\omega_0$) as a function of time can be expressed as a set of relationships known as the Bloch equations [5]:

$$\begin{aligned}
\frac{dM_x}{dt} &= \gamma M_y \left(B_0 - \frac{\omega}{\gamma}\right) - \frac{M_x}{T_2} \\
\frac{dM_y}{dt} &= \gamma M_z B_1 - \gamma M_x \left(B_0 - \frac{\omega}{\gamma}\right) - \frac{M_y}{T_2} \\
\frac{dM_z}{dt} &= -\gamma M_y B_1 - \frac{M_z - M_0}{T_1}
\end{aligned} \tag{2.7}$$

where the direction of the polarizing field is, by convention, along the z-axis, and the resonant RF-field along the x-axis. $\omega$ is the resonance frequency of the spins. Contributions to relaxation other than those from $T_1$- and $T_2$-processes are omitted.

### 2.2.4 Signal intensity

In general, the repetition time of the MR experiment is less than or on the order of $T_1$, the equilibrium magnetization will not fully recover in the time between a series of successive RF pulses, an effect which is known as partial saturation [6]. For low flip angle, the equilibrium magnetization in a fast RF-spoiled gradient-echo experiment, immediately before each RF pulse, is then a function of $T_1$, the repetition time (TR, time between excitations), and flip angle $\alpha$, according to the following relationship:

$$S = cM_0 sin(\alpha) \frac{1 - exp[-TR/T_1]}{1 - cos(\alpha) exp[-TR/T_1]} \tag{2.8}$$

where $S$ is the signal intensity immediately after excitation, $c$ is a constant which depends on the MR hardware, and $M_0$ is the equilibrium magnetization. Normally, signal is acquired a certain period (TE) after excitation, so that it is subject to $T_2^*$-relaxation. The signal $S$ acquired in a conventional gradient echo sequence is then [7]:

$$S = cM_0 sin(\alpha) \frac{1 - exp[-TR/T_1]}{1 - cos(\alpha) exp[-TR/T_1]} e^{-TE/T_2^*} \tag{2.9}$$

From this equation, the value for for $\alpha$, leading to maximum signal for a given TR, can be found:

$$cos(\alpha) = e^{-\frac{TR}{T_1}} \tag{2.10}$$

This angle is known as the Ernst-angle.

When the repetition time of the experiment is short (lower than $T_1$ and $T_2$), the magnetization is permanently in a "steady state" of excitation (see Eq. 2.8), the NMR signal is then no longer a function of the direct free induction decay (FID) signals only, but is composed of, amongst others, a mixture of direct FID signals and stimulated echoes [8]. Stimulated echoes are generated by three RF pulses, which are not necessarily subsequent. Longitudinal magnetization can be generated from the direct FID-signal by one of the pulses that follow. From this longitudinal magnetization, transverse magnetization can be generated by one of the succeeding RF pulses. A significant contribution from stimulated echoes is formed by a train or RF pulses when TR $\ll T_2$. The ratio of the first stimulated echo component ($S_{ste}$, formed by three subsequent RF pulses) with respect to the direct FID-signal ($S_{fid}$) is:

$$\frac{S_{ste}}{S_{fid}} = 0.5 e^{-2 \cdot TR/T_2} e^{-TR/T_1} sin^2(\alpha) \tag{2.11}$$

but various pathways can lead to stimulated echoes in a fast gradient-echo sequence. If the phase of the simulated echoes remains constant, their signals are summed. The relative contribution of stimulated echoes can be reduced by avoiding such a coherent contribution of stimulated echoes. The relative contribution from stimulated echoes to the signal can be manipulated, either by varying the pulse repetition time [9], the use of spoiler gradients [10], or by varying the phase of the RF pulse over subsequent excitations [11, 12]. In most practical applications today, RF phase-modulation has become the technique of choice due to its effectiveness at a large range of experimental parameters and flexibility of implementation [12]. The RF phase-cycling leads to spreading the phase of the various stimulated echo signals over the transverse plane.

## 2.3 MR thermometry

A number of parameters which play a role in an MRI experiment are temperature dependent. MR temperature imaging methods, based on the temperature dependence of molecular diffusion constant D [13], the spin-lattice relaxation time $T_1$ [14, 15], and the resonance frequency of water protons [16, 17], have been thoroughly investigated.

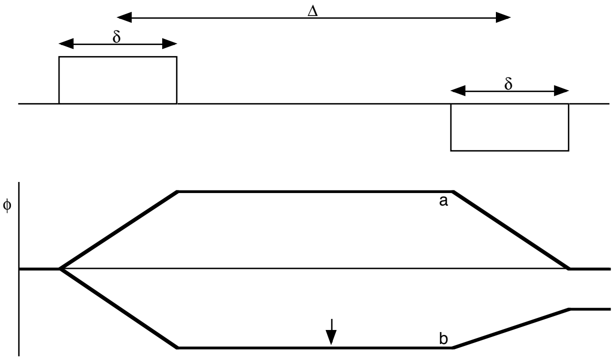

Figure 2.3: *Phase evolution of the net magnetization of two groups of spins, subject to two counteracting linear gradients. Initially, both groups of spins are present at equal distance from, but on opposite sides of, the gradient zero-crossing. Group* a *remains immobile throughout the given time frame, group* b *is subject to a single displacement in the direction of gradient zero-crossing during the delay between the two gradients (e.g. at a time indicated by the arrow). Its position closer to gradient zero-crossing submits it to a smaller field change upon application of the second gradient.*

### 2.3.1 Temperature dependence of the diffusion constant

The thermal brownian motion of an ensemble of molecules is described by the diffusion constant D. The relation between temperature and the diffusion constant is exponential [13]:

$$D \propto e^{-\frac{E_a}{kT}} \tag{2.12}$$

where $E_a$ is the activation energy of the molecular motion, $k$ the Boltzmann constant and $T$ is temperature.

Diffusion constants can be measured with MR, since diffusion induces an amplitude attenuation of the MR signal upon application of mutually counteracting magnetic field gradients. This attenuation is caused by a loss of phase coherence among precessing spins because of random movement along the direction of the gradients [18]. The attenuation depends only on the diffusion coefficient and applied gradients. An example of this effect is shown in Fig. 2.3, where the phase of the net magnetization of two groups of spins is shown, one group being immobile, the other being subject to a given movement in the time between two gradients. Since diffusional displacement is random, a phase dispersion will thus result, leading to signal attenuation. The effect of the applied gradients is accounted for in a factor $b$, which describes the exponential attenuation $e^{-bD}$ of the transverse magnetization. The $b$-factor can be calculated from the gradient characteristics strength ($G$), duration (δ) and separation (Δ) [19] (see also Fig. 2.3):

$$b = -\gamma^2 G^2 \delta^2 (\Delta - \frac{\delta}{3}) \tag{2.13}$$

where $\Delta$ is the time between the center of two gradients of strength $G$, applied during a period $\delta$. The diffusion coefficient can be calculated from the signal in two MR images with different diffusion sensitization (different $b$-value, generally achieved by the application of strong additional gradients):

$$D = \frac{ln(A_1/A_0)}{b_0 - b_1} \tag{2.14}$$

where $A_0$ and $A_1$ are the signal amplitudes in the two images, acquired with respectively factors $b_0$ and $b_1$. From Eq. 2.12 can be derived that a map of temperature changes can thus be obtained as follows:

$$\Delta T = T_1 - T_0 = \frac{kT_0^2}{E_a} \cdot \frac{(D_1 - D_0)}{D_0} \tag{2.15}$$

where $D_0$ and $D_1$ are the diffusion constants determined at temperatures $T_0$ and $T_1$, respectively. It is assumed that temperature variations are small ($\Delta T \ll T_0$) and that $E_a$ remains constant. The temperature dependent change in D for water is on the order of 2%/°C [13], since $E_a$ is 0.2 eV at 20°C [20].

### 2.3.2 Temperature dependence of $T_1$ relaxation time

Both $T_1$ and its temperature dependence differ between tissues, but a linear dependence of $T_1$ on 1/T is predicted over a small temperature range, since the variation of $T_1$ with temperature is [21]:

$$T_1(T) = T_1(\infty) \cdot e^{-\frac{E_a}{kT}} \tag{2.16}$$

where $E_a$ is the activation energy of the relaxation process. Changes in $T_1$ are of the order of 1-1.5% per °C at body temperature [22]. Cline et al. have shown that the signal change in an MR image as a function of temperature can be derived from Eq. 2.9 [23], assuming that:

$$T_1 = T_{1,0} + m(T - T_0) \tag{2.17}$$

where $m$ is the tissue dependent temperature dependence of $T_1$ (%/°C), and $T_{1,0}$ is the $T_1$ of the tissue at reference temperature $T_0$. It can then be derived that [23]:

$$\frac{dS}{dT} = -S_0 \left[ \frac{m \cdot TR\big(1 - cos(\alpha)\big)E}{(T_{1,0})^2\big(1-E\big)\big(1 - cos(\alpha)E\big)} + \frac{1}{T_0} \right] \tag{2.18}$$
$$where: \;\; E = exp\left[ -\frac{TR}{T_{1,0} + m(T - T_0)} \right]$$

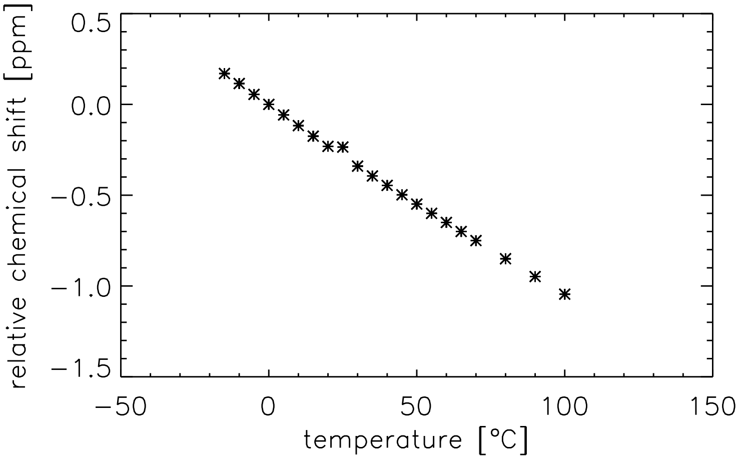

Figure 2.4: *Water proton resonance frequency as function of temperature relative to the water proton resonance frequency at 0°C, as experimentally obtained by Hindman [24]. The results demonstrate a mostly linear dependence of chemical shift on temperature over a large temperature range.*

where $S_0$ is the signal at reference temperature. Using this equation, temperature changes can be calculated from image signal changes, assuming that the $T_1$ of the tissue at reference temperature is known.

### 2.3.3 Temperature dependence of water proton resonance frequency

Initial experiments on the temperature dependence of the resonance frequency of protons in water were performed to obtain knowledge about the intermolecular forces leading to cohesion and hydrogen-bond formation between water molecules. An extensive study was performed by Hindman [24], who investigated this dependence in water in both gas and liquid states for temperatures ranging from -15 to 100°C. The results of these experiments are represented in Fig. 2.4. A detailed model for the interactions underlying the temperature dependence of the water proton resonance frequency was described in earlier work [25], suggesting that the proton resonance frequency shift was solely dependent on the average number of hydrogen bonds within the sample.

Hindman described the contribution of different factors to the magnetic shielding constant, which causes the chemical shift. Determination of the magnitude of the various contributions is difficult. Hindman therefore assumed in his model that water in liquid state is a temperature-dependent equilibrium between two phases, a hydrogen-bonded "ice-like" fraction and a non-hydrogen-bonded monomeric fraction. In this model, the ice-like phase appears in small clusters in bulk water. The two fractions have different magnetic shielding constants. An increase in temperature reduces the ice-like fraction, thus increasing the magnetic shielding, which in turn results in a change in resonance frequency.

Ishihara et al. suggested that the temperature dependent frequency shift can be determined from the phase in gradient-echo images, which is based on just such chemical shift properties [16, 26]. The local magnetic field inhomogeneity $\Delta B_0$ can be described as the sum of a temperature independent contribution, $\delta B_0$, and the chemical shift field $B_c$:

$$\Delta B_0(T(\vec{r})) = \delta B_0(\vec{r}) + B_c(T(\vec{r})) \tag{2.19}$$

where $\vec{r}$ represents a spatial vector, and $\delta B_0$ depends on magnet inhomogeneity and magnetic susceptibility of the sample. In order to measure changes in chemical shift, the term $\delta B_0$ must be canceled out, which can be accomplished by subtraction of the field distribution at reference temperature $T_0$ from the field distribution at temperature $T$. Hereby is assumed that the magnetic susceptibility is independent of temperature. A number of studies have indicated that the temperature dependence of susceptibility can however be non-negligible [27, 28, 29].

Field inhomogeneities can be calculated from the phase information in gradient echo images:

$$\Delta\Phi(T(\vec{r})) = \gamma \cdot \Delta B_0(T(\vec{r})) \cdot TE \tag{2.20}$$

where $\Phi(\vec{r})$ is the phase image and $\gamma$ the gyromagnetic ratio. Changes in temperature can then be calculated as follows:

$$\Delta T(\vec{r}) = \frac{\Delta B_0}{\alpha \cdot B_0} \tag{2.21}$$

where $\alpha$ is the temperature dependent water chemical shift in ppm/°C. From Eq. 2.20 and 2.21 can then be derived that:

$$\Delta T(\vec{r}) = \frac{\Delta\Phi(T(\vec{r}))}{\alpha \cdot \gamma \cdot TE \cdot B_0} \tag{2.22}$$

which is the equation on which PRF-based temperature imaging is based.

## 2.4 Comparison of MR thermometry methods

MR thermometry experiments in this thesis are all based on the shift of the water proton resonance frequency. One major advantage of the proton resonance frequency method with respect to diffusion- or $T_1$-based imaging is that its temperature dependence is, at first approximation, independent of tissue composition. Both diffusion- and $T_1$-based thermometry depend on tissue composition and might be influenced significantly by thermal coagulation [30, 31]. It should be mentioned that discrepancies exist in the values reported for the PRF temperature dependence in vivo. Values ranging from -0.0067 ppm/°C, reported during RF-heating of canine muscle [32], to -0.0146 ppm/°C, measured during heating of rat thigh muscle using an external water bag [33], have been reported. Recent detailed ex vivo studies by Peters et al. nevertheless demonstrate that the PRF-temperature dependence for eight different tissue samples was -0.0101±0.0004 ppm/°C [34], and may thus be considered, at first approximation, independent of tissue composition (except for errors due to fat content, see chapter 5).

In addition, the proton chemical shift is determined by resonance frequency only and can be detected independent of the other parameters. $T_1$- and diffusion-based MR thermometry experiments exploit changes in signal amplitude to determine a change in either $T_1$ or D. Because of the relatively strong gradients used to obtain diffusion-sensitization, the signal-to-noise ratio of the images will be sub-optimal.

## References

[1] P.T. Callaghan, Principles of nuclear magnetic resonance microscopy, Oxford science publications, ISBN 0-19-853997-5, 1991

[2] W. Oldendorf, W. Oldendorf Jr., Basics of magnetic resonance imaging, Martinus Nijhof publishing, ISBN 0-89838-964-X, 1988

[3] P.C. Lauterbur, Image formation by induced local interactions: examples employing nuclear magnetic resonance. *Nature* **242**, 190-191 (1973)

[4] P. Mansfield, P.K. Grannell, NMR diffraction in solids? *J. Phys. C.* **6**, L422 (1973)

[5] A. Abragam, Principles of nuclear magnetism, Clarendon Press, Oxford (1961)

[6] R. Freeman, H. Hill, *J. Chem. Phys.* **54**, 3367 (1971)

[7] F.W. Wehrli, Fast-scan magnetic resonance: principles and applications. *Magn. Reson. Q.* **6**, 165-236 (1990)

[8] M.L. Gyngell, The steady-state signals in short-repetition-time sequences. *J. Magn. Reson.* **81**, 474-483 (1989)

[9] R. Freeman, H.D.W. Hill, Phase and intensity anomalies in fourier transform NMR. *J. Magn. Reson.*, 366-383 (1971)

[10] A.P. Crawley, M.L. Wood, R.M. Henkelman, Elimination of transverse coherences in FLASH MRI. *Magn. Reson. Med.* **8**, 248-260 (1988)

[11] Y. Zur, M.L. Wood, L.J. Neuringer, Spoiling of of transverse magnetization in steady-state sequences. *Magn. Reson. Med.* **21**, 251-263 (1991)

[12] J.H. Duyn, Steady state effects in fast gradient echo magnetic resonance imaging. *Magn. Reson. Med.* **37**, 559-568 (1997)

[13] D. Le Bihan, J. Delannoy, R.L. Levin, Temperature mapping with MR imaging of molecular diffusion: application to hyperthermia *Radiology* **171**, 853-857 (1989)

[14] D.L. Parker, V. Smith, P. Sheldon, L.E. Crooks, L. Fussell, Temperature distribution measurements in two-dimensional NMR imaging. *Med. Phys.* **10**, 321-325 (1983)

[15] R.J. Dickinson, A.S. Hall, A.J. Hind, I.R. Young, Measurement of changes in tissue temperature using MR imaging. *J. Comput. Assist. Tomogr.* **10**, 486-472 (1986)

[16] Y. Ishihara, A. Calderon, H. Watanabe, K. Mori, K. Okamoto, Y. Suzuki, K. Sato, K. Kuroda, N. Nakagawa, S. Tsutsumi, A precise and fast temperature mapping method using water proton chemical shift, in "Proc., SMRM, 11th annual meeting, Berlin, 1992", p. 4803

[17] J. De Poorter, C. De Wagter, Y. De Deene, C. Thomsen, F. Ståhlberg, E. Achten, Noninvasive MRI thermometry with the proton resonance frequency (PRF) method: In vivo results in human muscle. *Magn. Reson. Med.* **33**, 74-81 (1995)

[18] H.Y. Carr, E.M. Purcell, Effects of diffusion on free precession in nuclear magnetic resonance experiments. *Phys. Rev.* **94**, 630-638 (1954)

[19] E.O. Stejskal, J.E. Tanner, Spin diffusion measurements: spin-echoes in the presence of a time-dependent field gradient. *J. Chem. Phys.* **42**, 288-292 (1965)

[20] J.H. Simpson, H.Y. Carr, Diffusion and nuclear spin relaxation in water. *Phys. Rev.* **111**, 1201-1202 (1958)

[21] A.S. Hall, M.V. Prior, J.W. Hand, I.R. Young, R.J. Dickinson, Observation by MR imaging of in vivo temperature changes induced by radio frequency hyperthermia. *J. Comput. Assist. Tomogr.* **14**, 430-436 (1990)

[22] P.A. Bottomley, T.H. Foster, R.E. Argersiger, L.M. Pfeifer, A review of normal tissue hydrogen NMR relaxation times and relaxation mechanisms from 1-100 MHz: dependence on tissue type, NMR frequency, temperature, species, excision, and age. *Med. Phys.* **11**, 425-447 (1984)

[23] H.E. Cline, K. Hynynen, C.J. Hardy, R.D. Watkins, J.F. Schenck, F.A. Jolesz, MR temperature mapping of focused ultrasound surgery. *Magn. Reson. Med.* **31**, 628-636 (1994)

[24] J.C. Hindman, Proton resonance shift of water in the gas and liquid states. *J. Chem. Phys.* **44**, 4582-4592 (1966)

[25] W.G. Schneider, H.J. Bernstein, J.A. Pople, *J. Chem. Phys.* **28**, 601 (1958)

[26] Y. Ishihara, A. Calderon, H. Watanabe, K. Okamoto, Y. Suzuki, K. Kuroda, Y. Suzuki, A precise and fast temperature mapping using water proton chemical shift. *Magn. Reson. Med.* **34**, 814-823 (1995)

[27] J. De Poorter, Noninvasive MRI thermometry with the proton resonance frequency method: study of susceptibility effects. *Magn. Reson. Med.* **34**, 359-367 (1995)

[28] I.R. Young, J.V. Hajnal, I.G. Roberts, J.X. Ling, R.J. Hill-Cottingham, A. Oatridge, J.A. Wilson, An evaluation of the effects of susceptibility changes on the water chemical shift method of temperature measurement in human peripheral muscle. *Magn. Reson. Med.* **36**, 366-374 (1996)

[29] R.D. Peters, R.S. Hinks, R.M. Henkelman, Heat-source orientation and geometry dependence in proton-resonance frequency shift magnetic resonance thermometry. *Magn. Reson. Med.* **41**, 909-918 (1999)

[30] S.J. Graham, M.J. Bronskill, R.M. Henkelman, Time and temperature dependence of MR parameters during thermal coagulation of ex vivo rabbit muscle. *Magn. Reson. Med.* **39**, 198-203 (1998)

[31] S.J. Graham, G.J. Stanisz, A. Kecojevic, M.J. Bronskill, R.M. Henkelman, Analysis of changes in MR properties of tissues after heat treatment. *Magn. Reson. Med.* **42**, 1061-1071 (1999)

[32] J.R. MacFall, D.M. Prescott, H.C. Charles, T.V. Samulski, $^1$H MRI phase thermometry in vivo in canine brain, muscle, and tumor tissue. *Med. Phys.* **23**, 1775-1782 (1996)

[33] K. Kuroda, Y. Suzuki, Y Ishihara, K. Okamoto, Y. Suzuki, Temperature mapping using water proton chemical shift obtained with 3D-MRSI: feasibility in vivo. *Magn. Res. Med.* **35**, 20-29 (1996)

[34] R.D. Peters, R.S. Hinks, R.M. Henkelman, Ex-vivo tissue type independence in proton-resonance frequency shift MR thermometry. *Magn. Reson. Med.* **40**, 454-459 (1998)

# Chapter 3

# Focused Ultrasound

## Contents

**3.1 Ultrasound properties** **42**

**3.2 Focused ultrasound** **43**

**3.3 FUS guidance** **44**

The effects of ultrasound on various tissues have first been thoroughly studied by Wood and Loomis [1], using non-focused, plane waves. The first application of focused ultrasound (FUS) [2] to living tissue dates from 1942 [3].

## 3.1 Ultrasound properties

Ultrasound is an acoustic sound wave with a frequency of more than 18 kHz. It is propagated as a mechanical wave, leading to periodic motion of particles within the medium. The characteristics of the wave are determined by the disturbance from which it originates, in this case the ultrasound transducer, and by the acoustic properties of the medium through which the wave travels. During focused ultrasound hyperthermia treatment, the wave is longitudinal, transverse (shear) waves are only formed under circumstances such as a soft tissue-bone interface [4]. The propagation speed ($v$) of ultrasound depends on both density ($\rho$) and acoustic impedance ($Z$) of the medium:

$$v = \frac{Z}{\rho} \tag{3.1}$$

When the ultrasound wave meets the interface between two media, it may be partially reflected and partially transmitted (see Fig. 3.1), depending on the incident angle and the difference in acoustic impedance between the two media. The angle of reflection ($\theta_r$) is always identical to the incident angle ($\theta_i$), whereas the transmission angle ($\theta_t$) depends on the impedance of the two media, according to Snell's law:

$$\frac{sin\theta_i}{sin\theta_t} = \frac{v_1}{v_2} \tag{3.2}$$

The ratio between the reflected ($p_r$) and incident acoustic power ($p_i$) depends on the acoustic impedance of the media and the incident angle:

$$\frac{p_r}{p_i} = \frac{Z_2 cos\theta_i - Z_1 cos\theta_t}{Z_2 cos\theta_i + Z_1 cos\theta_t} \tag{3.3}$$

which is valid only if the ultrasound wavelength is smaller than the dimensions of the reflecting object. When the wavelength is comparable to or greater than the object, the wave is scattered in all directions. Since the acoustic impedance of air and tissue differ by more than a factor of $10^3$, practically all of the ultrasound is reflected at tissue/air-interfaces [4].

In a given medium, the ultrasound energy will be attenuated exponentially. For a plane wave, assuming that there is no wave distortion, the intensity $I(x)$ at depth $x$ into the medium is described by:

$$I(x) = I(0)e^{-2\mu x} \tag{3.4}$$

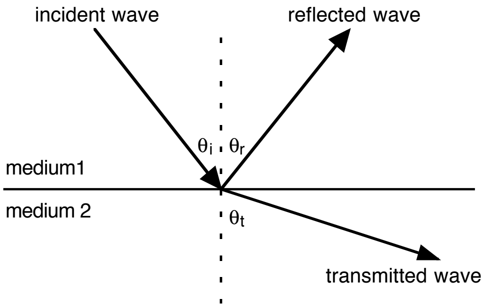

Figure 3.1: *Reflection and transmission of ultrasound at the flat interface of two media with different ultrasonic properties.*

where $I(0)$ is the intensity at the surface of the medium and $\mu$ is the amplitude attenuation coefficient per unit path length. Attenuation is the sum of losses due to absorption and scattering of the wave. In a purely elastic medium, the ultrasound absorption should depend on the square of the frequency, but in tissue the absorption has been shown to increase approximately linearly with frequency [5]:

$$\alpha = \alpha_0 f^m \tag{3.5}$$

where $f$ is the ultrasound frequency in MHz and $\alpha_0$ the absorption coefficient at 1 MHz. $\alpha_0$ and $m$ both depend on tissue type, $m$ has been experimentally found to be between 1 and 1.2 for soft tissue [5]. The attenuation coefficient $\mu$ has been found to depend on frequency in a similar manner to the frequency dependence of absorption, however, attenuation of ultrasound is higher than would be expected on the basis of viscosity of the medium only [4]. During the compression part of the cycle, energy is stored in lattice and molecular vibrational energy, and as translational energy. Not all of this kinetic energy is returned to the wave during the expansion part of the cycle, causing an increase in tissue temperature. Note that the absorption of ultrasound in bone is high (10-20 fold higher than in tissue [4]).

## 3.2 Focused ultrasound

Focused ultrasound can be generated using a curved, resonant piezo-electric element or a flat piezo-electric element in combination with a suitable lens. The principle is based on interference of the ultrasound waves, similar to the effect of a lens in optics. At the focal point, waves originating from different points on the ultrasound transducer are in phase. The shape of the focal point depends on the curvature of the piezo-electric element [6]:

$$d = 1.41\frac{\lambda}{\phi} \tag{3.6}$$

$$l = 9.9\frac{\lambda}{\phi^2} \tag{3.7}$$

where $d$ is the width (half peak pressure level) of the focal point and $l$ its length along the axis of the transducer. $\lambda$ is the ultrasound wavelength and $\phi$ the focusing strength, the ratio of transducer diameter to focal length. Hereby it is assumed that no defocusing occurs due to refractive inhomogeneities.

Eq. 3.6 and 3.7 indicate that the focus will be tighter for higher frequencies. However, the attenuation of the ultrasound by tissue in the path of the beam will increase with frequency, as can be seen from Eq. 3.5. Generally, the ultrasound frequencies used for FUS heating of tissues are in the lower megahertz range.

An alternative method to focus ultrasound is the combination of multiple small ultrasound elements, a so-called phased array [7]. The amplitude and phase of the driving signal for each of the individual elements are controlled such that emitted waves are in phase at the desired focal point. In order to be able to do so, the elements should behave like point sources, their size should be inferior to the wavelength to avoid formation of lobes [8]. For curved arrays, the element size can be up to twice the wavelength [4].

## 3.3 FUS guidance

The need for FUS guidance exists since refractive inhomogeneities will exist in biological tissues. Depending on the path of the FUS beam through the tissue, the focal point will change in shape and position. Also, when high ultrasound powers are used, the focal point will move towards the transducer and its shape deviates from the ellipsoidal. One of the factors involved is the increased absorption ahead of the focal plane due to slight increase in tissue temperature [6].

## References

[1] R.W. Wood, A. Loomis, The physical and biological effects of high frequency sound-waves of great intensity. *Phil. Mag.* **4**, 417 (1927)

[2] L. Grutzmacher, Piezoelectrischer Kristall mit Ultraschallkonvergenz. *Z. Phys.* **96**, 342 (1935)

[3] J.G. Lynn, R.L. Zwemer, A.J. Chick, A.E. Miller, A new method for the generation and use of focused ultrasound in experimental biology. *J. Gen. Physiol.* **26**, 179-193 (1942)

[4] K. Hynynen, Ultrasound heating technology. In: M.H. Seegenschmiedt, P. Fessenden, C.C. Vernon (eds), Thermoradiotherapy and thermochemotherapy, volume 1: biology, physiology, physics. Springer, Berlin, ISBN 3-540-57229-5, 253-278 (1995)

[5] S.A. Goss, L.A. Frizzell, F. Dunn, Ultrasonic absorption and attenuation of high frequency sound in mammalian tissues. *Ultrasound Med. Biol.* **5**, 181-186 (1979)

[6] G. ter Haar, Ultrasonically induced minimally invasive surgery. *J.E.M.U.* **19**, 255-259 (1998)

[7] L.A. Frizzell, P.J. Benkeser, K.B. Ocheltree, C.A. Cain, Ultrasound phased arrays for hyperthermia treatment. “Proc. IEEE Ultrasonics symp., 1985”, 930-935

[8] B.D. Steinberg, Principles of aperture and array design. John Wiley, New York (1976)

# Part II

# Methodology: Developments in MR Temperature Imaging

# Chapter 4

# Fast Temperature Imaging

Jacco A. de Zwart, Peter van Gelderen, Dan J. Kelly, Chrit T.W. Moonen
”Fast Magnetic-Resonance Temperature Imaging”
*Journal of Magnetic Resonance B* **112**, 86-90 (1996)

It has long been realized that local temperature elevation using focused ultrasound (FUS) can have medical benefits, for example, in cancer therapy [1, 2]. However, problems with the evaluation of power dosage and with focusing the ultrasound power at the target location have prevented widespread use. Magnetic-resonance imaging can be used, not only to provide detailed anatomical images, but also to provide temperature images [3]. Therefore, the combination of FUS and MRI appears to be promising for medical interventions [4, 5]. Ideally, pulsed, low-dose ultrasound would be used to elevate temperature by at most a few degrees Celsius. MR temperature imaging would then be used for dosimetry and for focusing the ultrasound interactively at the target location. Then, the therapeutic dose of ultrasound would be delivered. The interactive FUS adjustment necessitates a high temporal resolution in temperature imaging because of two reasons: (1) to avoid problems due to patient motion; and (2) to minimize the effects of thermal conduction (due to diffusion and perfusion processes) on temperature quantitation. The FUS pulse and the acquisition of a 3D temperature map should thus be completed in a few seconds. The speed and accuracy of currently used temperature imaging prevents an extensive interactive adjustment without some immobilization of tissue. Here, we will demonstrate that MR temperature imaging can be accelerated drastically while maintaining a high accuracy.

MR thermometry may be based on changes in the spin-lattice relaxation time $T_1$ [3, 5, 6], the diffusion constant D [7], or the proton resonance frequency (PRF) [8-12]. The temperature dependence of $T_1$ and diffusion coefficient is affected by tissue composition (protein content, membranes, solutes, [9, 10]), whereas the PRF is largely independent of these factors [9, 10]. Therefore, PRF-based methods appear advantageous for MR temperature imaging. The temperature dependence of the PRF is based on changes in the average strength of hydrogen bonds [13]. Ishihara first suggested the use of phase changes in gradient-echo images to calculate the temperature-dependent change in PRF [8]. Recent studies have confirmed the advantages of the PRF method [11, 12].

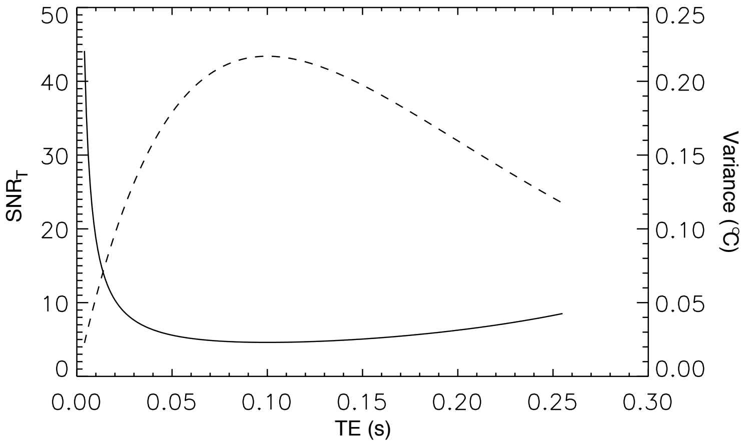

Figure 4.1: *Theoretical signal-to-noise ratio of PRF-based MRI thermometry ($SNR_T$) as a function of TE (dashed curve, left axis), together with variance of the temperature as a function of TE (solid line, right axis) for a sample with $T_2^*$ of 100 ms and initial image SNR of 100. Simulation was performed for a temperature increase of 1°C.*

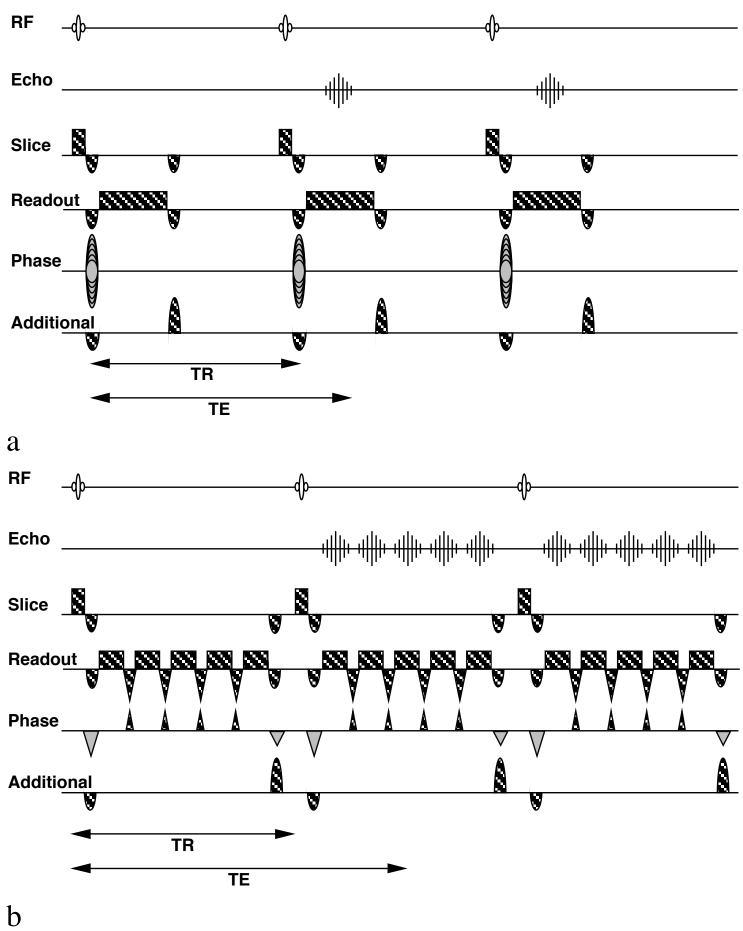

Figure 4.2: *(a) ES-FLASH sequence with additional gradients resulting in echo shifting (TE > TR); (b) PRESTO sequence, combining acquisition of multiple gradient echoes per TR with echo shifting. Note that the additional gradients remain identical in each TR period. For more details see Refs. [14-16].*

Here, we present methods for accelerated MR temperature imaging based on PRF. We start with an analysis of the accuracy of the temperature experiment. A gradient-echo image is acquired at the starting temperature, and a second gradient-echo image is acquired following temperature elevation. In order to minimize the total imaging time, the repetition time TR (time between successive excitations) must be kept very short. Previously, gradient-echo imaging has been performed with the limitation of TE $<$ TR. Thus, the short TR values necessary for fast-gradient-echo MRI led to suboptimal TE values. However, the recently published [14] echo-shifting principle (gradient echoes with TE $>$ TR) should allow an optimization of TE, given a very short TR, for fast MR temperature imaging without a loss in total imaging time. The accuracy of PRF-based MR thermometry is determined by the signal-to-noise ratio (SNR) in the two images, and the phase difference accumulated during the echo time (TE). The difference in phase angle increases linearly in time, whereas the image SNR decreases exponentially as a function of time. Therefore, in case of a fixed (short) TR, the SNR in the temperature image (called $\mathrm{SNR}_T$) can be expressed as

$$SNR_T = c \cdot TE \cdot e^{-\frac{TE}{T_2^*}} \tag{4.1}$$

where $c$ is a constant depending on spin density, flip angle, TR, as well as instrument parameters (field strength, RF coil); and $\mathrm{T}_2^*$ is the decay constant of the transverse magnetization due to local inhomogeneities and spin-spin relaxation effects. Figure 4.1 gives a simulation of $\mathrm{SNR}_T$ as a function of TE, as well as the variance in the temperature as a function of TE according to Eq. 4.1. Thus, $\mathrm{SNR}_T$ will be maximum for TE equal to $\mathrm{T}_2^*$. A relatively flat minimum in the variance is expected for TE values around $\mathrm{T}_2^*$. At TE values lower than 0.5 $\mathrm{T}_2^*$, the accuracy of MR thermometry deteriorates markedly.

Two classes of pulse sequences have been compared (see diagrams in Fig. 4.2): (1) An echo-shifted (ES) FLASH sequence with one gradient echo per TR with optional echo shifting over one or more TR periods [15]; and (2) a PRESTO sequence with acquisition of five gradient echoes per TR period and echo shifting (optional) of the complete echo train [16]. Artifacts due to susceptibility and off-resonance effects in the PRESTO sequence were minimized, using a single polarity readout. Both sequences were used without and with echo shifting over one and two TR periods.

Experiments were performed on a 4.7 T Omega CSI animal instrument (General Electric, Milwaukee, Wisconsin) with a 40 cm bore. A fluorescent probe (model 3000, Luxtron, Santa Clara, California) was used as an additional temperature reference. A tube filled with 0.5%, w/v, agarose gel (GibcoBRL *ultra*PURE, Life Technologies, Gaithersburg, Maryland) with 0.067 m*M* $\mathrm{MnCl_2}$ (Fischer Scientific, Fair Lawn, New Jersey) ($\mathrm{T}_2^*$, approx. 100 milliseconds; $\mathrm{T}_1$, approximately 1.4 seconds) was heated from the inside using flowing water (see Fig. 4.3a). The temperature of the flowing water was regulated using a thermostatic circulator (2219 multitemp II, LKB, Bromma, Sweden). MR temperature imaging was performed with RF-spoiled (quadratic phase cycling over eight RF pulses), gradient-echo imaging with TE values ranging from 3 to 150 ms. At least 20 dummy scans were used to reach a steady state. All data were acquired with a 64 × 60 image matrix, 0.56 × 0.56 mm in-plane resolution, and a slice thickness of 5.0 mm. Flip angle was 13° except where stated otherwise.

Data were processed off-line on SUN-SPARC workstations (Sun Microsystems, Mountain View, California) using IDL processing software (Research Systems, Boulder, Colorado). All (ES-)FLASH data were filtered in read-out and phase encode dimensions (cosine filter, central 60% unfiltered), then Fourier transformed. Phase images were calculated, and phase unwrapping [17] was applied to the selected region of interest (ROI) to remove $2\pi$ discontinuities. The phase-difference image was then calculated and converted into a temperature image using the PRF temperature dependence, TE, and the starting temperature indicated by the fluoroptic probe as additional parameters. Multi-gradient-echo data were handled in a similar way, with the following exceptions. First, k-space was reconstructed from the raw data. Data were then Fourier transformed in the readout direction, after which zero- and first-order phase correction was performed. The internal-reference scan (one echo train acquired without phase encoding) present in each data set was used for this phase correction. In order to preserve the temperature-dependent phase difference between reference and heated data, the identical reference-phase

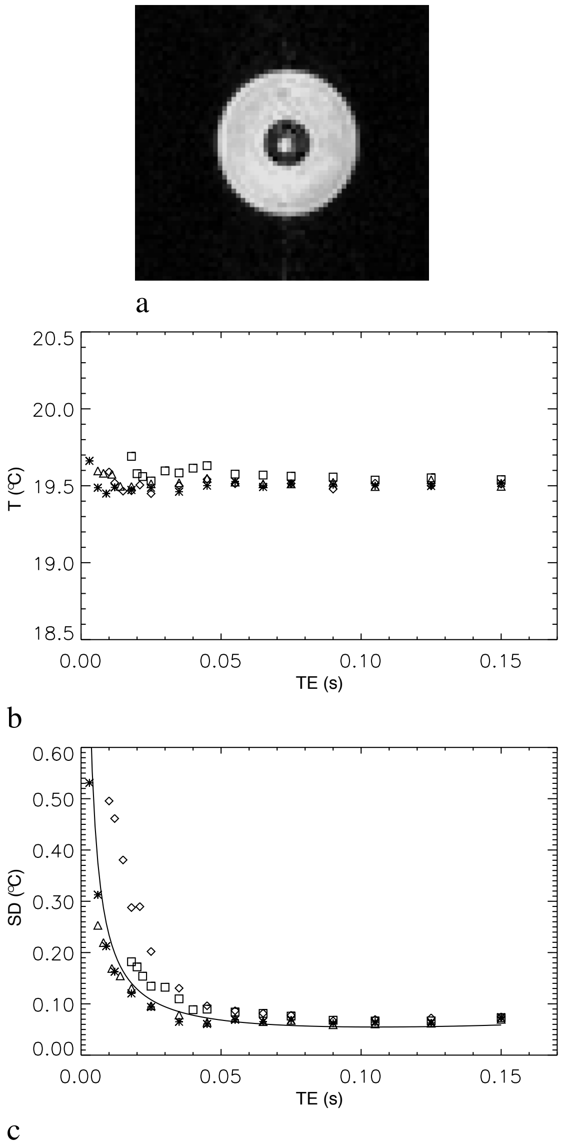

Figure 4.3: *(a) PRESTO image of one of the samples used, acquired with one TR shift. TR = 12 ms, TE = 18 ms (total imaging time 144 ms). Field of view = 36.0 × 33.8 mm, image matrix = 64 × 60 (in-plane resolution approximately 0.56 × 0.56 mm). Slice thickness 5 mm; (b) Average temperature in ROI (comprising approximately 100 voxels). Standard FLASH (∗), ES-FLASH with one TR shift (◇), and PRESTO without TR shift (△) and with one TR shift (□). (c) SD of the temperature found in the ROI. Data shown are an average over four identical data sets. Note that SD values are calculated for a ROI (SD for a single image), since the temperature stability of the magnet bore is insufficient to determine the accuracy in temperature imaging using the SD per voxel over many images.*

correction was also applied to the data obtained after temperature elevation. After phase correction, filtering and Fourier transformation was applied in the phase-encode direction.

The temperature dependence of the PRF was determined using multi-gradient-echo data without echo shifting acquired at echo times varying from 6 to 180 ms, both at 14.5 and 34.7°C. Linear regression of the average phase difference in a selected ROI yielded the value of 2.51 rad·$T^{-1}$·°$C^{-1}$·$s^{-1}$. This value was used in all subsequent experiments.

Figure 4.3 shows an overview of the thermometry results obtained with the different pulse programs as a function of TE. The temperature data shown are an average over the ROI (defined as part of an annulus of the cylinder shown in Figure 4.3a). All pulse sequences resulted in an average temperature which corresponds closely with the temperature as measured with the fluoroptic probe (generally within 0.1-0.2°C). The standard deviation (SD) reflects the spread of temperature within the voxels of this ROI. The TE dependence of the SD shows a broad minimum around the $T_2^*$ value of 100 ms as expected from Fig. 4.1.

Table 4.1 gives a further demonstration of the improved SD of the temperature upon echo shifting when very short TR values are used. Echo shifting was limited to a maximum of two TR periods. Table 4.1 shows that SD of 0.1-0.2°C were reached for image SNR values of approximately 50 and TE values between 14 and 54 ms. Note that a total imaging time of only 144 ms was used for PRESTO data given in the first row of Table 4.1b, and as shown in the image of Fig. 4.3. The experimentally determined SD values were generally a factor 1.5 to 2.0 higher than the theoretical values based on Eq. 4.1. We attribute this to small temperature gradients over the ROI.

Data given in Table 4.1 and Fig. 4.3 were obtained with a fixed flip angle of 13° corresponding with the Ernst flip angle for a TR of 36 ms. Experiments shown in Fig. 4.3 were repeated with 5°, 10°, 15°, and 20° flip angles. The calculated temperature was identical (data not shown). The SD values varied according to the SNR of the images corresponding to the theoretical curve in Fig. 4.1.

Although the PRF method is rather independent of protein and membrane content, it is based on the chemical shift of water hydrogens only. Lipid resonances are, at first approximation, independent of temperature. Therefore, lipid signals must be suppressed *in vivo* for an accurate temperature measurement. Lipid suppression in MRI is generally achieved using a Dixon-type second experiment with a delay leading to a $\pi$ shift in phase of the dominating lipid signal [18]. Addition of the data of both experiments leads to removal of the lipid signals in case of a homogeneous magnetic field. To avoid an increase of the total imaging time following temperature elevation, the reference data (with a $\pi$ phase shift) obtained during the "cold" experiment can be used to correct the data acquired during heating. This is demonstrated in Fig. 4.4. Data were acquired using a 0.5% agarose sample with a 78/22 v/v mixture of water and dioxane. The water-soluble dioxane gives a single proton resonance at 200 Hz from the water line at 4.7 T and is used to mimic the influence of lipids. The chemical-shift difference with respect to water is about equal to that of the dominant resonance of lipids at 1.5T. The data shown in Fig. 4.4 were analyzed with and without fat suppression based on the method described above. The dioxane causes a modulation of the calculated temperature when it is not suppressed. The modulation frequency corresponds with the difference in Larmor precession frequency.

Note that the "lipid" suppression was achieved without a time penalty after temperature elevation. The procedure of using the cold reference data for fat suppression following temperature elevation reduces the phase accumulation of the water hydrogens as a result of heating by a factor of two. The results of Figure 4.4 have been corrected for this effect. Thus, lipid suppression

| TR [ms] | Number of TR shifts | TE [ms] | Temperature [°C] | SD [°C] | Imaging time [s] |
|---|---|---|---|---|---|
| (a) Results of MR temperature imaging using (ES)-FLASH | | | | | |
| 12 | 0 | 6 | 19.9 | 0.44 | 0.72 |
| 12 | 1 | 18 | 19.8 | 0.25 | 0.72 |
| 12 | 2 | 30 | 19.7 | 0.19 | 0.72 |
| 20 | 0 | 14 | 19.7 | 0.18 | 1.2 |
| 20 | 1 | 34 | 19.7 | 0.16 | 1.2 |
| 20 | 2 | 54 | 19.8 | 0.15 | 1.2 |
| 60 | 0 | 54 | 19.7 | 0.05 | 3.6 |
| 60 | 1 | 114 | 19.7 | 0.11 | 3.6 |
| 60 | 2 | 174 | 19.7 | 0.17 | 3.6 |
| (b) Results of MR temperature imaging using PRESTO | | | | | |
| 12 | 0 | 6 | 19.6 | 0.28 | 0.14 |
| 12 | 1 | 18 | 19.5 | 0.19 | 0.14 |
| 12 | 2 | 30 | 19.5 | 0.15 | 0.14 |
| 20 | 0 | 14 | 19.6 | 0.16 | 0.24 |
| 20 | 1 | 34 | 19.5 | 0.11 | 0.24 |
| 20 | 2 | 54 | 19.6 | 0.10 | 0.24 |
| 60 | 0 | 54 | 19.7 | 0.05 | 0.72 |
| 60 | 1 | 114 | 19.7 | 0.11 | 0.72 |
| 60 | 2 | 174 | 19.7 | 0.17 | 0.72 |

Table 4.1: *Note. SNR for the FLASH images was approximately 50 for TR 12 ms, 55 for TR 20 ms, and 60 for TR 60 ms without echo shifting. SNR for the PRESTO images was approximately 70 for TR 12 ms, 60 for TR 20 ms, and 60 for TR 60 ms without echo shifting. Note that data for Figure 4.3 and Table 4.1 were obtained on different days.*

can be achieved without a time penalty after temperature elevation. An alternative procedure for lipid suppression is to calculate the lipid image from the two cold images, and then use the lipid image to eliminate lipid signal in the original cold and "warm" images. This procedure leads to similar results.

In conclusion, this study has demonstrated that MR temperature imaging based on the water proton frequency is accelerated drastically with very short TR periods using the echo-shifting principle and further using multiple gradient echoes per TR in combination with echo shifting. Very short TR periods in echo-shifted FLASH and PRESTO lead to correct temperature maps, indicating that stimulated echoes and spin echoes do not lead to systematic deviations in the calculated temperature. Lipid suppression is incorporated in temperature imaging with (ES-)FLASH and PRESTO, using a second scan according to the Dixon method. This lipid suppression is obtained without time penalty following temperature elevation. Thermometry precision depends on TE when using the proton frequency. A rather flat minimum is found for the SD for TE close to $T_2^*$ corresponding with theoretical analysis. A SD of 0.1-0.2°C was routinely obtained for a total imaging time of 144 ms (0.56 mm in-plane resolution).

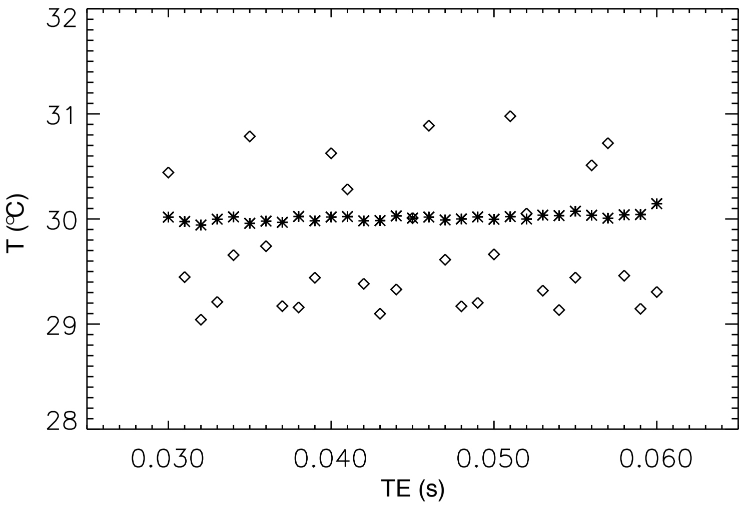

Figure 4.4: *MR temperature measurement using the PRF method on a 0.5% agarose sample with a 78/22, v/v, mixture of water and dioxane without (◇) and with (∗) Dixon type "lipid suppression". The reference data for the lipid suppression following temperature elevation were obtained from the reference scan acquired during the cold experiment.*

Note that the principles demonstrated in this paper are equally valid for the analysis of phase accuracy in gradient-echo-based phase imaging. For example, 3D phase maps are now used for shimming the main magnetic field. The generation of such maps can be accelerated drastically using the principles described in this paper.

## Acknowledgement

The authors thank Alan Olson for technical support.

## References

[1] P.P. Lele, A simple ethod for production of trackless focal lesions with focused ultrasound. *J. Physiol.* **160**, 494-512 (1962)

[2] F.J. Fry, L.K. Johnson, Tumor irradiation with intense ultrasound. *Ultrasound Med. Biol.* **4**, 337-341 (1978)

[3] D.L. Parker, V. Smith, P. Sheldon, L.E. Crooks, L. Fussell, Temperature distribution measurements in two-dimensional NMR imaging. *Med. Phys.* **10**, 321 (1983)

[4] F.A. Jolesz, P.D. Jakab, Acoustic pressure wave generation within an MR imaging system: potential medical applications. *Magn. Reson. Imaging* **1**, 609-613 (1991)

[5] H.E. Cline, J.F. Schenck, K. Hynynen, R.D. Watkins, S.P. Souza, F.A. Jolesz, MR-Guided focused ultrasound surgery, *J. Comput. Assist. Tomogr.* **16**, 956-965 (1992)

[6] R.J. Dickinson, A.S. Hall, A.J. Hind, I.R. Young, Measurement of changes in tissue temperature using MR imaging. *J. Comput. Assist. Tomogr.* **10**, 468-472 (1986)

[7] D. Le Bihan, J. Delannoy, R.L. Levin, Temperature mapping with MR imaging of molecular diffusion: application to hyperthermia. *Radiology* **171**, 853 (1989)

[8] Y. Ishihara, A. Calderon, H. Watanabe, K. Mori, K. Okamoto, Y. Suzuki, K. Sato, K. Kuroda, N. Nakagawa, S. Tsutsumi, A precise and fast temperature mapping method using water proton chemical shift, in "Proc., SMRM, 11th annual meeting, Berlin, 1992", p. 4803

[9] K. Kuroda, Y. Miki, N. Nakagawa, S. Tsutsumi, Non-invasive temperature mapping based upon NMR procedure. In: "Macroscopic and microscopic heat and mass transfer in biomedical engineering", 199-217, International center for heat and mass transfer, Belgrade, 1992

[10] K. Kuroda, K. Abe, S. Tsutsumi, Y. Ishihara, Y. Suzuki, K. Sato, Water proton magnetic resonance spectroscopic imaging. *Biomed. Thermol.* **13**, 43-62 (1993)

[11] J. De Poorter, C. De Wagter, Y. De Deene, C. Thomsen, F. Ståhlberg, E. Achten, Noninvasive MRI thermometry with the proton resonance frequency (PRF) method: *in vivo* results in human muscle. *Magn. Res. Med.* **33**, 74-81 (1995)

[12] J. de Poorter, C. de Wagter, Y. de Deene, C. Thomsen, F. Ståhlberg, E. Achten, Proton-resonance-frequency-shift method compared with molecular diffusion for quantitative measurement of two-dimensional temperature distribution in a phantom. *J. Magn. Reson. B* **103**, 234 (1994)

[13] J.C. Hindman, Proton resonance shift of water in gas and liquid states. *J. Chem. Phys.* **44**, 4582-4592 (1965)

[14] C.T.W. Moonen, G. Liu, P. van Gelderen, G. Sobering, A fast gradient-recalled MRI technique with increased sensitivity to dynamic susceptibility effects. *Magn. Res. Med.* **26**, 184-189 (1992)

[15] G. Liu, G. Sobering, A.W. Olson, P. van Gelderen, C.T.W. Moonen, Fast echo-shifted gradient-recalled MRI: combining a short repetition time with variable $T_2^*$ weighting. *Magn. Res. Med.* **30**, 68-75 (1993)

[16] G. Liu, G. Sobering, J. Duyn, C.T.W. Moonen, A functional MRI technique combining principles of echo-shifting with a train of observations (PRESTO). *Magn. Res. Med.* **30**, 764-768 (1993)

[17] G.S. Sobering, Y. Shiferaw, P. van Gelderen, C.T.W. Moonen, Quantitative measurement of the phase error for a simple and rapid phase-unwrapping algorithm, in "Proc., ISMRM, 3rd annual meeting, Nice, 1995", p. 661

[18] W.T. Dixon, Simple proton spectroscopic imaging. *Radiology* **153**, 189-194 (1984)

# Chapter 5

# Lipid Suppression

## Contents

**5.1 Introduction** **61**

**5.2 Materials and methods** **61**

5.2.1 In vitro experiments 63

5.2.2 In vivo experiments 64

**5.3 Results and discussion** **66**

5.3.1 In vitro studies 66

5.3.2 In vivo studies 68

**5.4 Conclusions** **70**

Jacco A. de Zwart, Frédéric C. Vimeux, Christophe Delalande, Paul Canioni, Chrit T.W. Moonen
”Fast Lipid-Suppressed MR Temperature Mapping with Echo-Shifted Gradient-Echo Imaging and Spectral-Spatial Excitation”
*Magnetic Resonance in Medicine* **42**, 53-59 (1999)

## Abstract

The water proton resonance frequency (PRF) is temperature dependent and can thus be used for magnetic resonance (MR) thermometry. Since lipid proton resonance frequencies do not depend on temperature, fat suppression is essential for PRF based temperature mapping. The efficacy of echo-shifted (TE $>$ TR) gradient-echo imaging with spectral-spatial excitation is demonstrated, resulting in accurate and rapid, lipid suppressed, MR thermometry. The method was validated on phantoms, fatty duck liver, and rat thigh, demonstrating improvements in both the speed and precision of temperature mapping. Heating of a rat thigh with focused ultrasound was monitored in vivo with an accuracy of 0.37°C and a time resolution of 438 msec.

## 5.1 Introduction

Recent trends in health care toward minimally invasive and image-guided procedures have accelerated the development of interventional MRI. Using laser [1], radiofrequency (RF) [2, 3] or focused ultrasound (FUS) approaches [4-8], tissue can be heated at selected locations within the body. MRI is considered an excellent monitor of thermotherapy since it provides both detailed anatomical information for target definition and accurate temperature maps. The latter is important for dosimetry of the energy deposition and, in the case of FUS, for adjusting the focus to the target location. Two FUS-MRI applications are under investigation: a) The ablation of tumors in soft tissue [6-8]; and b) The activation of genes under control of the temperature dependent heat shock protein (HSP) promoter [9, 10].

Three parameters have been suggested for MR temperature mapping: a) The spin-lattice relaxation time $T_1$ [2,11-14]; b) the molecular diffusion constant $D$ [15]; and c) the resonance frequency of water protons [16, 17]. It has been shown that, in contrast to $T_1$- and $D$-based methods, the relation between the water proton resonance frequency (PRF) and the temperature is, to a first approximation, tissue independent ($\sim$0.01 ppm·K$^{-1}$) [18, 19]. For this reason the PRF method was chosen for the present study.

A temperature map based on the PRF method can be calculated from the phase difference obtained from two gradient-echo images [16]. Theoretical as well as experimental studies in phantoms [1, 20, 21] and in vivo [22, 23] have shown that the optimal echo time (TE) for thermometry based on the water PRF equals the $T_2^*$ value of the sample; however, the need for very fast imaging during medical interventions requires a short repetition time (TR). The conflicting requirements of a long TE and a short TR can be resolved through the use of echo shifting, which leads to gradient echo imaging with TE $>$ TR [24, 25]. In this study we incorporated echo shifting in a standard fast low-angle shot (FLASH) and a multi-shot echoplanar imaging (EPI) sequence; the resulting gradient-echo sequences are referred to as echo-shifted (ES) FLASH and principles of echo shifting with train of observations (PRESTO) [26], respectively.

An important problem for PRF temperature measurements is that the lipid resonance frequencies are not temperature dependent. The presence of lipids modifies the phase difference obtained in the thermometry experiment and thus leads to thermometry errors. To overcome this problem, lipid suppression was incorporated into both ES-FLASH and PRESTO sequences. Fat-suppressed MRI was originally introduced by Dixon [27], who exploited phase-sensitive techniques to generate both water and lipid images. For temperature mapping based on water PRF, the generation of a separate lipid image is unnecessary, allowing one to use specially designed RF excitation pulses that take advantage of the difference in resonance frequency between water and fat to avoid excitation of the lipid signal. In this work a binomial pulse is used for fat-suppressed slice-selective excitation whose design is similar to that of previously presented spectral-spatial pulses [28, 29]. MR thermometry with the new methods was validated with conventional heating on phantoms using a thermocouple as a reference. The approach was then tested in vivo with FUS heating of rat thigh muscle.

## 5.2 Materials and methods

All experiments were performed on a Bruker Biospec animal instrument (Bruker, Ettlingen, Germany) with a 50 cm bore, 4.7 T magnet equipped with a shielded gradient insert (120 mm diameter, 0.193 T·m$^{-1}$). Data were processed off-line using IDL (RSI, Boulder, CO) running on

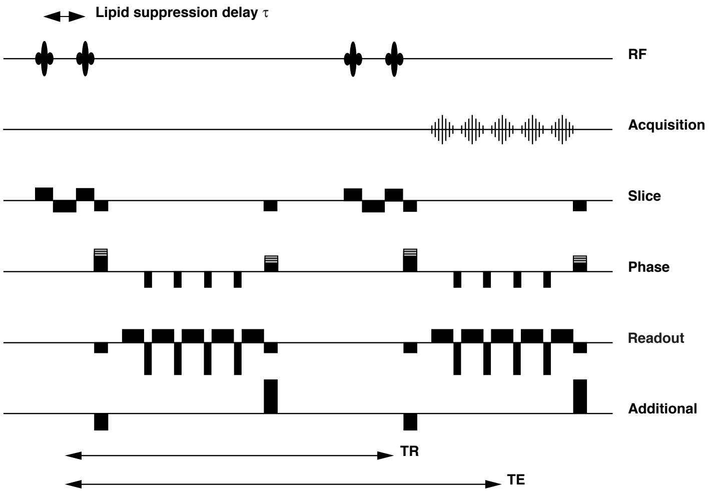

Figure 5.1: *Schematic representation of the PRESTO sequence, a multi-shot EPI technique combining the acquisition of multiple lines of k-space with echo shifting (TE > TR). A spectral-spatial (slice-selective binomial) pulse is used for lipid suppression. A unipolar read-out gradient serves to minimize artifacts. Note that the additional gradients serve to dephase unwanted coherence pathways, whereas the magnetization excited by the RF excitation of the previous TR period is properly rephased. The k-space trajectory is fully discussed in ref. 26.*

Silicon Graphics workstations (Mountainview, CA). Phase images were calculated, and phase unwrapping was applied in the selected region of interest to remove 2π discontinuities [30].

Gel samples, 6 g/l agar (Difco, Detroit, MI) in a 25:75 v/v mixture of dioxane and 0.092 mM $MnCl_2$ in water (Merck, Darmstadt, Germany), were used to test lipid suppression. Dioxane has a single resonance frequency, independent of temperature, and was used to simulate the lipid signal since its resonance frequency offset at 4.7 T (1.0 ppm, 200 Hz) is comparable to the frequency offset of body fat at 1.5 T (3.5 ppm, 220 Hz), resulting in equivalent suppression parameters.

Heated agar gel was poured into the outer of two concentric cylinders and allowed to harden. The temperature of the gel was then regulated using water flowing through the inner cylinder, controlled by a Haake F3 thermostatic circulator (Haake, Karlsruhe, Germany). A Physitemp IT-23 thermocouple (Physitemp, Clifton, NJ), connected to a Cole Parmer 91100-50 thermometer (Cole Parmer, Vernon Hills, IL), was introduced into the gel to provide a temperature reference. The thermocouple (accuracy 0.1°C) was placed 2 cm from the image plane to avoid susceptibility artifacts. In this study we used a temperature dependence of the image phase of 2.51 $rad{\cdot}s^{-1}{\cdot}T^{-1}{\cdot}K^{-1}$) (corresponding to a PRF temperature dependence of 0.0094 $ppm{\cdot}K^{-1}$), as empirically determined in previous work [20]. A temperature reference was not used for the FUS experiments, since a thermocouple in the focal point will interfere with the FUS beam.

ES-FLASH and a PRESTO sequences, both incorporating the spectral-spatial pulse excitation, were used in all experiments. The PRESTO sequence is shown in Fig. 5.1. The spectral-spatial excitation pulse consists of a binomial slice-selective RF pulse with two components separated by a delay τ. This pulse leads to full excitation of spins on resonance and zero excitation of spins with a (1+2$n$)/2τ frequency offset (where $n$ is an integer number) [31]. All experiments were performed with quadratic phase cycling [32] over 8 RF pulses, to remove transverse coherences.

Echo shifting (TE > TR) was achieved using a gradient pulse combination as described previously [33]. Spins excited by the $n^{th}$ RF pulse (or spectral-spatial pulse in the case of lipid suppression) are dephased by an additional gradient pulse of amplitude $M$. At the end of the TR period, an additional gradient pulse with identical duration but amplitude -2$M$ is applied. The first additional gradient pulse of magnitude $M$ in the next TR period then rephases the spins excited in the previous TR period while dephasing those excited by the $(n+1)^{th}$ RF pulse. For more details the reader is referred to refs. 24 and 25.

### 5.2.1 In vitro experiments

The following parameters were used for agar gel experiments: a 64 × 60 matrix; a slice thickness (ST) of 5.0 mm; a field of view (FOV) of 48 × 45 mm, resulting in a voxel size of 0.8 × 0.8 × 5.0 mm; a spectral width (SW) of 100 kHz. TE values ranged from 35.0 to 42.3 msec for the comparison of ES-FLASH and PRESTO sequences (gel $T_2^*$ was 35 msec). The TR was 50.0 msec in the FLASH experiments and 26.0 msec for PRESTO. In PRESTO, 5 echoes were acquired per TR period. The water peak was put on-resonance and data were acquired with a spectral-spatial pulse with a delay τ of 2427 $\mu$sec, leading to dioxane suppression at a temperature of approximately 17°C. In a second series, the delay τ was increased to 4854 $\mu$sec, resulting in full excitation of dioxane. For the thermometry experiment, PRESTO with a TR of 24.0 msec was used in combination with TE values ranging from 33.0 to 38.7 msec and suppression delays τ of 2500 (optimal suppression at 20.4 °C) and 5000 $\mu$sec. Since the transmit frequency is set according to the temperature-dependent water resonance frequency in the reference scan, the optimum value of the delay τ for complete suppression of the temperature-insensitive lipid signal will depend on the absolute temperature of the reference scan. Note that, once transmit frequency and delay τ have been fixed, the quality of fat suppression will not depend on the actual temperature. Binomial excitation does, however, result in a small, temperature-dependent suppression of the water signal, resulting from the change in water PRF with temperature. This effect (0.17% signal loss at 1.5 T for a temperature increase of 10°C) has no effect on the measured temperature but will slightly reduce the signal-to-noise ratio (SNR) of the phase map and thus the precision of the MR thermometry. Note that the method described here does not account for possible temperature-dependent changes in volume susceptibility.

The quality of lipid suppression was also examined for duck liver (*foie gras du canard*, Dubernet, Bordeaux, France) with a high fat content (approximately 57%, as determined by MR spectroscopy). The liver tissue was inserted into the outer of the two concentric cylinders as described for the agar gel samples. Data were acquired both with and without echo shifting over one TR period, using otherwise identical imaging parameters (matrix 64 × 60, FOV 48 × 45 mm, ST 5.0 mm). The TE values ranged from 9.0 to 11.9 msec (FLASH, TR of 50.0 msec) and 12.0 to 13.4 msec (ES-FLASH, TR of 8.5 msec). Both FLASH and ES-FLASH data were acquired with a delay τ of 2033 $\mu$sec (optimal suppression at 13.7°C). Due to hardware restrictions, a τ of 678 $\mu$sec, the shortest suppression delay resulting in lipid suppression, was not possible. The delay τ of 2033 $\mu$sec results again in complete cancellation of lipid signal. The FLASH experiments were repeated with a delay τ of 2710 $\mu$sec, resulting in no lipid suppression.

### 5.2.2 In vivo experiments

The performance of the lipid-suppressed ES-FLASH and PRESTO sequences for temperature mapping was also tested during heating of tissue using FUS. A polycarbonate rat holder was constructed that contained both the FUS transducer and an MR surface coil, a design similar to that described in ref. 10. The holder was placed in a Plexiglas tube that was partially filled with water. The temperature of the water in the rat holder was regulated using a thermostatic circulator, to maintain the body temperature of the animal at approximately 35°C. The ultrasound passes through a 38 mm aperture in the platform supporting the animal. The holder was inclined to insure that the rat hind leg was under water while the head was maintained above water. The leg was supported by four 2-0 braided polyester fiber sutures, forming a grid across the aperture. The FUS transducer was positioned so that the focus was approximately 10 mm into the rat thigh. Male Wistar rats ($n$ = 11, weight 425-575 g) were anesthetized using halothane (1%) and heated under an approved protocol. The FUS transducer (Specialty Engineering Associates, Soquel, CA) was 38 mm in diameter, with a radius of curvature and nominal focal length of 25 mm. The resonance frequency was 1.45 MHz. A Kalmus 170/KMP amplifier (Kalmus, Bothell, WA) was used to drive the FUS transducer. A Yokogawa FG-110 function generator (Yokogawa, Tokio, Japan) was used as a low-power signal source. Reflecting power was monitored using a 4410A W meter with 4410-2 element (Bird, Cleveland, OH). The transmit/receive surface coil was potted with epoxy in a 58 mm diameter channel cut in the platform around the FUS aperture. Tuning and matching capacitors were housed well above the water and above the rat. The animals were sacrificed after the experiment.

Local shimming was performed using three-dimensional (3D) phase information in a selected volume of interest (VOI). A thick-slice 3D FLASH experiment was repeatedly performed with TE values starting from 3 msec and increasing in 1 msec intervals up to 10 ms. After each step a first-order phase correction was calculated from the unwrapped phase data. This phase correction was used to adjust the first-order shims X, Y, and Z. In experiments with spectral-spatial excitation, the two components of the RF pulse have half the amplitude compared to the amplitude used in non-fat-suppressed slice-selective excitation. The following parameters were used for in vivo studies using FLASH: a 64 × 64 matrix; an FOV of 80 × 80 mm; an ST of 5.0 mm, resulting in a voxel size of 1.3 × 1.3 × 5.0 mm; and an SW of 100 kHz. TR was 15 msec in all experiments. The flip angle was approximately 15° in the focal region but was location dependent due to the use of a transmit/receive surface coil. One hundred ninety-two consecutive images were acquired following the acquisition of eight dummy scans. FUS heating (frequency 1.45 MHz, 11.4 W electrical power) was applied starting 10 sec after the end of the dummy acquisitions and lasting for 55 sec. Temperature was monitored using FLASH with spectral-spatial or non-fat-suppressed excitation. A 10 min interval between the experiments allowed the tissue to cool down. The acquisition time per image was 960 msec, resulting in a total monitoring time of about 3 min. The first image was used as the reference image for all following images. For in vivo ES-FLASH studies, 384 images were acquired with the following parameters: a 64 × 60 matrix; an FOV of 80 × 75 mm, resulting in a voxel size of 1.3 × 1.3 × 5.0 mm; and an SW of 100 kHz. FUS with an amplitude of 11.4 W electrical power was applied for 50 sec, starting 10 sec into the experiment. The short muscle $T_2^*$ values at 4.7T (approximately 20 msec at the resolution used) prevented a meaningful use of the PRESTO sequence.

To obtain information about lipid content and lipid offset frequency, 30 FLASH experiments (without spectral-spatial excitation) with TE values starting from 3.5 msec and increasing in

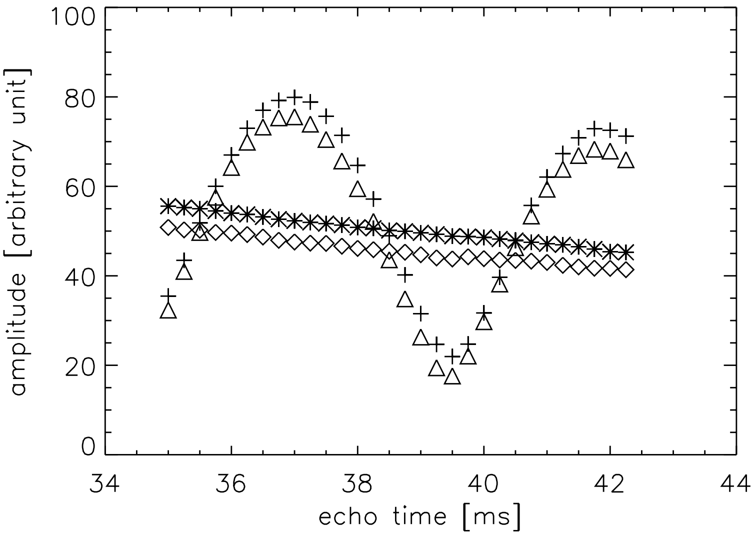

a

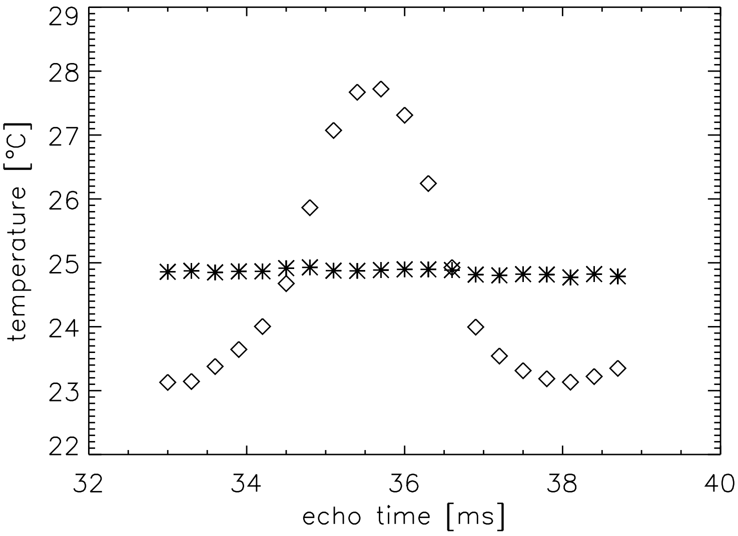

b

Figure 5.2: *a) Comparison of total signal amplitude as a function of echo time using data acquired with both optimal and non-suppressed FLASH (TR 50 msec, 3000 msec imaging time) and PRESTO (TR 26 msec, 312 msec imaging time) sequences. Data were acquired in an agar gel phantom containing 25% dioxane to simulate the lipid signal. FLASH: ∗, optimal suppression; +, non-suppressed. PRESTO: ◇, optimal suppression; △, non-suppressed. Data shown represent the average signal in a region of interest (ROI) comprising 581 voxels. b) Thermometry results for the same sample. Data measured in a 621 pixel ROI in images from PRESTO with optimal (∗) and no (◇) suppression of the dioxane signal. The reference temperatures as indicated by a thermocouple were 20.4 and 24.9 °C, respectively.*

0.1 msec intervals were acquired. A repetition time of 25 msec was used; all other parameters were identical to those used during the FUS monitoring. Sinusoidal fits to both the real and the imaginary part of these data as a function of echo time were used to estimate both the fat offset frequency and the percentage of fat. Since local shimming was applied, no correction for field inhomogeneity was used in the fat suppression procedure.

## 5.3 Results and discussion

### 5.3.1 In vitro studies

The signal amplitude of the water/dioxane phantom as a function of TE is shown in Fig. 5.2a for FLASH and PRESTO data. In case of well-adjusted "dioxane suppression" the signal decays as a function of TE only due to $T_2^*$ relaxation of the gel. In the case of no suppression, an oscillation of the total signal amplitude is observed due to the varying phase difference relationship between the water and dioxane components of the magnetization. The periodicity of this modulation was approximately 5 msec, corresponding to a difference of 200 Hz in resonance frequencies of water and dioxane at 4.7 T. The time used for the acquisition of one image was 3000 msec for the FLASH data and 312 msec for PRESTO. The comparability of these data demonstrates that the use of echo shifting does not effect the binomial excitation.

Using the PRESTO sequence, MR gradient-echo images of the water/dioxane sample with and without dioxane suppression were acquired using a range of echo times, with each set of images being acquired at two temperatures. The calculated temperature as a function of TE is given in Fig. 5.2b, demonstrating that the calculated temperature was independent of TE in the case of optimally adjusted dioxane suppression and corresponded with the thermocouple reference temperature. However, in case of no suppression, large TE-dependent deviations in the calculated temperature can be seen. At an echo time of 33 msec the SNR of the phase maps was 35.7 in the optimally suppressed data. The theoretical variance in the temperature for data with this SNR and TE is 0.05°C (at 4.7 T). A standard deviation (SD) of 0.11°C was found within an ROI containing 98 voxels. The discrepancy between the theoretical variance and experimental accuracy has been previously explained by the presence of a small temperature gradient within the ROI (20).

Results obtained during heating of the liver tissue are shown in Fig. 5.3a. Data were acquired at 13.7 and 17.7°C as measured using a thermocouple. Without suppression of fat signal, deviations of up to 13°C from the actual temperature are found. With a suppression delay $\tau$ that was optimized to suppress excitation of magnetization at 738 Hz off-resonance (the average lipid offset frequency as measured using MR spectroscopy), the correct temperature was calculated. In Fig. 5.3b, a simulation of this experiment is shown, based on the following parameters: 57% lipid content; 738 Hz lipid frequency offset; 13.7°C reference temperature; and 4.0°C temperature rise. The simulation demonstrates reasonable agreement with the experimental data and confirms the large, TE-dependent errors in temperature when using non-fat-suppressed data. Note also that the minima in the simulated data are shifted approximately 100 $\mu$sec to the left compared with the experimental data, indicating that the actual average lipid frequency offset was about 10 Hz lower than the 738 Hz that was used for simulation. The SNR was 8.5 for FLASH data with a TE of 9.0 msec and 5.8 for ES-FLASH data with TE 12.0 msec.

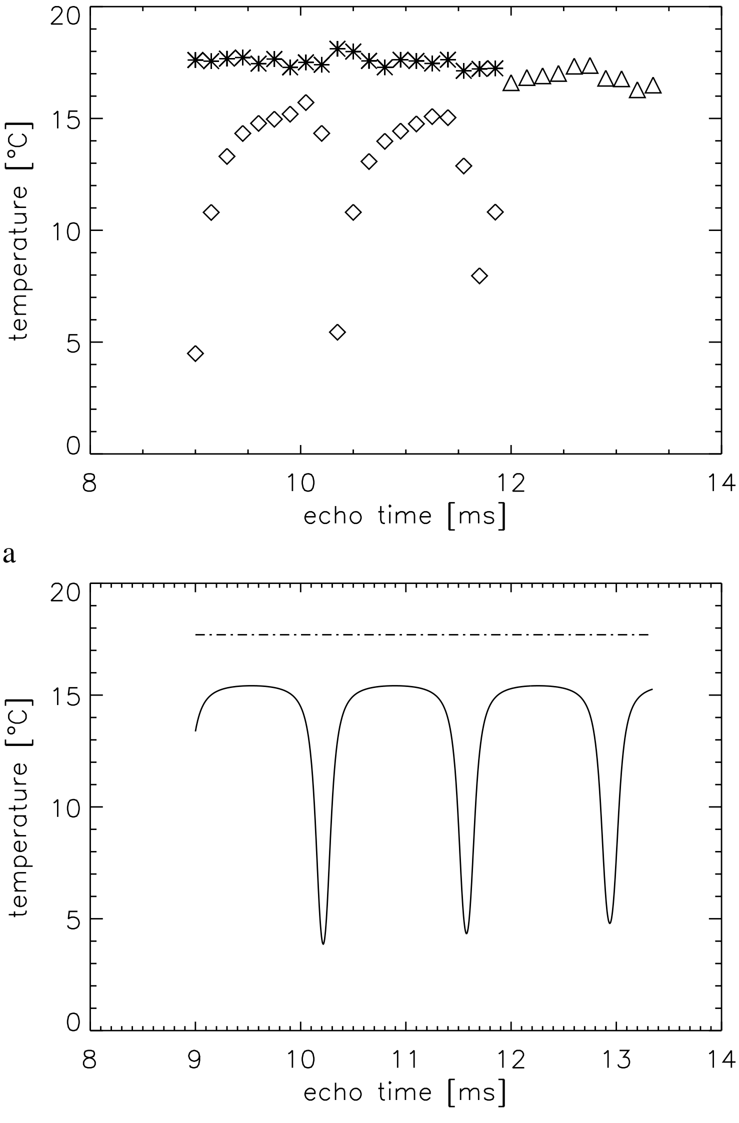

a

a

Figure 5.3: *a) Thermometry results for duck liver with a 57% lipid content and a* $T_2^*$ *value of 8 msec. Temperatures shown are averaged over a ROI comprising 136 voxels. FLASH data were acquired with an optimal lipid suppression delay* $\tau$ *(*$*$*) and a delay* $\tau$ *resulting in no suppression of the lipid signal (*$\Diamond$*). ES-FLASH data (*$\triangle$*) were acquired with an optimal delay* $\tau$ *only. Thermocouple reference temperatures were 13.7° and 17.7°C. b) Simulation of PRF thermometry data for a voxel containing 57% lipid spins, which are 738 Hz off-resonance with a temperature rise from 13.7° to 17.7°C. The solid line is a simulation for no lipid suppression; the broken line represents lipid-suppressed data.*

### 5.3.2 In vivo studies

Figure 5.4 displays the focal point temperature measured in vivo during and after FUS heating of a rat thigh muscle. Figure 5.4a shows results obtained with the non-fat-suppressed gradient echo imaging; Fig. 5.4b shows identical experiments but with spectral-spatial excitation ($\tau$ = 2419 $\mu$sec). When applying a constant-intensity FUS beam to tissue, the evolution of the temperature in the focal point can be described as [7]:

$$T_t = A \cdot ln\left(1 + \frac{t}{\tau_r}\right) + T_0 \tag{5.1}$$

where $T_t$ is the temperature at time $t$ after the start of the FUS application, $\tau_r$ the time constant for radial diffusion, and $T_0$ the initial temperature. $A$ is a constant depending on, amongst other parameters, the absorbed heat. After switching off the FUS source, the focal point temperature decays to the original temperature due to diffusion, which can be described as:

$$T_t = A \cdot ln\left[\left(1 + \frac{t}{\tau_r}\right) \Big/ \left(1 + \frac{t - t_0}{\tau_r}\right)\right] + T_0 \tag{5.2}$$

Where $t_0$ is the time at which the FUS heating was started. This model does not account for physiological thermoregulatory mechanisms.

The data acquired at TE of 10 msec with spectral-spatial excitation were used for the fit shown in Fig. 5.4. Only those data acquired during FUS application were fitted using Eq. 5.1; the subsequent temperature decay was calculated using Eq. 5.2. A maximal temperature rise of 8.9°C was measured after 55 sec of FUS heating. The image SNR was 24.2, giving rise to a theoretical variance of 0.35°C in the calculated temperature for this echo time. Using the difference between the fitted and the actual data, a measured standard deviation of 0.42°C is calculated, which is in good agreement with the theoretical variance. For all animals ($n$ = 11), accuracy of the measurement was 0.47°C in the FUS focal point (average SD), which is in reasonable agreement with the theoretical variance based on the SNR. In the absence of lipid suppression (Fig. 5.4a), the observed temperature profile was TE dependent. For a TE of 9.7 msec, a maximal temperature rise of 12.7°C was calculated, in contrast to the 6.3°C maximum calculated for an echo time of 10.5 msec.

The results obtained in vivo with echo-shifted FLASH are summarized in Tables 5.1 and 5.2. In three voxels the temperature-induced signal changes during FUS heating were fitted to Eq. 5.1. The fitted maximum temperature rise is displayed in Table 5.1, while Table 5.2 compares the image SNR with the standard deviation (in the difference between fit and data) for the data acquired at echo time 11.4 msec. The results demonstrate good agreement between the accuracy of experimental temperature measurements and the temperature variance predicted on the basis of image SNR. Table 5.1 also shows the echo time dependency of the measurement when ES-FLASH without lipid suppression is used. Note that the TE dependence of temperature measurement is avoided when spectral-spatial excitation with optimal suppression delay is used.

The slice-selective binomial spectral-spatial pulse was chosen because of its small time penalty. Its efficacy to suppress lipids depends on the $B_0$ field homogeneity. Higher order

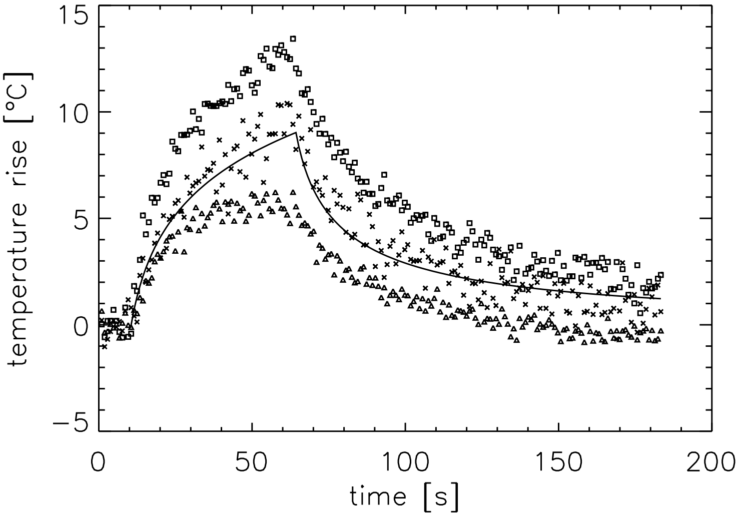

a

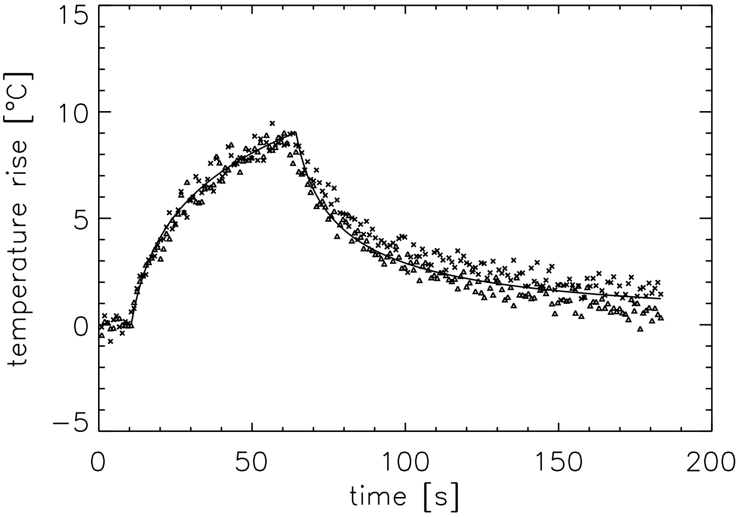

a

Figure 5.4: *Calculated temperature evolution in the focal point in rat thigh during in vivo FUS heating. One hundred ninety one temperature maps were calculated from continuously acquired gradient-echo data (960 msec per image). The FUS was applied between 10 and 65 sec into the experiment. A fat content of approximately 16% was calculated for the focal point voxel. a) Non-fat-suppressed gradient-echo imaging with TEs of 9.7 (□), 10.0 (×), and 10.5 (△) msec; b) Gradient-echo imaging with spectral-spatial excitation and TEs of 10.0 (×) and 10.5 (△) msec. The solid line in both figures represents a fit to the data acquired with lipid suppression at a TE of 10.0 msec (× in Fig. b).*

| Fat suppression | TE | $T_{max}$ | | |
|---|---|---|---|---|
| | | Focal point[a] | Voxel 1[b] | Voxel 2[c] |
| No | 11.0 | 9.0 | 8.8 | 1.9 |
| No | 11.4 | 9.4 | 10.8 | 3.0 |
| No | 11.7 | 8.8 | 11.2 | 4.0 |
| Yes | 11.0 | 8.9 | 8.5 | 2.7 |
| Yes | 11.4 | 8.9 | 8.0 | 2.5 |
| Yes | 11.7 | 8.9 | 8.9 | 3.3 |

*Data were acquired using ES-FLASH. A fit to the data was used to determine the maximal temperature rise.

[a] The focal point voxel contained a negligible amount of fat.

[b] Voxel 1 was located 3.8 mm above the focal point and contained approximately 9% fat.

[c] Voxel 2 was located at 4.5 mm from the focal point and contained about 22% fat.

Table 5.1: *Maximal temperature rise in three voxels in the thigh of a male Wistar rat during a 50 sec FUS heating period**

spectral-spatial pulses [28] may be less sensitive to field homogeneity at the cost of imaging speed. Since local shimming around the target can be used in application of local hyperthermia, the binomial pulse was preferred in this study.

## 5.4 Conclusions

A combination of spectral-spatial pulse and echo shifting (TE $>$ TR) in gradient-echo imaging can be used for fast, lipid-suppressed temperature mapping based on the proton resonance frequency. This suggests that the method presented here provides reliable thermometry, even under conditions of unknown tissue fat content. The only disadvantage is the relatively small time penalty due to the incorporation of the spectral-spatial pulse (2 msec per TR period at 1.5 T).

| Voxel | Fat suppression | Signal-to-noise ratio | Variance (theoretical) | Standard deviation (calculated) |
|---|---|---|---|---|
| Focal Point | No | 20.0 | 0.37 | 0.36 |
| Focal Point | Yes | 20.8 | 0.36 | 0.38 |
| Voxel 1 | No | 11.6 | 0.64 | 0.65 |
| Voxel 1 | Yes | 11.8 | 0.63 | 0.68 |
| Voxel 2 | No | 14.7 | 0.51 | 0.50 |
| Voxel 2 | Yes | 16.9 | 0.44 | 0.41 |

*The calculated standard deviation is the standard deviation in the difference between fit and temperature data.

Table 5.2: *Comparison between calculated temperature variance, based on the image signal-to-noise ratio and echo time, and standard deviation in the observed temperature rise for data acquired with a TE of 11.4 msec**

## Acknowledgements

The authors thank Nicolas Grenier, Hervé Trillaud, and Richard Jones (Bordeaux, France) for discussions and help, Peter van Gelderen (NIH, Bethesda, Maryland, USA) for advice, and Scott Chesnick (NIH) for help in constructing the rat holder. J.A.d.Z. was the recipient of a TMR Marie Curie Research Training Grant (European Commission), ERBFMBICT961733.

## References

[1] T. Harth, T. Hahn, M. Rassek, B. Schwabe, H.J. Schwarzmaier, J.S. Lewin, U. Mödder, Determination of laser-induced temperature distributions using echo-shifted TurboFLASH. *Magn. Reson. Med.* **38**, 238-245 (1997)

[2] A.S. Hall, M.V. Prior, J.W. Hand, I.R. Young, R.J. Dickinson, Observation by MR imaging of in vivo temperature changes induced by radio frequency hyperthermia. *J. Comput. Assist. Tomogr.* **14(3)**, 430-436 (1990)

[3] H.J. Schwarzmaier, T. Kahn, Magnetic resonance imaging of microwave induced tissue heating. *Magn. Reson. Med.* **33**, 729-731 (1995)

[4] J.G. Lynn, R.L. Zwemer, A.J. Chick, A.E. Miller, A new method for the generation and use of focused ultrasound in experimental biology. *J. Gen. Physiol.* **26**, 179-193 (1942)

[5] G. ter Haar, D. Sinnett, I. Rivens, High intensity focused ultrasound - a surgical technique for the treatment of discrete liver tumours. *Phys. Med. Biol.* **34(11)**, 1743-1750 (1989)

[6] H.E. Cline, J.F. Schenck, K. Hynynen, R.D. Watkins, S.P. Souza, F.A. Jolesz, MR-Guided focused ultrasound surgery, *J. Comput. Assist. Tomogr.* **16(6)**, 956-965 (1992)

[7] H.E. Cline, J.F. Schenck, R.D. Watkins, K. Hynynen, F.A. Jolesz, Magnetic resonance-guided thermal surgery. *Magn. Reson. Med.* **30**, 98-106 (1993)

[8] C. Damianou, K. Hynynen, Focal spacing and near-field heating during pulsed high temperature ultrasound therapy. *Ultrasound in Med. & Biol.* **19(9)**, 777-787 (1993)

[9] C.T.W. Moonen, D. Madio, A. Olson, D. DesPres, P. van Gelderen, T. Fawcett, N. Holbrook, On the feasibility of MRI guided focused ultrasound for local induction of gene expression, in "Proc., ISMRM, 5th annual meeting, Vancouver, 1997", p. 526

[10] D.P. Madio, P. van Gelderen, D. DesPres, A. Olson, J.A. de Zwart, T.W. Fawcett, N.J. Holbrook, M. Mandel, C.T.W. Moonen, On the feasibility of MRI-guided focused ultrasound for local induction of gene expression. *J. Magn. Res. Imaging* **8**, 101-104 (1998)

[11] D.L. Parker, Application of NMR imaging in hyperthermia: an evaluation of the potential for localized tissue heating and noninvasive temperature monitoring. *IEEE Trans. Biomed. Eng.* **BME-31**, 161-167 (1984)

[12] R.J. Dickinson, A.S. Hall, A.J. Hind, I.R. Young, Measurement of changes in tissue temperature using MR imaging. *J. Comput. Assist. Tomogr.* **10(3)**, 468-472 (1986)

[13] I.R. Young, J.W. Hand, A. Oatridge, M.V. Prior, G.R. Forse, Further observations on the measurement of tissue $T_1$ to monitor temperature in vivo by MRI. *Magn. Reson. Med.* **31**, 342-345 (1994)

[14] H.E. Cline, K. Hynynen, C.J. Hardy, R.D. Watkins, J.F. Schenck, F.A. Jolesz, MR temperature mapping of focused ultrasound surgery. *Magn. Reson. Med.* **31**, 628-636 (1994)

[15] D. Le Bihan, J. Delannoy, R.L. Levin, Temperature mapping with MR imaging of molecular diffusion: application to hyperthermia. *Radiology* **171(3)**, 853 (1989)

[16] Y. Ishihara, A. Calderon, H. Watanabe, K. Mori, K. Okamoto, Y. Suzuki, K. Sato, K. Kuroda, N. Nakagawa, S. Tsutsumi, A precise and fast temperature mapping method using water proton chemical shift, in "Proc., SMRM, 11th annual meeting, Berlin, 1992", p. 4803

[17] J. De Poorter, C. De Wagter, Y. De Deene, C. Thomsen, F. Ståhlberg, E. Achten, Noninvasive MRI thermometry with the proton resonance frequency (PRF) method: in vivo results in human muscle. *Magn. Reson. Med.* **33**, 74-81 (1995)

[18] Y. Ishihara, A. Calderon, H. Watanabe, K. Okamoto, Y. Suzuki, K. Kuroda, Y. Suzuki, A precise and fast temperature mapping using water proton chemical shift. *Magn. Reson. Med.* **34**, 814-823 (1995)

[19] R.D. Peters, R.S. Hinks, R.M. Henkelman, Ex vivo tissue-type invariability in proton-resonance frequency shift MR thermometry, in "Proc., ISMRM, 5th annual meeting, Vancouver, BC, Canada, 1997", p. 1955

[20] J.A. de Zwart, P. van Gelderen, D.J. Kelly, C.T.W. Moonen, Fast magnetic-resonance temperature imaging. *J. Mag. Res. B* **112**, 86-90 (1996)

[21] A.H. Chung, K. Hynynen, V. Colucci, K. Oshio, H.E. Cline, F.A. Jolesz, Optimization of spoiled gradient-echo phase imaging for *in vivo* localization of a focused ultrasound beam. *Magn. Reson. Med.* **36**, 745-752 (1996)

[22] H.E. Cline, K. Hynynen, E. Schneider, C.J. Hardy, S.E. Maier, R.D. Watkins, F.A. Jolesz, Simultaneous magnetic resonance phase and magnitude temperature maps in muscle. *Magn. Reson. Med.* **35**, 309-315 (1996)

[23] K. Kuroda, K. Oshio, A.H. Chung, K. Hynynen, F.A. Jolesz, Temperature Mapping Using the Water Proton Chemical Shift: A Chemical Shift Selective Phase Mapping Method. *Magn. Reson. Med.* **38**, 845-851 (1997)

[24] C.T.W. Moonen, G. Liu, P. van Gelderen, G. Sobering, A fast gradient-recalled MRI technique with increased sensitivity to dynamic susceptibility effects. *Magn. Reson. Med.* **26**, 184-189 (1992)

[25] G. Liu, G. Sobering, A.W. Olson, P. van Gelderen, C.T.W. Moonen, Fast echo-shifted gradient-recalled MRI: combining a short repetition time with variable $T_2^*$ weighting. *Magn. Reson. Med.* **30**, 68-75 (1993)

[26] G. Liu, G. Sobering, J. Duyn, C.T.W. Moonen, A functional MRI technique combining principles of echo-shifting with a train of observations (PRESTO). *Magn. Reson. Med.* **30**, 764-768 (1993)

[27] W.T. Dixon, Simple proton spectroscopic imaging. *Radiology* **153**, 189-194 (1984)

[28] C. Meyer, J. Pauly, A. Macovski, D. Nishimura, Simultaneous spatial and spectral selective excitation. *Magn. Reson. Med.* **15**, 287-304 (1990)

[29] C.J. Baudouin, D.J. Bryant, I.R. Young, Fat suppression in magnetic resonance imaging at low field strength using binomial pulse sequences. *Br. J. Radiol.* **65**, 132-136 (1992)

[30] G.S. Sobering, Y. Shiferaw, P. van Gelderen, C.T.W. Moonen, Quantitative measurement of the phase error for a simple and rapid phase-unwrapping algorithm, in "Proc., ISMRM, 3rd annual meeting, Nice, 1995", p. 661

[31] M. Guéron, P. Plateau, and M. Decorps, Solvent Signal Suppression in NMR, in "Prog. Nucl. Magn. Reson. Spectr.", ed. J.W. Emsley, J. Feeney and L.H. Sutcliffe, Pergamon Press, Oxford, 1991, Vol. 23, p. 135

[32] Y. Zur, M.L. Wood, L.J. Neuringer, Spoiling of transverse magnetization in steady-state sequences. *Magn. Reson. Med.* **21**, 251-263 (1991)

[33] J.H. Duyn, V.S. Mattay, R.H. Sexton, G.S. Sobering, F.A. Barrios, G. Liu, J.A. Frank, D.R. Weinberger, C.T.W. Moonen, 3-dimensional functional imaging of human brain using echo-shifted FLASH MRI. *Magn. Reson. Med.* **32**, 150-155 (1994)

# Chapter 6

# Real-time Correction of Displacement

## Contents

**6.1 Introduction** **77**

**6.2 Materials and methods** **77**

- 6.2.1 Experimental setup and procedures 77
- 6.2.2 Pulse sequences 78
- 6.2.3 On-line data processing 80
- 6.2.4 Temperature calculation 80
- 6.2.5 Navigator-based phase correction 81
- 6.2.6 Detection of displacement 81
- 6.2.7 Correcting spatial reference for thermometry 82
- 6.2.8 FUS power control 83

**6.3 Results and discussion** **83**

- 6.3.1 Exclusion of the heated region from the navigator profile 83
- 6.3.2 Detection of displacement 84
- 6.3.3 Correcting spatial reference for thermometry 84
- 6.3.4 Data processing speed 87
- 6.3.5 Visualization 89

**6.4 Conclusions** **90**

Jacco A. de Zwart, Frédéric C. Vimeux, Jean Palussière, Rares Salomir, Christophe Delalande, Chrit T.W. Moonen
”Real-Time Correction and Visualization of Motion During MR-Controlled FUS Hyperthermia”
*Magnetic Resonance in Medicine* [submitted]

## Abstract

Displacement of tissue during MRI-controlled focused ultrasound (FUS) therapy represents severe potential problems. Errors in calculated temperature may result from motion-related irregular scanning of k-space, leading to image artefacts, and from object displacement, leading to the use of an incorrect spatial temperature reference.

Here, cyclic navigator echoes were incorporated in rapid gradient-echo MRI sequences for temperature mapping based on the proton resonance frequency. Real-time evaluation of navigator information was used in three ways. First, image artifacts were minimized similar to conventional use of navigators. Second, accurate information on displacement, combined with a novel processing method, was employed to correct the reference temperature maps, thereby avoiding persistence of motion-related temperature errors throughout the hyperthermic period. Third, on-line visualization of displacement, together with temperature maps and thermal dose images, was developed, allowing physician intervention at all times.

## 6.1 Introduction

The capability of focused ultrasound (FUS) to non-invasively heat deep-laying soft tissue has been known for over half a century [1], but the lack of a suitable guidance technique prevented widespread medical application. The need for a guidance tool arises from the dependence of the ultrasound characteristics (velocity, attenuation, refraction) on tissue composition and tissue temperature. In addition, heat conduction depends on tissue composition and physiological parameters. MRI has been suggested for FUS-guidance, since it offers both target visualization and thermometry capabilities [2]. Thermal dose for each voxel can be evaluated by integrating the temperature-time trajectory [2, 3]. Temperature mapping by MR has been demonstrated, based on either the apparent diffusion constant D [4], the NMR relaxation time $T_1$ [5, 6] or the water proton resonance frequency (PRF) [7, 8].

The objective of FUS heating in tumor ablation is to obtain complete tumor necrosis without damage to nearby healthy tissue. Since heat will spread over time due to heat conduction, high power FUS heating during short periods of time should be used, leading to steep temperature gradients. However, cavitation should be minimized to maintain a well-defined focal area. The objective of MR-guided FUS in gene therapy is the spatial and temporal control of transgene expression, using genes under control of a heat sensitive promoter [9, 10], requiring accurate temperature control. Both applications are thus expected to benefit from real-time control of FUS by MRI. Recent studies have shown the feasibility of MR-controlled FUS [3, 11, 12], albeit in conditions of no tissue motion.

Displacement of tissue is a severe problem for MRI-controlled FUS for several reasons. First, it leads to image artifacts due to irregular scanning of k-space [13], and thus to errors in temperature images. Second, the displacement of the region of interest leads to errors depending on the particular MR thermometry used. Whereas the $T_1$ and diffusion-based thermometry methods are sensitive to signal intensity changes, the PRF-method is sensitive to phase changes. It is preferred here for thermometry since it does not depend on tissue composition nor on changes in tissue microstructure during therapy [14-16]. Note that the rapid gradient-echo MR methods allow calculation of temperature changes based on the PRF, but not the determination of absolute temperature. The use of correct spatial reference is thus a requirement for reliable temperature mapping. A single tissue displacement during the course of the thermal therapy may lead to temperature errors that persist throughout the hyperthermic period. A third problem of tissue displacement is the fact that the spatial relation between FUS transducer and target is no longer correct and the wrong anatomical region might be heated.

In this work, methods are presented to minimize such motion problems. The basis of the method is the incorporation of cyclic navigators in fast gradient-echo MRI. Real-time processing of navigator data allows accurate detection of displacement and reduction of image artifacts. Furthermore, real-time visualization of displacement, together with temperature maps and thermal dose maps, allows the physician in charge to intervene.

## 6.2 Materials and methods

### 6.2.1 Experimental setup and procedures

Experiments were performed on a Bruker Biospec animal instrument (Bruker, Ettlingen, Germany) with 4.7 T field strength, 500 mm bore and a 120 mm insert gradient set (maximal amplitude: 0.193 T·m$^{-1}$). PRF-based MR temperature maps were acquired using the phase information in gradient echo images [7]. The highest sensitivity for phase changes is achieved at an echo time (TE) equal to the $T_2^*$-value of the tissue [17-19]. In this study a temperature dependence on the image phase of 2.51 rad·s$^{-1}$·T$^{-1}$·K$^{-1}$ (corresponding to a PRF temperature dependence of 0.0094 ppm·K$^{-1}$) was used, as was empirically determined in previous work [19].

The single-element FUS transducer (Specialty Engineering Associates, Soquel, CA, USA) was 38.1 mm in diameter, with a 25.4 mm radius of curvature (focal point at 25.4 mm from transducer surface) and operated at 1.45 MHz. The sinusoidal signal was generated using a Yokogawa FG110 wave generator (Yokogawa, Tokyo, Japan) and amplified using a Kalmus KMP 170F amplifier (Kalmus, Bothell, WA, USA) (58 dB power gain). The wave generator was connected to a serial port of the Silicon Graphics Indy MR control computer (SGI, Mountain View, CA, USA) via a serial/IEEE448 converter plug (IOtech, Cleveland, OH, USA) to allow computer control of the FUS generator output. No interference between FUS and MR imager was observed, allowing FUS application to continue during MR data acquisition.

A plexiglas rat holder was constructed which contained both the FUS transducer and an MR surface coil. A similar setup has been described by Madio et al. [9]. The holder was placed in a plexiglas tube which was partially filled with water. In order to maintain the body temperature of the animal at approximately 35°C the water temperature was regulated using a Haake F3 thermostatic circulator (Haake, Karlsruhe, Germany). A Physitemp ESO-1 thermocouple (Physitemp, Clifton, NJ, USA), connected to a Cole Parmer 91100-50 thermometer (Cole Parmer, Vernon Hills, IL, USA), was used to provide an endorectal reference temperature (accuracy 0.1°C). The ultrasound passes through a 38.1 mm aperture in the platform supporting the animal. The holder was inclined to insure that the rat hind leg was under water while the head was maintained above water. The leg was supported by four 2-0 braided polyester fiber sutures, forming a grid across the aperture. The FUS transducer was positioned so that the focus was approximately 10 mm into the rat thigh. The focal point position of the single-element transducer could not be changed during the hyperthermia procedure.

Male Wistar rats ($n$ = 41, weight 325-550 g) were anesthetized using Halothane (1%) and heated under an approved protocol. Fur was first trimmed and then completely removed using hair remover in order to improve passage of the ultrasound beam into the tissue. After the intervention, rats were injected with 0.5 ml of a solution containing 18 mg/ml of lysin-acetylsalicylate and 2 mg/ml glycine (Vetalgine, Sanofi Santé, Libourne, France) to minimize suffering. All rats were sacrificed 24 hours after treatment.

### 6.2.2 Pulse sequences

Both FLASH (fast low angle shot) and PRESTO (principles of echo-shifting with a train of observations) [21] gradient-echo MR sequences were used during automatic FUS control. In order to combine rapid imaging (implying a short repetition time, TR) with the relatively long echo time ($\sim T_2^*$), necessary to obtain optimal temperature sensitivity [19], the sequences employ the echo shifting principle (TE > TR) [22, 23]. In an echo-shifted sequence, spins excited by the $n^{th}$ RF pulse are dephased by an additional gradient with area $+S$, applied along the three axes. At the end of the $n^{th}$ TR period an additional gradient pulse with area $-2S$ is applied along all axes. The first additional gradient pulse with area $+S$ in the $(n+1)^{th}$ TR period then rephases the spins excited in the $n^{th}$ TR period while dephasing those excited by the $(n+1)^{th}$ RF pulse.

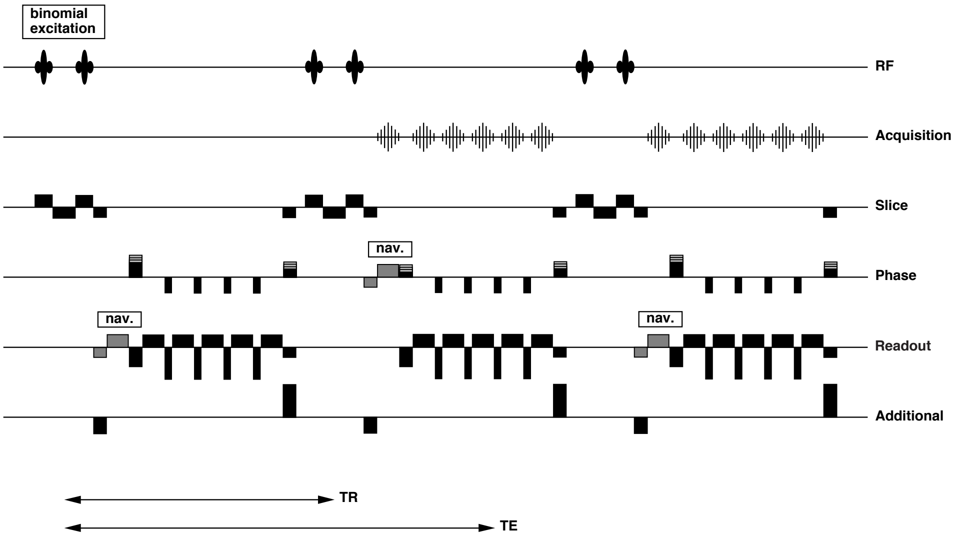

Figure 6.1: *Diagram of the PRESTO sequence. Slice selective binomial excitation is used for lipid suppression [24]. In this example, 5 lines of k-space are acquired per TR period with a single-polarity read-out. Additional gradients along all three axes lead to echo shifting over one TR period. Before the read-out train, a single navigator echo is acquired, cycling between the read and phase direction in successive TR periods.*

For further information about the PRESTO sequence refer to reference [21]. A diagram of the PRESTO sequence used here is given in Figure 6.1. Note that the number of lines acquired per TR period is variable (odd number of lines per TR only).

Lipid signals are a source of significant error in the calculated temperature maps, since their PRFs are not temperature dependent and modify the phase difference obtained in the thermometry experiment [24]. Lipid signals were suppressed using binomial spectral-spatial RF excitation pulses [25, 26], avoiding excitation of lipid signal, as was described previously [24].

To optimize lipid suppression in the target zone, localized shimming was performed using 3D phase information in a selected volume of interest (VOI). To remove transverse coherence, quadratic phase cycling [27] over 8 TR periods was used in all experiments. Both sequences allowed the acquisition of a series of dynamic scans, separated by an optional delay. During this delay, which was an integer multiple of a TR period, no data were acquired, but the slice selective spectral-spatial excitation was not interrupted to preserve a steady state of the spin system, and the phase cycle was maintained. One navigator echo was acquired per TR period, before phase encoding and data acquisition. The navigator echo was alternately acquired along the read and phase-encode directions (cyclic navigator [28], see Figure 6.1), thus allowing in-plane movement detection with a temporal resolution of 2 TR. Figure 6.1 shows a pulse sequence diagram of the PRESTO sequence including cyclic navigators, binomial spectral-spatial excitation and single-polarity read-out with 5 read-outs per TR period.

### 6.2.3 On-line data processing

The control software was written in IDL (RSI, Boulder, CO, USA), running under Digital UNIX 4.0D on a Digital Personal Workstation 500a (Digital Equipment Corporation, Maynard, MA, USA). Before the start of an MR experiment, a region of interest (ROI) was selected to avoid temperature calculation and phase unwrapping in regions with poor signal-to-noise ratio (SNR). Regions to be excluded from navigator comparison (focal point region, water in reservoir) were also determined (see below). A desired temperature evolution was then defined. The on-line processing algorithm was started before the start of the MR experiment. First the experimental parameters (image size; TR; TE; sequence type; number of lines/TR (PRESTO); presence of navigator echoes; number of dynamic scans) were read from the Bruker parameter file, which was present in the data directory. Following completion of the first (reference) data-set, loopwise checks of the data directory were performed to detect the presence of new data. Upon availability of such data, the latest available complete data-set was read. In case MR imaging was faster than data analysis, intermediate images were skipped. A baseline and, in case of PRESTO-data, a phase correction (see reference 19) was calculated using the first data-set and applied to all successive data. Navigator data were analyzed and motion correction was applied, if necessary (see below).

The temperature map was then used to update the FUS amplitude value and to calculate the thermal dose for each voxel according to the empirical equation [29]:

$$\begin{aligned} TD(t) &= \int_0^t r^{(43-T(t))}dt \\ where:\ & r = 0.25 \quad (T < 43°C) \\ & r = 0.50 \quad (T > 43°C) \end{aligned} \tag{6.1}$$

where $TD(t)$ is the thermal dose at time $t$ and $T(t)$ is the temperature evolution in time. The thermal dose can be used to estimate the zone in which the threshold for tissue necrosis is exceeded [3]. The equivalent of 240 minutes at 43°C is used as threshold [29]. Following calculation of the thermal dose, the complete user-interface was updated.

### 6.2.4 Temperature calculation

Phase difference between the current and the reference image in PRF-based MR thermometry has been calculated directly [7, 8, 20], followed by phase unwrapping to correct for possible $2\pi$ discontinuities (this will be referred to as the direct method). Here, an alternative method is proposed, where the phase difference between the latest available image and the preceding image is calculated. This phase difference map is then, after optional phase unwrapping, added to the sum of all previous phase difference maps, resulting in the phase difference image with respect to the reference image (this method will be referred to as the additive method). The resulting phase difference map is of course identical to the map obtained using the direct method:

$$\Delta\phi = \sum_{i=1}^{n}(\phi_i - \phi_{i-1}) = \phi_n - \phi_0 \tag{6.2}$$

where $\phi_i$ is the phase information of a voxel in image $i$ and where $\Delta\phi$ is the final phase difference of that voxel between the last (image $n$) and the reference image (image 0). This method exploits the phase evolution between successive images and therefore has two important advantages:

1) When temperature changes amount to less than $\pi$ radians phase change between two successive images (which is typically the case for fast temperature mapping), phase unwrapping becomes unnecessary, thus accelerating data processing. Phase difference images are calculated from complex data [20]:

$$\Delta\phi = atan\left(\frac{Re_i Im_{i-1} - Re_{i-1} Im_i}{Re_{i-1} Re_i + Im_{i-1} Im_i}\right) \tag{6.3}$$

where $Re_{i-1}$ and $Im_i$ are the real part of image $(i-1)$ and the imaginary part of image $i$, respectively.

2) When temperature-induced phase gradients in the phase difference map between current and reference image exceed $\pi$ radians phase over one voxel, correct phase unwrapping of the phase difference between current and reference image is prone to errors. Changes in phase gradients between successive images are much smaller. Therefore the correct temperature map may still be reconstructed using the additive method. This also implies that even when high temperature changes are expected, the echo time can be optimized for temperature sensitivity ($\mathrm{TE} \sim \mathrm{T}_2^*$).

### 6.2.5 Navigator-based phase correction

Navigator data were zero-filled eight times before FFT to increase the precision of displacement detection (see below). Phase changes in the navigator profiles were used for a zeroth-order phase correction of the k-space lines acquired in that particular TR period to reduce artifacts due to irregular scanning of k-space. The applied correction was similar to navigator correction described in literature [13, 30]. However, the FUS focal region was excluded to avoid errors due to phase changes related to tissue temperature changes. Data points of the navigator profile were selected on the basis of signal intensity (only data where the signal in the reference navigator in the first image exceeded 50% of the maximum signal were accounted for), and data representing the FUS focal region were excluded using the same selection criteria as were applied during displacement detection (see below). Using the selected data, the average phase change with respect to the first navigator profile was determined for the zeroth-order phase correction.

### 6.2.6 Detection of displacement

The first navigator echo in read-out and phase-encode direction was stored for reference purposes. Displacement in read-out and phase-encode direction was calculated from comparison of successive navigator echoes with these reference profiles. In general, navigator and image resolution were identical. Since navigator data were zero-filled eight times, the maximal precision of displacement detection is therefore one-eighth the width of a voxel. The magnitude signal in the obtained profile was subtracted from the magnitude signal in the reference navigator profile acquired along that axis, and the sum of the absolute value of this difference calculated, following exclusion of irrelevant and unwanted parts of the profile (e.g. water bath and heated region).

This subtraction and successive summation were repeated after translation of the navigator profile with respect to the reference profile. The translation with minimal differences is equal to the displacement (with opposite sign) with respect to the starting position.

For each image, the displacement was averaged for read-out as well as phase-encode direction, and then compared to a user-defined threshold. If one or both of the values exceed this threshold, which is defined before the start of the experiment (typically about one-fourth the size of a voxel), a warning is issued (beep) and motion correction is applied automatically. Note that the displacement information may also be used for mechanical or electronic adjustment of the FUS focal point to match the new target location. The FUS setup used for this study did not allow such adjustment.

### 6.2.7 Correcting spatial reference for thermometry

The correction method exploits the additive method of phase difference calculation. If a movement is detected in the $n^{th}$ image, the available sum of phase difference maps at that point is the total phase difference between the $1^{st}$ and the $(n-1)^{th}$ image (see Eq. 6.2). If no movement would have been detected, the phase difference between the $(n-1)^{th}$ and the $n^{th}$ image would have been added to this map to obtain the phase difference between the $1^{st}$ and the $n^{th}$ image. However, since movement occurred during acquisition of the $n^{th}$ image, the calculated phase difference between the $(n-1)^{th}$ and $n^{th}$ image is unreliable and an error would be introduced in all successive temperature maps. The $n^{th}$ image is therefore discarded. However, the measured displacement is used to regrid the available summed phase image (the phase difference between the $1^{st}$ and $(n-1)^{th}$ image) to the new position of the object. Regridding is performed using linear interpolation with a resolution of one-tenth of a voxel size. When the phase difference between the $(n+1)^{th}$ and the $(n+2)^{th}$ image is available, it is added to this regridded summed phase image.

Note that using this method information about temperature changes between the $(n-1)^{th}$ and the $(n+1)^{th}$ image is lost and that noise in the temperature map increases due to the use of a second reference temperature map. If displacements are detected during $m$ images, the noise will increase with $\sqrt{m}$.

In order to test the reliability of both motion detection and correction, various experiments were performed on meat samples of approximately $5 \times 5 \times 2$ cm$^3$, which were attached to a stick and placed in the plexiglas rat holder. In this setup, the meat sample can slide over the top of the table containing the MR surface coil. To prevent motion in the direction perpendicular to the intended sliding direction, two styrofoam strips were fixed on opposite sides of the meat sample, 5 cm apart. A ruler on the opposite end of the stick allowed controlled displacement of the sample during the experiment. The reservoir was filled with water, with the water level 1-2 mm above the table containing the MR surface coil. Data were acquired in a coronal scan plane through the FUS focal point, just above the water level, the sliding motion was performed in the read-out direction. A FLASH sequence was used with the parameters: $80 \times 80$ mm$^2$ field of view (FOV); 3 mm slice thickness (ST); $64 \times 64$ matrix; 20 msec TR; 10 msec TE; 128 dynamic scans; cyclic navigators acquired along the read-out and phase-encode direction; 32 dummy scans. The temporal resolution was 1280 msec. The flip angle was approximately 9° in the focal point region, which is approximately the Ernst-angle for a $T_1$ of 1500 msec and the TR used.

### 6.2.8 FUS power control

Software has been developed in-house to automatically control the applied FUS power based on MR temperature data [3, 12]. Input parameters for the initial version of the control software [3] are: the starting point of the FUS heating relative to the start of the MR experiment; the duration of FUS heating; maximal allowed FUS power; the reference temperature; current focal point temperature; target temperature.

A control mechanism based on a physical model accounting for the local heat deposit and heat loss was used [12]. Before the start of the experiment, a target focal point temperature trajectory is defined, typically a 40-60 sec temperature rise, followed by a constant-temperature plateau of varying duration. The spatial temperature distribution, available on-line from the MR temperature maps, is used to calculate the FUS deposit required to achieve the target temperature, based on the bioheat equation [31]:

$$\alpha_2(\vec{r},T)P(\vec{r},t) = -\alpha_1(\vec{r},T)\nabla^2 T(\vec{r},t) + \rho(\vec{r})c(\vec{r})\frac{\partial T(\vec{r},t)}{\partial t} \tag{6.4}$$

where $P(\vec{r},t)$ is the spatial distribution of the applied FUS, which is the parameter modified by the control software. $\alpha_2$ is the FUS absorption coefficient of the tissue. $c$, $\rho$ and $\alpha_1$ are the specific heat, density and thermal conductivity of the tissue, respectively. $T$ is the temperature rise above body temperature. Since rapid heating is assumed, perfusion is neglected.

## 6.3 Results and discussion

### 6.3.1 Exclusion of the heated region from the navigator profile

An immobilized meat sample was heated 20°C above initial temperature for 120 sec under automatic FUS control, starting 20 sec after the start of the MR experiment. Figure 6.2 shows a reference navigator profile for the read direction (the first navigator profile in the first dataset, broken line, shifted 500 a.u. upward for figure clarity) and a magnitude navigator profile that was acquired 40 sec after the start of the MR experiment (at the moment that the target temperature rise of 20°C was reached, solid line). The signal drop around sample number 33 is the result of large, local phase changes that are caused by the 20°C temperature increase (4.7 radians phase change is expected with a 20 msec TE at 4.7 T for 20°C temperature change). Since each navigator echo is a projection, large phase changes in the direction perpendicular to its read-out lead to a signal drop due to dispersion of phase. Errors in navigator comparison might arise from this signal drop. In all experiments, the hyperthermia target zone was therefore systematically excluded from navigator analysis. Generally, in vivo experiments were carried out using a transverse scan plane, through the centre of the transducer. Therefore, water in the reservoir containing the rat-holder was also excluded from analysis of navigator profiles acquired in the phase-encode direction. Typically, a zone the size of 5 voxels on each side of the FUS focal point was excluded from navigator analysis.

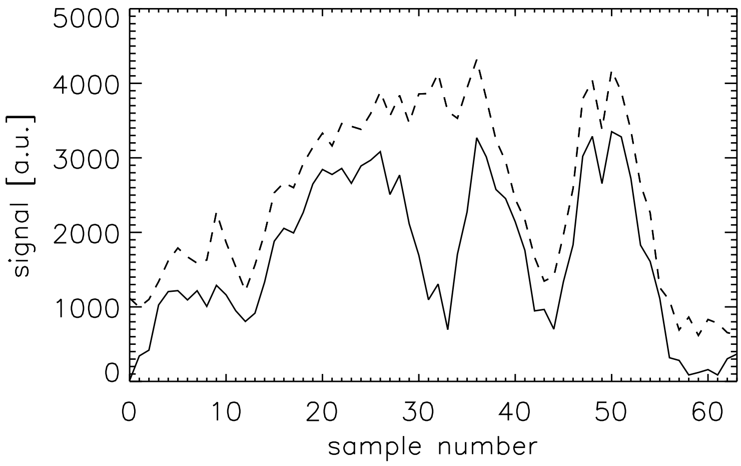

Figure 6.2: *Reference navigator profile (broken line) and navigator profile after a 20°C temperature rise in the focal point (solid line). The signal drop in the center (around sample number 33) is caused by large, local, temperature induced phase changes. Since the navigator echo is a projection, phase dispersion perpendicular to the acquisition direction cause a drop in the signal. Note that the reference profile is shifted 500 a.u. upward to improve figure clarity.*

### 6.3.2 Detection of displacement

Fig. 6.3 shows the results from navigator analysis during stepwise displacement of a meat sample while constant-power FUS heating was applied. The figure shows the calculated displacement in both the read-out direction (the direction in which the sample was moved) and the phase-encode direction. FUS heating was applied during a 120-sec period, starting 20 sec into the experiment. The sample was moved over a distance of approximately 4.5 mm in 5 steps, and thereafter replaced at approximately its original position. After each step, the sample was left at its new position for 5 to 10 sec before being moved again. The standard deviation in the calculated displacement, calculated over the first 32 images, before the sample was moved, was 0.014 mm in the read-out and 0.009 mm in the phase-encode direction. Similar experiments, in which the sample was not moved, indicated that the final temperature rise achieved using this heating cycle was approximately 10°C (results not shown). The results demonstrate the accuracy of displacement detection using cyclic navigator information.

In a series of experiments conducted on rat thigh in vivo ($n$ = 12), the average standard deviation in the calculated displacement was 0.10 mm for the read-out direction and 0.08 mm for the phase-encode direction.

### 6.3.3 Correcting spatial reference for thermometry

The efficacy of the proposed movement correction technique is demonstrated in Fig. 6.4. A meat sample was moved, first approximately 2.5 mm (at the time of acquisition of image 30) and then to a position about 4.5 mm from the starting position (when image 60 was acquired). At the time of acquisition of image 91, the sample was returned to approximately its original position. Fig. 6.4a shows the displacements of the meat sample in both the read-out and phase-

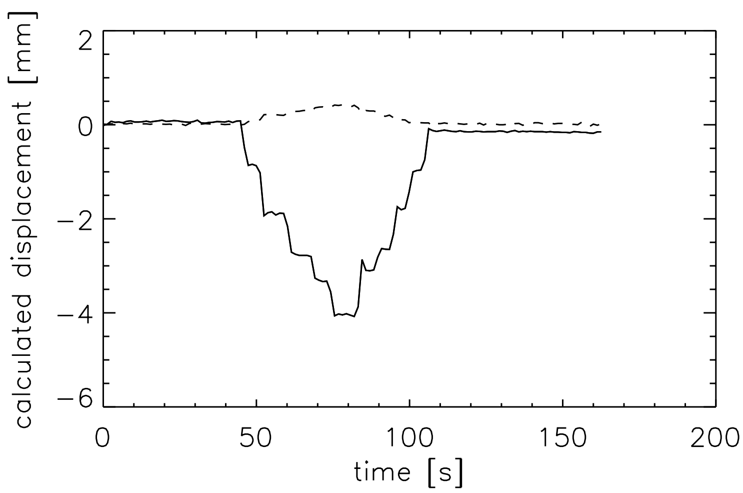

Figure 6.3: *Displacements measured when a meat sample was moved approximately 4.5 mm in five steps and thereafter returned to its original position. During the experiment, FUS heating was applied for 120-sec, starting 20 sec after the start of data acquisition. The solid line shows the displacement in the read direction, the direction in which the sample was moved. The displacement in the phase-encode direction is shown as a broken line. The standard deviation in the calculated displacement, calculated over the first 32 images (before the sample was moved) was 0.014 mm in the read-out and 0.009 mm in the phase-encode direction.*

encode direction, as calculated from the navigator data. The standard deviation in the navigator data, calculated over the first 29 images (before the first movement was applied), was 0.022 mm in the read-out and 0.018 mm in the phase-encode direction. In Fig. 6.4b the calculated temperature as a function of time in a voxel (fixed in real space, relative to magnet, irrespective of sample position) is shown. The data were analyzed both with and without application of the proposed correction method. When correction of spatial reference is not applied, large apparent temperature changes are calculated due to the use of incorrect spatial reference phase, even though the sample was not heated. When correction of spatial reference is applied using a threshold for target displacement of 0.2 mm, the calculated temperature is insensitive to the displacements. Note that the amplitude and sign of such apparent temperature changes depend on local field homogeneity. The data of Fig. 6.4b represent a randomly chosen voxel within the meat sample. Other voxels give qualitatively similar results.

The threshold-value used for automatic correction following target displacement depends on both the accuracy of the displacement detection and field homogeneity. When important local field inhomogeneities exist, the error in calculated temperature for a given displacement will be more important. Field homogeneity and spin density changes can be evaluated beforehand using high resolution magnitude and phase images. Typically, a threshold equivalent to approximately three times the standard deviation of the noise in displacement detection was used.

When a movement is detected during the acquisition of the $n^{th}$ image, information about the phase changes between the acquisition of the $(n-1)^{th}$ and the $(n+1)^{th}$ is lost using the method proposed here. It is possible to restore the lost information by regridding the complex $(n-1)^{th}$ data set to the new sample position and to calculate the phase difference map between

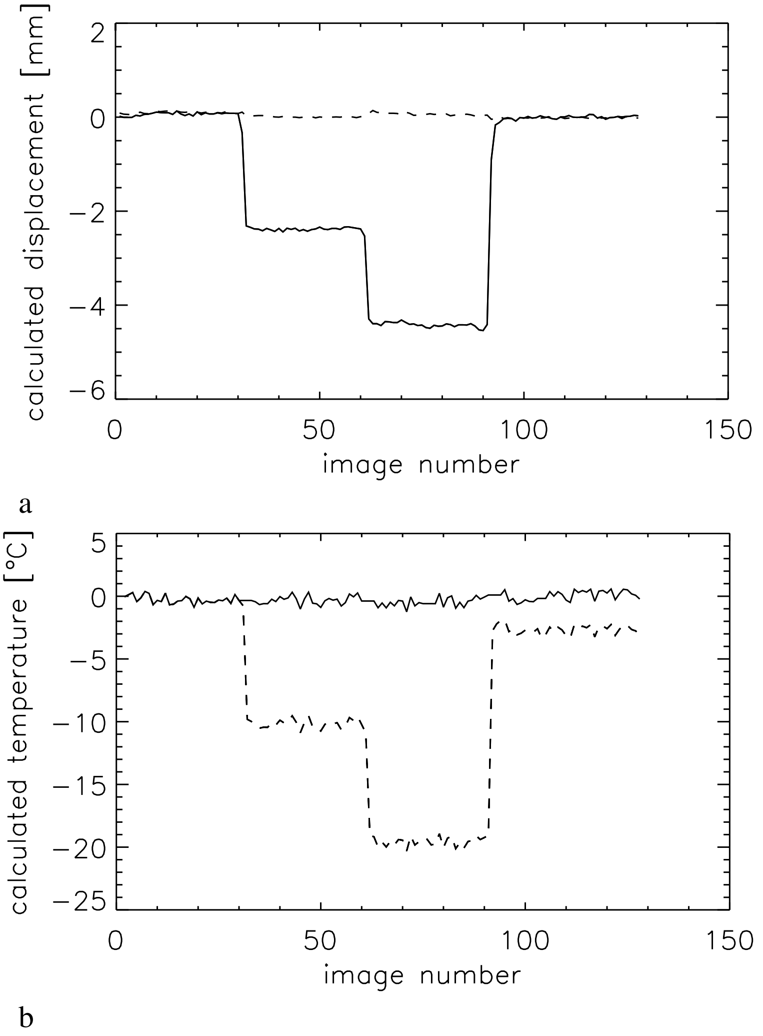

Figure 6.4: *a) Displacement measured using navigator profiles in read-out (solid line) and phase-encode (broken line) during MR thermometry of a moving meat sample. b) Apparent temperature changes calculated on the basis of MR data acquired during this experiment, both without (broken line) and with (solid line) on-line automatic navigator correction. No FUS heating was applied, the threshold for navigator correction was 0.2 mm, both the image and navigator resolution were 1.25 mm.*

| Machine | CPU | Clock speed | Operating system | Test 1[b] | Test 2[c] |
|---|---|---|---|---|---|
| SGI Indy[d] | MIPS R4000 | 100 MHz | IRIX 5.3 | 519 | 1080 |
| SGI O2 | MIPS R5000 | 180 MHz | IRIX 6.3 | 302 | 489 |
| Dell OptiPlex GX1 | Intel Pentium II | 350 MHz | Linux 2.2.5 | 110[e] | 175[e] |
| PC | AMD Athlon | 600 MHz | Linux 2.2.12 | 68[e] | 102[e] |
| Digital PW 500a | Dec Alpha 20164 | 500 MHz | Digital UNIX 4.0D | 59[e] | 133[e] |

[a] Tests performed using PRESTO-data: 64 × 63 matrix; 3 k-space lines acquired per TR period; 384 dynamics; cyclic navigator

[b] Standard data analysis without analysis of navigator data

[c] Standard data analysis including navigator analysis

[d] MR system computer

[e] Including byte swap of the data

Table 6.1: *Data processing time per image (in msec) of the control software*[a]

the regridded $(n-1)^{th}$ image and the $(n+1)^{th}$ image. The resulting phase difference map may then be added to the regridded subtotal phase difference map. However, the obtained phase difference between the regridded $(n-1)^{th}$ data-set and the $(n+1)^{th}$ data-set was found to be error prone (results not shown). These errors are probably due to inter- and intra-voxel spin density and field homogeneity distribution. This additional correction was therefore not further used. Note that the regridding algorithm used here, linear interpolation, is rather simple because of the speed requirements for real-time applications.

Note that a movement correction method based on the comparison of signal in acquired navigator profiles is based on the assumption that the shape of the profile has not changed after displacement. Such a method therefore depends on the sensitivity profile of the RF-coil and field inhomogeneities that are not caused by the object. In this study, correction for such effects proved unnecessary.

### 6.3.4 Data processing speed

The typical processing time per image was less than 200 msec, including FUS control software and update of the complete user interface. A separate IDL routine, applying the calculated FUS power, was running on the Silicon Graphics MR system computer to which the FUS signal generator is connected. The workstations communicated over a standard TCP/IP network. This setup was chosen to accelerate data processing as can be seen from Table 1, where the average data processing time on 3 UNIX workstations and 2 PCs operating under Linux is given. These data are obtained by off-line analysis of a PRESTO data-set (64 × 63 matrix; 3 lines/TR; 384 dynamics; cyclic navigators). A copy of the data was stored on a local hard-disk and analyzed image by image with the same software used for on-line analysis during the MR experiments. The total duration of the main loop was measured using a standard IDL timing function and divided by the number of dynamic scans minus one (since the first time the loop is entered two images are read to obtain a reference image). The experiment was performed twice, once with and once without analysis of the navigator data, demonstrating that navigator analysis currently accounts for approximately 50% of the processing time. Note that these data contain only 21 navigator echoes per image. The time penalty of navigator analysis when using FLASH-data, typically containing 64 navigator echoes, is therefore higher.

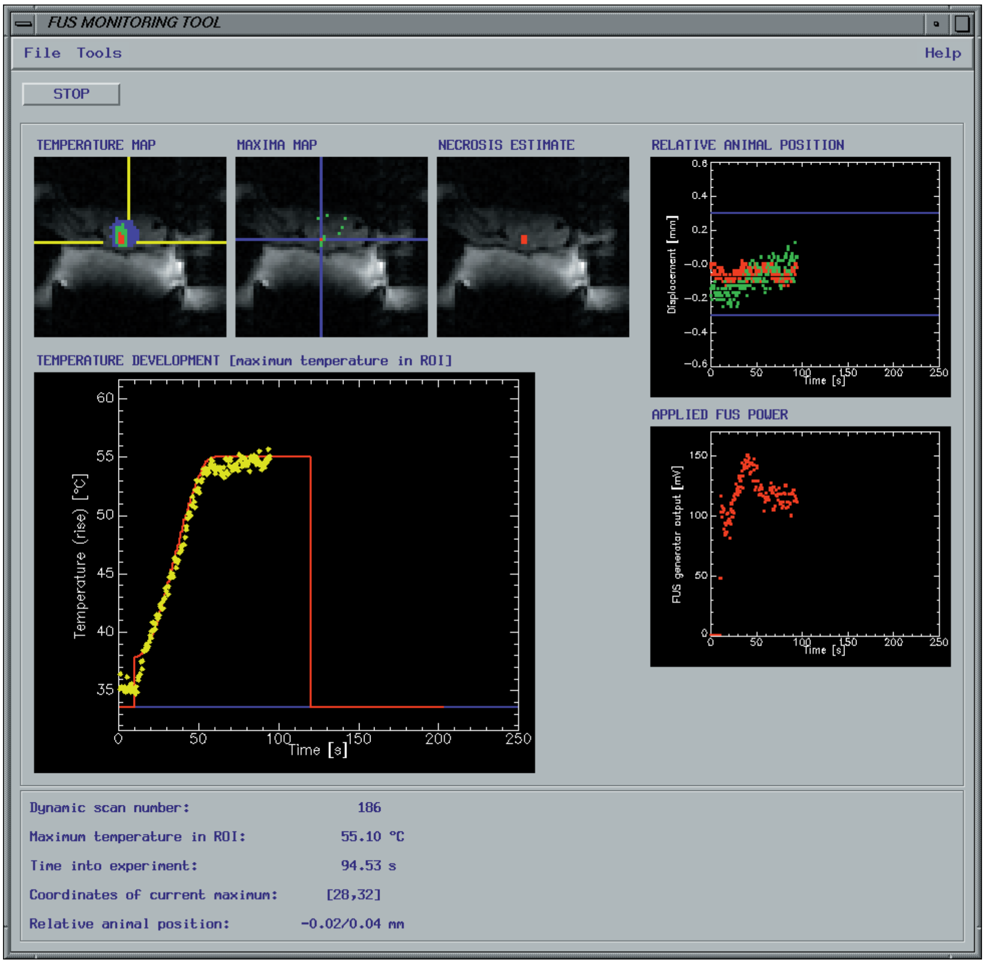
FUS MONITORING TOOL
File
Tools
Help
STOP
TEMPERATURE MAP
MAXIMA MAP
NECROSIS ESTIMATE
RELATIVE ANIMAL POSITION
0.6
0.4
0.2
-0.0
-0.2
-0.4
-0.6
Displacement [mm]
0
50
100
150
200
250
Time [s]
TEMPERATURE DEVELOPMENT [maximum temperature in ROI]
60
55
50
45
40
35
Temperature (rise) [°C]
0
50
100
150
200
250
Time [s]
APPLIED FUS POWER
150
100
50
0
FUS generator output [mV]
0
50
100
150
200
250
Time [s]

Dynamic scan number: 186

Maximum temperature in ROI: 55.10 °C

Time into experiment: 94.53 s

Coordinates of current maximum: [28,32]

Relative animal position: -0.02/0.04 mm

Figure 6.5: *User interface of the automatic FUS heating tool. During MR thermometry the interface is updated in real-time to give the user accurate information about the state of the intervention. Top-left: Color coded temperature map. Top-center: Focal point location and focal point history. Top-right: Necrosis estimate based on applied thermal dose. Main plot: Focal point temperature as a function of time. Top-right plot: Displacement calculated from cyclic navigators. Bottom-right plot: Output of FUS generator under automatic control. See text for more details.*

These results indicate that, for 2D data, real-time data handling on a low end UNIX- or Linux-machine is feasible. Multi-slice or 3D temperature imaging might require a faster computer to allow sub-second processing. Please note that the specific diffusion time of heat in tissue is in the order of 10 sec [12]. The methods proposed here allow control of the heating procedure with an update of at least a factor of 10 faster. Therefore, the term real-time processing appears justified despite the rather poor general definition of “real-time”.

### 6.3.5 Visualization

A control window is shown in Fig. 6.5. Similar to a previously reported approach [32], the window is updated immediately after processing of each image, informing the user on-line about the state of the hyperthermia procedure. The goal of the particular experiment, performed on rat thigh muscle in vivo, was to heat tissue locally at 55°C for 60 sec, following a 50-sec temperature rise (with shape equal to half the cycle of a sine wave).

The top-right graph shows the outcome of navigator echo analysis, where horizontal blue lines indicate the threshold for target displacement. When the detected displacement exceeds this limit, the user is warned with a beep and movement correction is applied.

The bottom-right graph shows the output of the wave generator (in mV) throughout the hyperthermia procedure. Note that the electrical power, sent to the FUS transducer, increases with the square of the generator output in mV. In the top-left corner, a color coded temperature map is shown, superimposed on the latest available $T_2^*$-weighted image. The threshold for each of the three color levels is set by the user before the start of the experiment. The yellow lines indicate the regions taken into account in navigator analysis, typically the area around the FUS focal point and the water in the reservoir are excluded. The FUS transducer is located in the lower part of the $T_2^*$-weighted image. The interface between rat thigh (in top of the image) and the water in the reservoir water can be seen as a low-intensity line just below the heated region. The plexiglas table, which supports the animal and contains the MR surface coil, is represented by the two low-intensity regions on the left and right side of the image.

The top-center image indicates the current location of the focal point (blue cross) and allows on-line evaluation of displacement of focal point due to modified ultrasound characteristics upon local tissue heating. The focal point is defined as the hottest voxel in a beforehand selected region of interest. Green and red points indicate the voxels that have been labeled as focal point after FUS application was started, where the red voxel indicates the voxel that was most frequently identified as the focal point. The top-right image shows an estimate of tissue necrosis. This estimate is based on the thermal dose that is calculated using the MR temperature maps and Eq. 6.1. Both focal point history map and tissue necrosis estimate are translated automatically when displacement correction is applied.

The main graph (bottom-left) shows the maximum temperature in the ROI as a function of time. The horizontal blue line indicates the reference temperature, the red curve shows the desired focal point temperature profile (target profile). Note that the data shown before start of the FUS heating reflect the maxima of the noise in temperature in the ROI of the respective image and thus indicate an apparent starting temperature slightly above the body temperature. This results from the fact that, before heating occurs, the hottest voxel is determined by the maximum positive noise in the ROI.

In the top left corner, a stop button is present which allows instant interruption of both FUS heating and MR thermometry.

The accuracy of MR thermometry experiments on in vivo rat thigh, determined prior to hyperthermia, was 0.48°C (average of standard deviations, obtained for each of 7 rats). Upon heating to a constant temperature, a precision in the focal point of 0.72°C was reached. The results show that accurate temperature control is feasible, together with real-time evaluation of displacement and correction of temperature maps.

## 6.4 Conclusions

The results demonstrate the efficacy of real-time motion detection and correction, based on cyclic navigator echoes, for PRF-based MR temperature imaging throughout the hyperthermic procedure. The methods provide reduction of motion artifacts, and correction of the spatial reference for temperature calculation following tissue displacements. In addition, the displacement of tissue, together with temperature and thermal dose maps, are used for real-time visualization, allowing intervention at any time.

## Acknowledgements

The authors thank Bruno Quesson, Nicolas Grenier, Paul Canioni and Hervé Trillaud (RMSB, Victor Segalen University, Bordeaux, France), Jean Pergrale and Pierre Lelong (Laboratoires d'Electronique Philips, Limeil-Brévannes, France), Erik Dumont and Joop van Vaals (Philips Medical Systems) for helpful discussions.

## References

[1] J.G. Lynn, R.L. Zwemer, A.J. Chick, A.E. Miller, A new method for the generation and use of focused ultrasound in experimental biology. *J. Gen. Physiol.* **26**, 179-193 (1942)

[2] H.E. Cline, J.F. Schenck, K. Hynynen, R.D. Watkins, S.P. Souza, F.A. Jolesz, MR-guided focused ultrasound surgery. *J. Comput. Assist. Tomogr.* **16**, 956-965 (1992)

[3] F.C. Vimeux, J.A. de Zwart, J. Palussière, R. Fawaz, C. Delalande, P. Canioni, N. Grenier, C.T.W. Moonen, Real-time control of focused ultrasound heating based on rapid MR thermometry. *Invest. Radiol.* **34(3)**, 190-193 (1999)

[4] D. Le Bihan, J. Delannoy, R.L. Levin, Temperature mapping with MR imaging of molecular diffusion: application to hyperthermia. *Radiology* **171(3)**, 853 (1989)

[5] D.L. Parker, Application of NMR imaging in hyperthermia: an evaluation of the potential for localized tissue heating and noninvasive temperature monitoring. *IEEE Trans. Biomed. Eng.* **31**, 161-167 (1984)

[6] R.J. Dickinson, A.S. Hall, A.J. Hind, I.R. Young, Measurement of changes in tissue temperature using MR imaging. *J. Comput. Assist. Tomogr.* **10(3)**, 468-472 (1986)

[7] Y. Ishihara, A. Calderon, H.Watanabe, K. Mori, K. Okamoto, Y. Suzuki, K. Sato, K. Kuroda, N. Nakagawa, S. Tsutsumi, A precise and fast temperature mapping method using water proton chemical shift, in "Proc., SMRM, 11th annual meeting, Berlin, 1992", p. 4803

[8] J. De Poorter, C. De Wagter, Y. De Deene, C. Thomsen, F. Ståhlberg, E. Achten, Noninvasive MRI thermometry with the proton resonance frequency (PRF) method: in vivo results in human muscle. *Magn. Res. Med.* **33**, 74-81 (1995)

[9] D.P. Madio, P. van Gelderen, D. DesPres, A. Olson, J.A. de Zwart, T.W. Fawcett, N.J. Holbrook, M. Mandel, C.T.W. Moonen, On the feasibility of MRI-guided focused ultrasound for local induction of gene expression. *J. Magn. Res. Imaging* **8**, 101-104 (1998)

[10] C. Moonen, A. Vekris, P. Voisin, J. de Zwart, C. Maurange, F. Vimeux, P. Canioni, Spatial and temporal control of transgene expression with heat-sensitive promoter and MRI guided focused ultrasound, in "Proc., ISMRM, 7th annual meeting, Philadelphia, 1999", p. 402

[11] K. Hynynen, N. McDannold, F. Jolesz, The feasibility of MRI control of ultrasound surgery of large tumors, in "Proc., ISMRM, 7th annual meeting, Philadelphia, PA, USA, 1999", p. 1943

[12] R. Salomir, F.C. Vimeux, J.A. de Zwart, N. Grenier, C.T.W. Moonen, Hyperthermia by MR-guided focused ultrasound: accurate temperature control based on fast MRI and a physical model of local energy deposition and heat conduction. *Magn. Reson. Med.* **43**, 342-347 (2000) labelINref31

[13] R.L. Ehman, J.P. Felmee, Adaptive technique for high-definition MR imaging of moving structures. *Radiology* **173**, 255-263 (1989)

[14] Y. Ishihara, A. Calderon, H. Watanabe, K. Okamoto, Y. Suzuki, K. Kuroda, Y. Suzuki, A precise and fast temperature mapping using water proton chemical shift. *Magn. Reson. Med.* **34**, 814-823 (1995)

[15] R.D. Peters, R.S. Hinks, R.M. Henkelman, Ex vivo tissue-type invariability in proton-resonance frequency shift MR thermometry, in "Proc., ISMRM, 5th annual meeting, Vancouver, BC, Canada, 1997", p. 1955

[16] S.J. Graham, M.J. Bronskill, R.M. Henkelman, Time and temperature dependence of MR parameters during thermal coagulation of ex vivo rabbit muscle. *Magn. Reson. Med.* **39**, 198-203 (1998)

[17] K. Kuroda, K. Oshio, A.H. Chung, K. Hynynen, F.A. Jolesz, Temperature Mapping Using the Water Proton Chemical Shift: A Chemical Shift Selective Phase Mapping Method. *Magn. Reson. Med.* **38**, 845-851 (1997)

[18] T. Harth, T. Hahn, M. Rassek, B. Schwabe, H.J. Schwarzmaier, J.S. Lewin, U. Mödder, Determination of laser-induced temperature distributions using echo-shifted TurboFLASH. *Magn. Reson. Med.* **38**, 238-245 (1997)

[19] J.A. de Zwart, P. van Gelderen, D.J. Kelly, C.T.W. Moonen, Fast magnetic-resonance temperature imaging. *J. Mag. Res. B* **112**, 86-90 (1996)

[20] A.H. Chung, K. Hynynen, V. Colucci, K. Oshio, H.E. Cline, F.A. Jolesz, Optimization of spoiled gradient-echo phase imaging for in vivo localization of a focused ultrasound beam. *Magn. Reson. Med.* **36**, 745-752 (1996)

[21] G. Liu, G. Sobering, J. Duyn, C.T.W. Moonen, A functional MRI technique combining principles of echo-shifting with a train of observations (PRESTO). *Magn. Reson. Med.* **30**, 764-768 (1993)

[22] C.T.W. Moonen, G. Liu, P. van Gelderen, G. Sobering, A fast gradient-recalled MRI technique with increased sensitivity to dynamic susceptibility effects. *Magn. Reson. Med.* **26**, 184-189 (1992)

[23] G. Liu, G. Sobering, A.W. Olson, P. van Gelderen, C.T.W. Moonen, Fast echo-shifted gradient-recalled MRI: combining a short repetition time with variable $T_2^*$ weighting. *Magn. Reson. Med.* **30**, 68-75 (1993)

[24] J.A. de Zwart, F.C. Vimeux, C. Delalande, P. Canioni, C.T.W. Moonen, Fast lipid suppressed MR temperature mapping with echo-shifted gradient echo imaging and spectral-spatial excitation. *Magn. Reson. Med.* **42**, 53-59 (1999)

[25] C. Meyer, J. Pauly, A. Macovski, D. Nishimura, Simultaneous spatial and spectral selective excitation. *Magn. Reson. Med.* **15**, 287-304 (1990)

[26] M. Guéron, P. Plateau, and M. Decorps, Solvent Signal Suppression in NMR, in "Prog. Nucl. Magn. Reson. Spectr.", ed. J.W. Emsley, J. Feeney and L.H. Sutcliffe, Pergamon Press, Oxford, 1991, Vol. 23, p. 135.

[27] Y. Zur, M.L. Wood, L.J. Neuringer, Spoiling of transverse magnetization in steady-state sequences. *Magn. Reson. Med.* **21**, 251-263 (1991)

[28] J.W.C. van der Veen, P. van Gelderen, D.R. Weinberger, C.T.W. Moonen, Characterization of brain motion with a 3D navigator and reduction of motion artifacts in PRESTO, in "Proc., ISMRM, 5th annual meeting, Vancouver, BC, Canada, 1997", p. 466

[29] S.A. Sapareto, W.C. Dewey, Thermal dose determination in cancer therapy. *Int. J. Radiation Oncology Biol. Phys.* **10**, 787-800 (1984)

[30] N.F. Ramsey, J.S. van der Brink, A.M.C. van Muiswinkel, P.J.M. Folkers, C.T.W. Moonen, J.M. Jansma, R.S. Kahn, Phase navigator correction in 3D fMRI improves detection of brain activation: quantitative assessment with a graded motor activation procedure. *Neuroimage* **8**, 240-248 (1998)

[31] H.H. Pennes, Analysis of tissue and arterial blood temperatures in the resting human forearm. *J. Appl. Physiol.* **1**, 93-122 (1948)

[32] K.C. Patel, J.L. Duerk, Q. Zhang, Y.C. Chung, M. Williams, K. Kaczynski, M. Wendt, J.S. Lewin, Methods for providing probe position and temperature information on MR images during interventional procedures. *IEEE Trans. Med. Imag.* **17**, 794-802 (1998)

# Part III

# Methodology: Controlling the Hyperthermia Procedure

# Chapter 7

# FUS heating under MR Control

## Contents

**7.1 Introduction** **96**

**7.2 Materials and methods** **96**

7.2.1 Manual FUS control 96

7.2.2 Automatic FUS control 97

7.2.3 Tissue necrosis estimation based on MR thermometry 97

**7.3 Results** **97**

7.3.1 FUS control using MR thermometry 97

7.3.2 Estimation of tissue necrosis 100

**7.4 Discussion and conclusion** **101**

Adapted from:

Frédéric C. Vimeux, Jacco A. de Zwart, Jean Palussière, Rabia Fawaz, Christophe Delalande, Paul Canioni, Nicolas Grenier, Chrit T.W. Moonen

”Real-Time Control of Focused Ultrasound Heating Based on Rapid MR Thermometry”

*Investigative Radiology* **34**, 190-193 (1999)

## 7.1 Introduction

The use of MR thermometry for the evaluation of temperature evolution during and after FUS heating has been described previously [1-5]. The novelty of the work described here is the use of temperature information to control the hyperthermia procedure. This necessitates rapid MR thermometry, together with on-line data processing and an interface between the MR system computer and the FUS wave generator. In addition, the on-line available information about the spatial distribution of temperature is used to update, on-line, a map of the degree of tissue necrosis for each voxel, which is subsequently used to indicate treatment progress. For MR-controlled tissue ablation, mapping of tissue necrosis appears the correct parameter to determine success of treatment.

## 7.2 Materials and methods

All experiments described in this chapter were performed on the 4.7 T Bruker Biospec animal instrument with a 120 mm diameter shielded gradient insert.

Data were processed on-line using routines written in IDL. Data analysis software was running on the Bruker MR system computer, a 100 MHz Silicon Graphics Indy workstation. Temperature maps were based on the temperature dependence of the water proton resonance frequency [6-9], the pulse sequences used have been described in chapter 4.

FUS heating experiments were performed using a 38.1 mm diameter FUS transducer with a fixed focal depth of 25.4 mm, operating at 1.45 MHz. Sinusoidal signal to drive the FUS transducer was generated using a Yokogawa FG-110 function generator, the signal was amplified using a Kalmus 170/KMP amplifier. The transducer was placed in a plexiglas rat holder which contains a transmit/receive MR surface coil, a setup which is described in more detail in the chapters 5 and 11. The distance between the table supporting the animal and the table containing the FUS transducer could be adjusted so the FUS focal point depth into the tissue could be set during the preparation-phase of the experiment.

### 7.2.1 Manual FUS control

Initially, FUS heating was controlled manually on the basis of the calculated focal point temperature, which was displayed on the screen each time a new image had been analyzed. Before the start of the actual hyperthermia procedure, the location of the FUS focal point was determined using a low-power FUS sonication. MR temperature maps, acquired during this pilot experiment, were analyzed off-line. The center of the hottest voxel was taken as the FUS focal point. During subsequent high-power FUS sonication, data were analyzed on-line, based on the input parameters: echo time (TE); reference temperature; focal point coordinates; phase difference between latest and reference (first) image. The displayed focal point temperature, the temperature in the focal point determined during the pilot experiment, was used to control the FUS power manually by switching the FUS amplifier on or off if the actual temperature was below or above the target temperature, respectively. These experiments were performed on the thigh muscle of a sacrificed rat. MRI parameters for both the low- and high-power FUS experiment were: $64 \times 64$ matrix; $80 \times 80$ mm$^2$ field-of-view; 4 mm slice thickness; 10 msec TE; 20 msec repetition time (TR); 375 acquired images; and 1.28 sec acquisition time per image.

### 7.2.2 Automatic FUS control

An automatic FUS control system was developed using a serial-to-IEEE488 converter plug (IOtech, Cleveland, OH). The converter plug linked the wave generator to the serial port of the MR system control computer. The MR thermometry data were analyzed on-line using a modified version of the software described above, where an additional subroutine was used to modify the output voltage of the wave generator immediately after the analysis of each image. The focal point was localized using a pilot experiment, as described above. Thereafter, the parameters for the feedback control software were entered: focal point coordinates; starting time of the FUS heating procedure (relative to the start of the MR data acquisition); duration of FUS heating; desired temperature; reference (starting) temperature.

The speed of the control system was limited by image reconstruction, which took approximately 1 sec in the described setup. Initial experiments were performed on turkey meat and the thigh muscle of a sacrificed rat. MRI parameters of the gradient echo thermometry sequence were as follows: matrix 64 × 64; field-of-view 80 mm × 80 mm; slice thickness 5 mm; TE 12 msec; TR 80 msec; total number of images 370; and acquisition time per image 5.12 sec. A limitation of the available pulse program memory of the MRI-system prevented the use of a larger number of images, and therefore a shorter time per image.

### 7.2.3 Tissue necrosis estimation based on MR thermometry

Tissue ablation in the thigh muscle of male Wistar rats ($n$ = 6) with a mass of 500 ± 50 g was studied under an approved laboratory animal protocol. Throughout the experiment, the body temperature of the animal was measured using a copper-constantan thermocouple and kept at approximately 35°C. The fur on one of the thighs was first trimmed and then completely removed using hair remover to obtain good contact between skin and water, thus allowing propagation of the ultrasound waves into the rat thigh. Anesthesia was initiated with pentobarbital (intramuscular injection of 0.8 ml/kg). While in the magnet, the animal was kept under anesthesia using halothane (1%). Just after the sonication, 0.5 ml of Vetalgine (acetylsalicylic acid, Sanofi Santé Nutrition Animale, Libourne, France) was injected to minimize possible suffering. The animal was killed 12 hours after the sonication. The heated leg was dissected, fixed in 10% formalin, and sectioned for histologic examination. Sections were stained with hematoxylin, eosin, and saffron and examined.

The size of the tissue necrosis, found in histology, was compared with the necrosis volume predicted on the basis of the thermal dose, calculated from on-line acquired temperature data using Eq. 1.1 [10].

The MRI parameters of the gradient echo thermometry sequence used in these experiments were: 64 × 64 matrix; 64 mm × 64 mm$^2$ field-of-view; 5 mm slice thickness; 12 msec TE; 15 msec TR; and 360 dynamic scans.

## 7.3 Results

### 7.3.1 FUS control using MR thermometry

Figure 7.1 shows the temperature evolution at the focal point and at two locations at respectively 10 and 20 mm from the focal point during FUS heating under manual control. The data

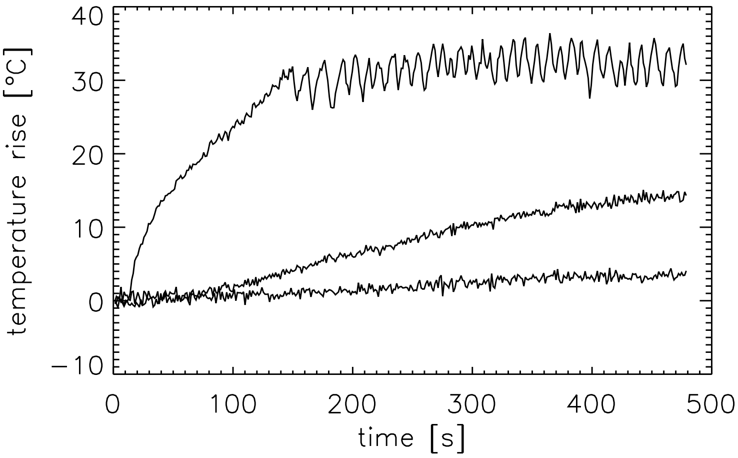

Figure 7.1: *An example of manual temperature control of FUS heating in the thigh of a dead rat using 17.5 W electrical power ultrasound. The top curve shows the evolution of focal point temperature. The target temperature was 30°C above the starting value. The middle and bottom lines show the temperature evolution in a voxel at 10 mm and 20 mm from the focal point, respectively.*

demonstrate that temperature visualization in real time allowed the focal point temperature to be maintained at the desired level. A temperature rise of 30°C was chosen to simulate application to tissue ablation, whereas a 6°C temperature rise was chosen to simulate application to gene therapy or local drug release (result not shown). It was possible to maintain the temperature at 30°C with a precision of ± 4°C (see Fig. 7.1) and at 6°C with a precision of ± 1°C. The precision of the MR thermometry itself was 0.2 to 0.5°C. Temperature variation (see Fig. 7.1) in the focal point is thus greater than the noise in the temperature measurement, which is due to the binary on/off FUS switching. This can been seen from the fluctuation of measured temperature away from the focal point (see Fig. 7.1, middle and bottom curve), which is due to noise in the temperature measurement only, indicating that heating of these voxels is caused by heat conduction and not by direct FUS heating.

Automatic control of FUS during hyperthermia, based on on-line MR thermometry, was tested on turkey meat for different temperature rises (5°C, 10°C and 30°C). Two methods were compared. Method 1 uses only the temperature difference between the measured temperature and the desired temperature, with the change in wave amplitude set proportional to this difference. Method 2 in addition uses the slope of the latest three data points to modify the generator amplitude after each cycle of three temperature images. The evolution of focal point temperature using these two methods, shown in Figures 7.2a and 7.2b, respectively, demonstrates that it is possible to automatically maintain the temperature at a certain level under MR control. For each method, the standard deviation during the different temperature evolutions is given in Table 7.1. Both methods produced similar results. The main disadvantage of the first method is the overshoot when the temperature rises rapidly. The main disadvantages of the second method are the higher sensitivity to noise when calculating the slope and the lower time resolution.

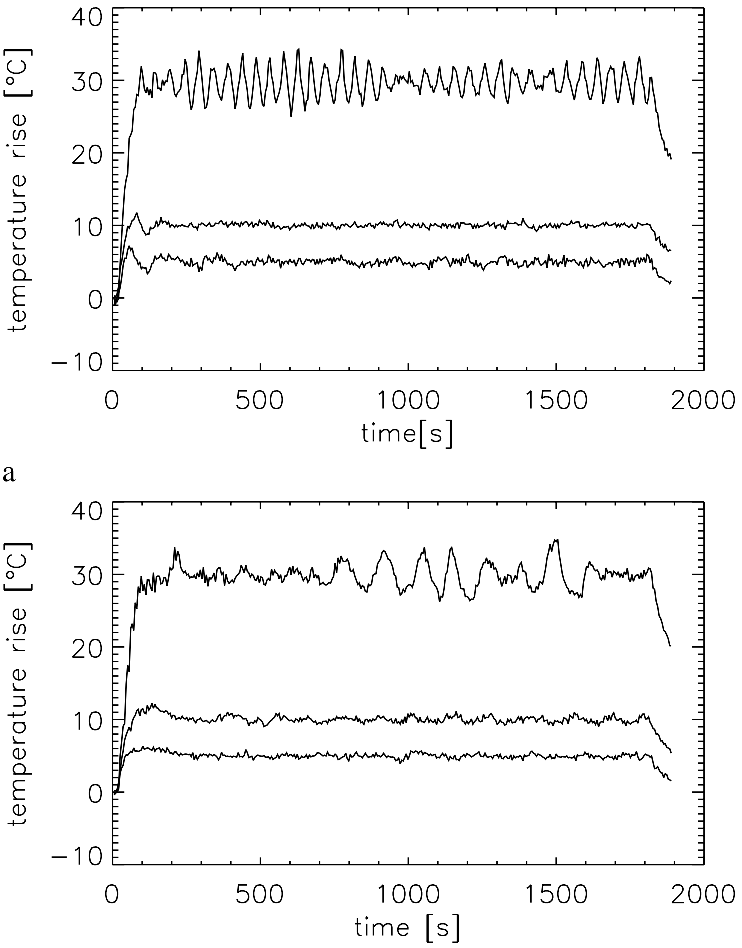

a

b

Figure 7.2: *Focal point temperature evolution under automatic FUS control, determined using MR thermometry. The experiments were performed using control method 1 (a) and control method 2 (b). See text for more details.*

| | Standard Deviation (°C) Using: | |
|---|---|---|
| Target Temperature Rise | Method 1 | Method 2 |
| 5°C | 0.54 | 0.38 |
| 10°C | 0.36 | 0.55 |
| 30°C | 1.81 | 1.64 |

Table 7.1: *Temperature stability during 30 minutes of MRI-controlled FUS heating at a constant temperature elevation using the two different control methods.*

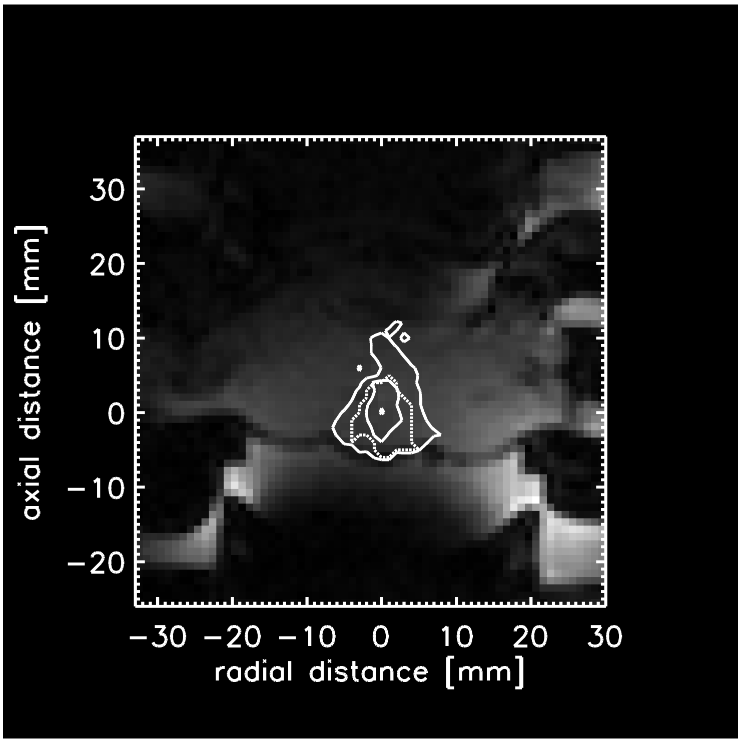

Figure 7.3: *Temperature mapping in rat thigh and tissue necrosis estimate. A temperature contour plot (solid lines, temperature levels 5°C, 10°C, and 15°C [focal point only]) and necrosis estimate contour plot (dotted line) are superposed on a $T_2^*$-weighted image. The transducer can be seen on the bottom of the image, whereas the rat skin is visible as a low-intensity line just below the center of the image. The focal point is located at coordinates [0,0], 5 mm into the rat thigh.*

### 7.3.2 Estimation of tissue necrosis

Figure 7.3 shows a transverse MR intensity image with overlaying temperature contours. Based on the temperature evolution in each voxel, the surface of the necrosed tissue zone in the imaging plane was calculated using the thermal dose estimate (Eq. 1.1) and subsequently compared to the volume of tissue necrosis determined using conventional tissue histology. Six rats were used, undergoing different heating protocols. In two rats the temperature elevation was limited to 8°C. No necrosis was seen on histologic examination (nor predicted based on the calculated necrosis estimate). With a temperature rise of more than 10°C, some degree of necrosis was seen in all animals. The difference between healthy tissue and necrosed tissue showed a sharp demarcation, as can been seen in Figure 7.4. In some cases, an edematous border area could be identified. These preliminary results in rat muscle confirmed approximate correspondence between tissue histology and necrosis estimate based on thermal dose evaluation, as has been demonstrated elsewhere [5].

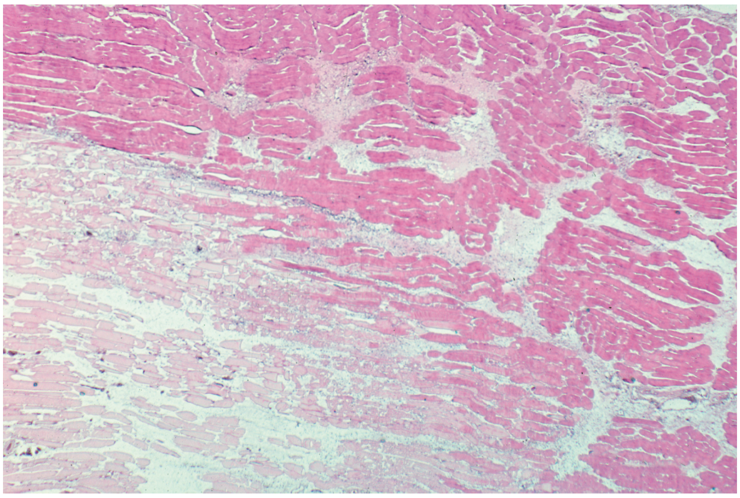

Figure 7.4: *Border region between healthy and necrosed tissue after treatment with FUS under automatic MR control. The boundary between healthy and necrosed tissue shows a sharp demarcation.*

## 7.4 Discussion and conclusion

Real-time FUS control by MRI has been shown to be feasible, based on a combination of rapid MR thermometry, fast on-line data processing, a dedicated MRI/FUS interface, and FUS control software. Using a combination of rapid temperature imaging and real-time thermal dose calculation, it is thus possible to control the FUS to get the desired necrosis volume, as well as to monitor tissue near the target region.

## References

[1] H.E. Cline, J.F. Schenck, K. Hynynen, R.D. Watkins, S.P. Souza, F.A. Jolesz, MR-Guided focused ultrasound surgery. *J. Comput. Assist. Tomogr.* **16(6)**, 956-965 (1992)

[2] D.P. Madio, P. van Gelderen, D. DesPres, A. Olson, J.A. de Zwart, T.W. Fawcett, N.J. Holbrook, M. Mandel, C.T.W. Moonen, On the feasibility of MRI-guided focused ultrasound for local induction of gene expression. *J. Magn. Res. Imaging* **8**, 101-104 (1998)

[3] D.L. Parker, Application of NMR imaging in hyperthermia: An evaluation of the potential for localized tissue heating and noninvasive temperature monitoring. *IEEE Trans. Biomed. Eng.* **31**, 161-167 (1984)

[4] H.E. Cline, K. Hynynen, C.J. Hardy, R.D. Watkins, J.F. Schenck, F.A. Jolesz, MR temperature mapping of focused ultrasound surgery. *Magn. Reson. Med.* **31**, 628-636 (1994)

[5] N. McDonnald, K. Hynynen, D. Wolf, G. Wolf, F.A. Jolesz, MRI evaluation of thermal ablation of tumors with focused ultrasound. *J. Magn. Res. Imaging* **8**, 91-100 (1998)

[6] Y. Isihara, A. Calderon, H. Watanabe, K. Mori, K. Okamoto, Y. Suzuki, K. Sato, K. Kuroda, N. Nakagawa, S. Tsutsumi, A precise and fast temperature mapping method using water proton chemical shift, in "Proc., SMRM, 11th annual meeting, Berlin, 1992", p. 4803

[7] J. De Poorter, C. De Wagter, Y. De Deene, C. Thomsen, F. Ståhlberg, E. Achten, Noninvasive MRI thermometry with the proton resonance frequency (PRF) method: In vivo results in human muscle. *Magn. Reson. Med.* **33**, 74-81 (1995)

[8] Y. Ishihara, A. Calderon, H. Watanabe, K. Okamoto, Y. Suzuki, K. Kuroda, Y. Suzuki, A precise and fast temperature mapping using water proton chemical shift. *Magn. Res. Med.* **34**, 814-823 (1995)

[9] J.A. de Zwart, P. van Gelderen, D.J. Kelly, C.T.W. Moonen, Fast magnetic-resonance temperature imaging. *J. Magn. Res. B* **112**, 86-90 (1996)

[10] S.A. Sapareto, W.C. Dewey, Thermal dose determination in cancer therapy. *Int. J. Radiation Oncology Biol. Phys.* **10**, 787-800 (1984)

# Chapter 8

# MR-Controlled Hyperthermia Based on a Physical Model

## Contents

**8.1 Introduction** **104**
**8.2 Theory** **104**
**8.3 Materials and methods** **106**
  8.3.1 Experimental setup 106
  8.3.2 Image processing 106
**8.4 Results and discussion** **108**
  8.4.1 Estimating heat conduction and energy absorption 108
  8.4.2 Performance using correct parameter estimates 108
  8.4.3 Performance in case of parameter errors 110
**8.5 Conclusion** **112**

Adapted from:
Rares Salomir, Frédéric C. Vimeux, Jacco A. de Zwart, Nicolas Grenier, Chrit T.W. Moonen
”Hyperthermia by MR Guided Focused Ultrasound: Accurate Temperature Control Based on Fast MRI and a Physical Model of Local Energy Deposition and Heat Conduction”
*Magnetic Resonance in Medicine* [in press]

## 8.1 Introduction

In FUS hyperthermia procedures, the variance of ultrasound properties with tissue composition is a major problem. In addition, heat conduction through diffusion and perfusion processes may vary locally as a function of tissue architecture, tissue composition, local physiological parameters, and temperature. As a consequence, both energy deposit and heat losses are difficult to predict in advance of the procedure.

Therefore, direct feedback to the ultrasound apparatus, based on thermometry data, is necessary to guarantee a targeted temperature evolution. Initial attempts of this laboratory and others [1, 2] used conventional control methods without an underlying realistic physical model of energy deposit and heat loss. These methods are similar to the common PID (proportional, integral, derivative) type of control mechanism and are based on the temperature evolution in the focal point. Conventional thermometry has been used for control of FUS, but without a realistic physical model of heat exchange [3, 4].

Since the experimental parameters are difficult to predict and the noise in temperature MRI is significant, it was anticipated that real-time evaluation of the temperature gradients during FUS hyperthermia using a realistic physical model might lead to a better control system. Such a system is presented here, together with an evaluation of its performance in situations in which the initial estimates of FUS energy absorption and heat losses were incorrect.

## 8.2 Theory

The control mechanism is based on the bioheat equation, which describes the flow of applied heat away from its source [5, 6]. Since rapid heating is assumed, perfusion is neglected.

$$\alpha_2(\vec{r},T)P'(\vec{r},t) = -\alpha_1(\vec{r},T)\nabla^2 T(\vec{r},t) + \frac{\partial T(\vec{r},t)}{\partial t} \tag{8.1}$$

$P'(\vec{r},t)$ is the spatial distribution of the applied FUS, determined by the acoustic field and the electrical power $P(t)$, which is the parameter modified by the control software. $\alpha_2$ is the FUS absorption-coefficient of the tissue, $\alpha_1$ the coefficient for heat diffusion, where isotropic and slowly spatially varying diffusivity is assumed. $T$ is the temperature rise above body temperature. $\nabla^2$ is the Laplacian operator, defined as: $\frac{\partial^2}{\partial x^2} + \frac{\partial^2}{\partial y^2} + \frac{\partial^2}{\partial z^2}$. Note that the functions $\alpha_1(\vec{r},T)$ and $\alpha_2(\vec{r},T)$ are not precisely known at the start of the heating procedure.

For a fixed, single-element FUS transducer, only the power transmitted to the probe ($P(t)$) can be modified on-line by the control system. The transducer geometry and the refractive index distribution in the tissue determine the acoustic field (see chapter 3), which are accounted for in $P'(\vec{r},t)$. Consequently, only the temperature in the focal point can be controlled, whereas the temperature evolution elsewhere involves spatially and temperature dependent functions such as the acoustic power field, the heat diffusivity in the tissue, $\alpha_1(\vec{r},T)$, and the FUS absorption, $\alpha_2(\vec{r},T)$. Note that the acoustic power field of a spherical, single element FUS transducer has approximately a gaussian distribution around the focal point, with a 6 dB attenuation radius denoted as $R_0$, the specific heat diffusion time $\tau$ then equals to $R_0^2/2\alpha_1$, which is on the order of 10 sec for a FUS wavelength of 1 mm.

For the FUS control mechanism, the objectives were twofold: First, the temperature in the focal point should reach the target value as fast as possible without overshooting or oscillating. Second, having reached the target value, the temperature should remain constant for a user-defined period.

Let $\Theta(t)$ be the targeted time evolution for the focal point temperature ($T_{max}(t)$). The integrals of the target function, the experimentally observed evolution of the maximum temperature, and the difference between them are then respectively:

$$\Omega(t) = \int_0^t \Theta(t')dt' \tag{8.2}$$

$$\Psi(t) = \int_0^t T_{max}(t')dt' \tag{8.3}$$

$$\Delta(t) = \Omega(t) - \Psi(t) = \int_0^t \left[\Theta(t') - T_{max}(t')\right] dt' \tag{8.4}$$

Using the second derivative of Eq. 8.4, the heat equation (Eq. 8.1) in the focal point can be expressed in $\Delta(t)$ instead of $T_{max}(t)$:

$$\frac{d^2\Delta(t)}{dt^2} = \frac{d\Theta(t)}{dt} - \alpha_1(T_{max})\nabla^2 T_{max}(t) - \alpha_2(T_{max})P(t) \tag{8.5}$$

where is assumed that in the focal point $\vec{r} = (0,0,0)$, and that $P(t)$=$P'(0,0,0,t)$.

Note that a second order, linear differential equation in $\Delta(t)$ offers particular advantages for the control system, similar to those of a PID control system. The reason is that the solution for $\Delta(t)$ of such an equation approaches asymptotically to zero, as does its first derivative. If the first derivative of $\Delta(t)$ equals zero, $T_{max}(t)$ overlaps with the targeted time evolution $\Theta(t)$. This is the basic idea of the control system. Therefore, we shall rewrite Eq. 8.5 into a second order, linear differential equation in $\Delta(t)$ of the type:

$$\frac{d^2\Delta}{dt^2} + a \cdot \frac{d\Delta}{dt} + \frac{a^2}{4} \cdot \Delta = 0 \qquad where: \;\; a > 0 \tag{8.6}$$

In order to obtain an expression similar to Eq. 8.6 from Eq. 8.5, $P(t)$ in Eq. 8.5 should be substituted by:

$$P(t) = \frac{1}{\alpha_2(T_{max})}\left[\frac{d\Theta(t)}{dt} - \alpha_1(T_{max})\nabla^2 T_{max}(t) + a \cdot [\Theta(t) - T_{max}(t)] + \frac{a^2}{4}\Delta(t)\right] \tag{8.7}$$

Eq. 8.7 is used to calculate the FUS power-level on-line. From the solution of the second order differential equation (Eq. 8.6) it can be seen that the parameter $a$ is related to the characteristic response time $t_r$ of the regulation loop ($a$=2/$t_r$). It is assumed in Eq. 8.6 and 8.7 that all functions used to calculate the ultrasound power are precisely known. The experimentally observed temperature then shows an asymptotic approach to the target function:

$$\Theta(t) - T(t) = \frac{d\Delta}{dt}(t) = [\Theta(0) - T(0)] \cdot \left(1 - \frac{a}{2}t\right) \cdot e^{\left(-\frac{a}{2}t\right)} \tag{8.8}$$

In reality, the values for energy absorption and energy loss are estimated, only the target function and its derivative are precisely known. In addition, $T_{max}(t)$ and $\nabla^2 T_{max}(t)$ are obtained from the MR temperature maps and thus affected by noise. Note that the values for $\alpha_1$ and $\alpha_2$ are not adjusted by the control software. Any possible estimation error or temperature dependent change in $\alpha_1$ or $\alpha_2$ is compensated by the control software by means of the $\Delta(t)$-term in Eq. 8.7. Therefore, initial estimates for $\alpha_1$ and $\alpha_2$ are maintained throughout the heating experiment for the calculation of the ultrasound power according to Eq. 8.7. The tolerance for errors in the initial estimates will be analyzed below.

## 8.3 Materials and methods

### 8.3.1 Experimental setup

Both segmented-EPI and PRESTO sequences [7] were used for MR thermometry based on the water proton resonance frequency (PRF) [8-10]. Scan parameters for in vitro experiments were: segmented-EPI; 50 msec TR; 15 msec TE; 64 × 63 image matrix; 3 lines of k-space per TR; 64 × 63 $\text{mm}^2$ field-of-view; 2 mm slice thickness. Temporal resolution was 1.05 sec and the spatial resolution 1 × 1 × 2 $\text{mm}^3$.

Segmented EPI-data in vivo were acquired using: 30 msec TR; 14 msec TE; 64 × 60 image matrix; 5 lines of k-space per TR; 64 × 64 $\text{mm}^2$ field of view; 3 mm slice thickness; binomial excitation for lipid suppression [11]; 510 msec temporal resolution (360 msec scan-time per image, 150 msec delay between dynamics). Scan parameters for the PRESTO sequence during in vivo experiments were: echo shifting over 1 TR period; 256 dummy scans; 13.8 msec TR; 23 msec TE; 64 × 64 mm field-of-view; 64 × 63 matrix size; 3 mm slice thickness; binomial excitation with 2236 $\mu$sec pulse separation ($\tau$); 400 dynamics; 495 msec temporal resolution (289 msec scan-time, 106 msec delay between dynamics).

In all experiments, a PRF temperature dependence of 0.0094 $\text{ppm}\cdot\text{K}^{-1}$ was used to convert phase information in MR images into temperature (see chapter 4) [11, 12]. A transverse image plane was chosen in such a way that it includes the FUS focal point.

Male Wistar rats (weight 325-500 g) were anesthetized using halothane (1%) and a mixture of nitrous oxide/oxygen (7:3) under an approved protocol. In order to improve passage of the ultrasound beam into the tissue, fur on one of the thighs was completely removed using hair remover. Endorectal temperature was monitored throughout the in vivo experiments, employed to maintain body temperature at 35°C using a thermostatic water bath [11, 13]. Rats were sacrificed after the heating procedure.

### 8.3.2 Image processing

Data processing and FUS control calculations were performed on a Dec Alpha PW 500a workstation (in-house written software using IDL, RSI, Boulder, CO). MR data were processed as

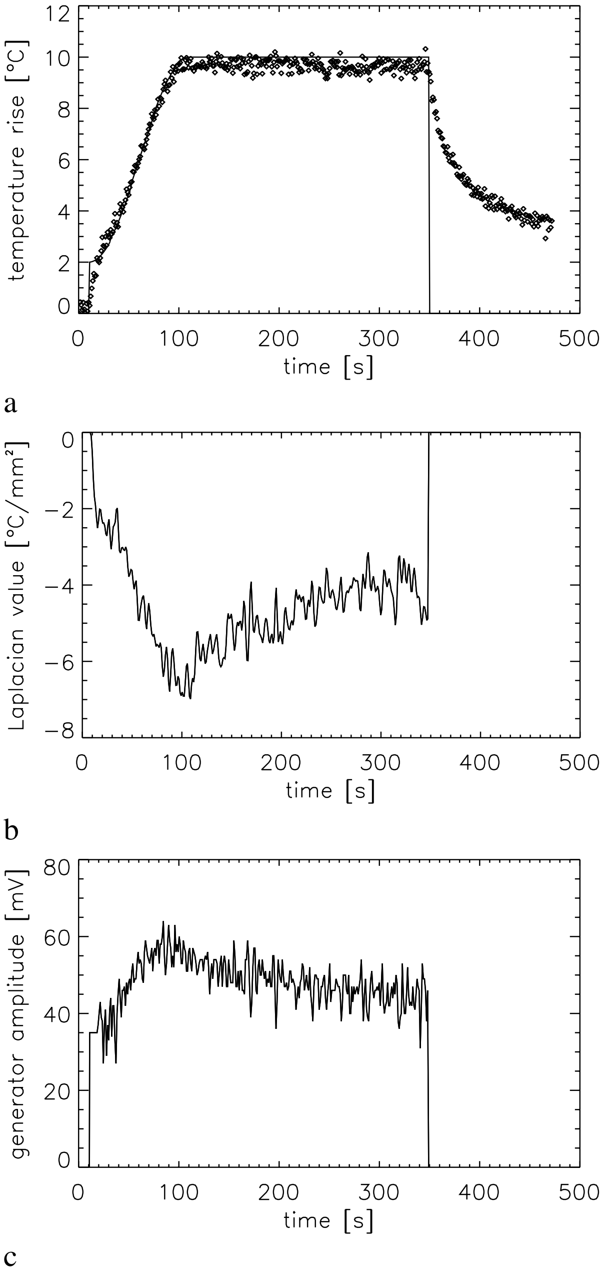

Figure 8.1: *(a) Focal point temperature rise in a fresh meat sample during automatic FUS control, measured using MR thermometry. The values used for* $\alpha_1$ *and* $\alpha_2$ *were approximately correct (determined using a pilot experiment). The solid curve represents the targeted temperature evolution. (b) On-line calculated Laplacian in the focal point. (c) FUS generator amplitude, as calculated by the control mechanism.*

described in chapter 6. A targeted time evolution of the temperature in the focal point was defined prior to the start of each experiment. It consisted of an initial ascending part (profile of the second half of a cosine-period, between $\pi$ and $2\pi$ radians) followed by a period of constant temperature. The first derivative of this curve is continuous and was numerically computed.

The value for the Laplacian operator for the focal point when applied to the measured temperature maps (from here on simply referred to as the Laplacian) was calculated using a finite element method in combination with a temporal filter for noise reduction (using a binomial weighting ratio of 1:4:6:4:1 over 5 images). The $\Delta(t)$ integral (as defined in Eq. 8.4) was numerically computed. The maximum temperature was taken directly from the MR temperature maps. FUS settings were calculated using Equation 8.7 as described in the Theory-section. Total time for data processing was less than 250 msec per image (see chapter 6).

## 8.4 Results and discussion

### 8.4.1 Estimating heat conduction and energy absorption

The parameters for energy loss ($\alpha_1$) and FUS energy absorption ($\alpha_2$) were estimated using a preliminary constant-power FUS heating experiment. $\alpha_1$ was calculated as the time derivative of the focal point temperature immediately after the FUS power was switched off, divided by the Laplacian (average over five images). $\alpha_2$ was calculated as the initial time derivative of the focal point temperature relative to the FUS power (when FUS is switched on and diffusion is negligible, see Eq. 8.1). The accuracy of the estimates was better than 10%, judged from repeated experiments. The values were used by the control software to calculate the generator amplitude, via Eq. 8.7, each time a new temperature map was available.

### 8.4.2 Performance using correct parameter estimates

An experiment with a targeted 10°C temperature rise was performed on a fresh meat sample, baseline temperature was 15°C. No irreversible tissue modifications are expected as a result of this temperature trajectory. Figure 8.1a shows the focal point temperature as a function of time. In the flat part of the profile, the average temperature rise is 9.7°C with a standard deviation of 0.22°C, compared to a standard deviation of noise in the temperature measurement of 0.16°C in the same voxel (determined over the first 10 images, before FUS heating was started). In Figure 8.1b the Laplacian in the focal point, calculated on-line, is plotted. The diminishing temperature gradients around the focal point induce an attenuation of the Laplacian during the period of constant focal point temperature. This is reflected by the applied generator amplitude, plotted in Figure 8.1c, which diminishes during the period of constant temperature. Because of noise in MR temperature data, both the calculated value of the Laplacian and the generator amplitude show approximately 10% fluctuation. This has little effect on the resulting temperature since the temporal resolution of the MR experiment (and thus the frequency of the fluctuation) is higher than the specific heating response time of the tissue ($\tau$).

Figure 8.2 shows the results of two FUS heating experiments on rat thigh in vivo, performed under automatic control. In both experiments, the temporal resolution was 0.5 sec. Figure 8.2a shows a segmented-EPI experiment under automatic control. The average temperature between 60 and 115 sec into the experiment was 54.4°C (target temperature 55°C) with a standard deviation of 0.48°C. The standard deviation of the noise in measured temperature was 0.39°C for

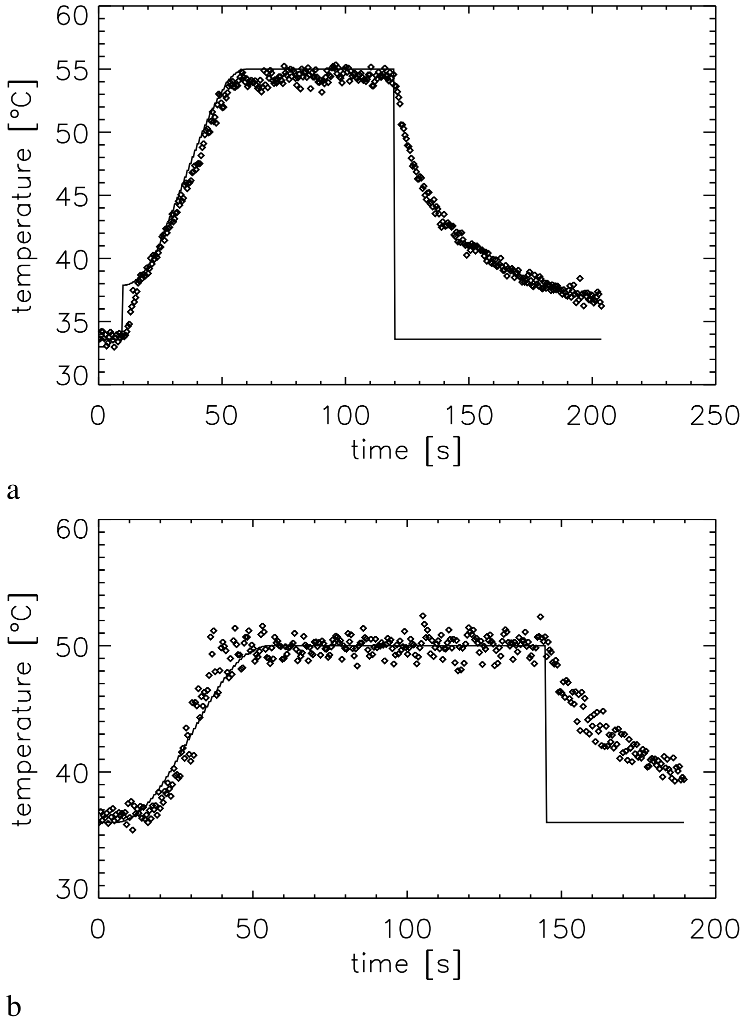

Figure 8.2: *Two examples of the evolution of focal point temperature during in vivo FUS heating of rat thigh under automatic control. MR measurements (◇) are superimposed on the targeted temperature-time evolution (solid line). A value of 0.2* $s^{-1}$ *was used for the parameter a. (a) interleaved gradient echo EPI sequence. (b) PRESTO with binomial excitation for lipid suppression and echo shifting over one TR period.*

the focal point voxel, as was determined over the first 16 temperature maps (before the start of FUS heating).

Note that the average focal point temperature is somewhat below target temperature, since the control software assumes that the maximum temperature found in the latest image is the focal point temperature. If two neighboring voxels have approximately the same temperature, this value might be biased by noise.

Fig. 8.2b shows the result of a similar experiment where data were acquired using a PRESTO sequence with echo shifting over one TR period. Standard deviation in the period of constant temperature (60 to 140 sec into the experiment) was 0.74°C for the focal point voxel, standard deviation of the measured temperature was 0.53°C in the focal point (determined over the first 32 temperature maps). Average temperature during the constant part of the heating cycle was 50.0°C, corresponding to the target temperature.

These results demonstrate temperature control with a precision close to the precision of the temperature measurement.

### 8.4.3 Performance in case of parameter errors

The values of $\alpha_1$ and $\alpha_2$ and their temperature dependence are not precisely known. Both parameters depend on tissue composition, physiological processes (like perfusion), and irreversible tissue changes that might occur during ablation procedures. Therefore, the regulation system should be tolerant for errors in $\alpha_1$ and $\alpha_2$. A theoretical analysis of the effect of erroneous values for $\alpha_1$ and $\alpha_2$ in Eq. 8.7 indicates the following: 1) An erroneous estimate of the absorption parameter reduces the efficiency of the regulation loop, possibly leading to over- and undershooting of temperature and an increased convergence time. However, the experimental temperature will still approach the target function. 2) An erroneous estimate of the heat diffusivity leads to a constant offset in experimental temperature with respect to the constant temperature region in the target function. This offset is proportional to the first time derivative of the Laplacian, multiplied by the absolute error in $\alpha_1$, multiplied by $a^{-2}$. In order to estimate this effect, the Laplacian derivative was estimated from the data shown in Figure 8.1b (by linear regression of the data between 150 and 250 sec). The obtained value was of the order of 0.01 $\text{K}\cdot\text{mm}^{-2}\cdot\text{s}^{-1}$, leading to a temperature offset in the order of 0.1°C, an error which is not directly observable since it is inferior to the precision of MR thermometry.

The influence of erroneous values for $\alpha_1$ and $\alpha_2$ on the control efficiency was experimentally studied on a piece of fresh meat. The desired temperature trajectory consisted of a 100 sec rise (shape of second half of a cosine period) of 10°C, followed by a 240-sec period of constant temperature at 10°C above starting temperature. Automatic FUS heating protocols were repeatedly performed using different combinations of estimates for $\alpha_1$ and $\alpha_2$. The heat conduction estimate varied between 0 and 300% of the correct value (determined using a pilot experiment, see above). FUS absorption values from 40 to 250% of the correct value were used. Thirty-minute delays between successive experiments allowed an identical and spatially uniform baseline temperature to be established.

Nine representative results are shown in Figure 8.3. The results indicate a large tolerance for errors in initial estimates of $\alpha_1$ and $\alpha_2$. However, note that the control loop becomes unstable when diffusion is strongly overestimated, particularly in combination with an underestimation of absorption. We tentatively attribute this effect to the experimental noise in MR temperature measurements. When a noise-affected calculation results in an overestimated value for the

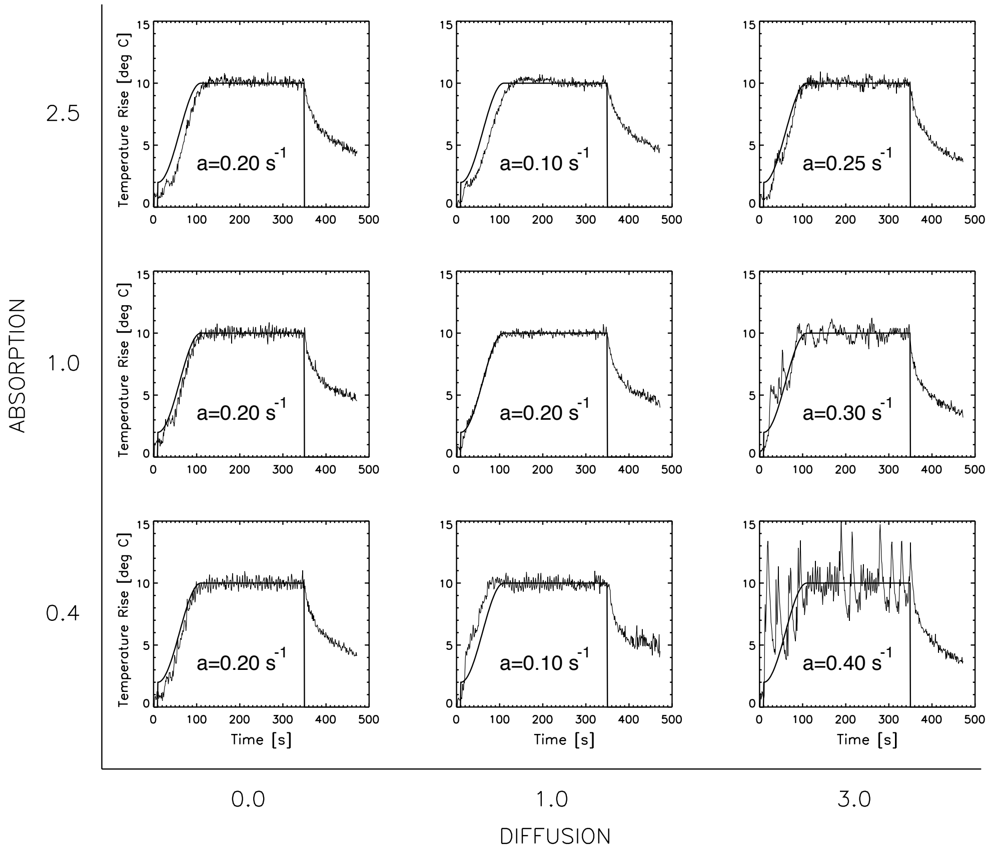

Figure 8.3: *Performance of the temperature regulation system in case of erroneous estimate of heat conduction* ($\alpha_1$) *and FUS power absorption* ($\alpha_2$). *Identical heating experiments were performed for nine combinations of* $\alpha_1$ *and* $\alpha_2$. *Data for the center plot were acquired using correct values for both* $\alpha_1$ *and* $\alpha_2$. *Parameter values are tabulated relative to the correct value. The negative reaction strength, a, for each experiment is indicated inside the respective plots.*

Laplacian (second derivatives being sensitive to noise), the increase in applied FUS power is equal to $\alpha_1\varepsilon/\alpha_2$, where $\varepsilon$ is the Laplacian over-estimation. Increasing FUS power leads to a real increase of the Laplacian in the tissue and therefore to a new FUS power increase. This positive reaction will be stopped after approximately $2/a$ sec by a negative reaction of the control loop, which explains the periodicity of the instabilities in this extreme example.

The negative reaction strength of the regulation loop used for each of the experiments ($a$ in Eq. 8.7) is indicated in the corresponding plot in Figure 8.3. Generally, values for $a$ between 0.1 $s^{-1}$ and to 0.2 $s^{-1}$ were sufficiently high to allow the temperature rise to match the target evolution even when erroneous values for $\alpha_1$ and $\alpha_2$ were used. Only in the extreme case of combined strong underestimation of heat conduction and overestimation of FUS absorption (Figure 8.3, bottom right), $a$ had to be increased to 0.40 $sec^{-1}$ in order to allow some control over the heating procedure, although strong fluctuations persist. The experimentally found optimum value for $a$ (for all but extreme errors in $\alpha_1$ and $\alpha_2$) is $0.2\ s^{-1}$, the corresponding response time of the regulation loop being 10 sec. Increasing the strength of the negative reaction leads to a faster compensation of the initial parameters errors, however, the amplitude of the FUS power fluctuations around the target value increases.

## 8.5 Conclusion

A new temperature control method for MR-guided FUS is presented, based on non-invasive, fast temperature mapping and a realistic physical model of heat conduction. The system has shown excellent performance in vitro and in vivo, with a large tolerance for errors in the estimate of heat conduction and energy absorption. It is anticipated that the method presented here will be useful for other local hyperthermia techniques, such as those using RF or laser.

## References

[1] F.C. Vimeux, J.A. de Zwart, J. Palussière, R. Fawaz, C. Delalande, P. Canioni, N. Grenier, C.T.W. Moonen, Real-time control of focused ultrasound heating based on rapid MR thermometry. *Invest. Radiol.* **34**, 190-193 (1999)

[2] N.B. Smith, N.K. Merrilees, S. Sokka, K. Hynynen, Control system for an MRI compatible intracavitary ultrasound array for thermal treatment of prostate disease. Proceedings annual meeting of the International Society for Magnetic Resonance in Medicine 672 (1999)

[3] P.D. VanBaren, E.S. Ebbini, Multi-point temperature control during hyperthermia treatments: theory and simulation. *IEEE Trans. Biomed. Engin.* **42**, 818-827 (1995)

[4] Y.Y. Chen, W.L. Lin, H.L. Liou, J.Y. Yen, M.J. Shieh, Self-tuning fuzzy logic control for ultrasound hyperthermia with reference temperature based on objective functions. *Med. Phys.* **26**, 825-834 (1999)

[5] H.H. Pennes, Analysis of tissue and arterial blood temperatures in the resting human forearm. *J. Appl. Physiol.* **1**, 93-122 (1948)

[6] H.E. Cline, K. Hynynen, C.J. Hardy, R.D. Watkins, J.F. Schenck, F.A. Jolesz, MR temperature mapping of focused ultrasound surgery. *Magn. Reson. Med.* **31**, 628-636 (1994)

[7] G. Liu, G. Sobering, J. Duyn, C.T.W. Moonen, A functional MRI technique combining principles of echo-shifting with a train of observations (PRESTO). *Magn. Reson. Med.* **30**, 764-768 (1993)

[8] Y. Ishihara, A. Calderon, H. Watanabe, K. Okamoto, Y. Suzuki, K. Kuroda, Y. Suzuki, A precise and fast temperature mapping using water proton chemical shift. *Magn. Reson. Med.* **34**, 814-823 (1995)

[9] J. De Poorter, C. De Wagter, Y. De Deene, C. Thomsen, F. Ståhlberg, E. Achten, Noninvasive MRI thermometry with the proton resonance frequency (PRF) method: in vivo results in human muscle. *Magn. Reson. Med.* **33**, 74-81 (1995)

[10] R.D. Peters, R.S. Hinks, R.M. Henkelman, Ex vivo tissue-type independence in proton-resonance frequency shift MR thermometry, *Magn. Reson. Med.* **40**, 454-459 (1998)

[11] J.A. de Zwart, F.C. Vimeux, C. Delalande, P. Canioni, C.T.W. Moonen, Fast lipid suppressed MR temperature mapping with echo-shifted gradient echo imaging and spectral-spatial excitation. *Magn. Reson. Med.* **42**, 53-59 (1999)

[12] J.A. de Zwart, P. van Gelderen, D.J. Kelly, C.T.W. Moonen, Fast magnetic-resonance temperature imaging. *J. Mag. Res. B* **112**, 86-90 (1996)

[13] D.P. Madio, P. van Gelderen, D. DesPres, A. Olson, J.A. de Zwart, T.W. Fawcett, N.J. Holbrook, M. Mandel, C.T.W. Moonen, On the feasibility of MRI-guided focused ultrasound for local induction of gene expression. *J. Magn. Res. Imaging* **8**, 101-104 (1998)

# Chapter 9

# Implementation on a Clinical Scanner

## Contents

**9.1 Introduction** **116**

**9.2 FUS transducer and setup** **116**

**9.3 MR sequences** **116**

**9.4 Data handling** **116**

9.4.1 User interface 117

**9.5 Heating trajectories** **118**

**9.6 Discussion** **119**

## 9.1 Introduction

This chapter describes the current status of the transfer of MR thermometry and FUS control technology to a whole-body MR scanner. A prototype FUS setup is combined with a 1.5 T Philips ACS-NT scanner (Philips Medical Systems, Best, Netherlands), equipped with PT-6000 gradient system (23 mT·m$^{-1}$, 105 mT·m$^{-1}$·s$^{-1}$).

## 9.2 FUS transducer and setup

The prototype FUS setup has been developed by the Philips electronics research laboratory LEP (Laboratoires d'Electronique Philips, Limeil-Brévannes, France). It has been integrated in a standard MR scanner-bed. The FUS transducer is 96 mm in diameter and consists of 14 concentric elements, of which phase and amplitude can be controlled independently. The radius of curvature and default focal depth of the transducer are 130 mm, the focal depth can be set electronically anywhere in the range from 55 to 160 mm. The transducer has been mounted on a platform which can be moved hydraulically, allowing displacement of the transducer in the horizontal plane over a distance of approximately 80 × 80 mm$^2$ (maximum speed approximately 10 mm·s$^{-1}$). Control of the hydraulic displacements and of the phase and amplitude of the signal, sent to each of the 14 elements, is done via a RS-232 serial connection, using an IBM-compatible PC. The routines handling FUS position and signal amplitude and phase settings were written in C.

## 9.3 MR sequences

Various conventional RF-spoiled gradient echo sequences, with or without echo-shifting, are available on the Philips whole body scanner. Binomial excitation is also implemented. The acquisition of multi-slice or three-dimensional data is possible at a timescale of a few seconds, however, the reconstruction hardware is not capable to reconstruct 3D-data in real-time. Initial experiments were therefore performed using the available multi-slice gradient-echo EPI sequences with or without echo-shifting.

## 9.4 Data handling

Reconstruction of magnitude and phase MR images is done using the standard Philips hard- and software. After data reconstruction, a copy of the data is sent on a slice-by-slice basis over a standard TCP/IP network to a Dell Precision 410 PC (Dell, Round Rock, TX), which runs the Linux operating system. On the Philips scanner, data are archived as usual.

The software for the communication between MR scanner and PC was developed by Philips Medical Systems. The receiving part, running on the Dell PC, has been modified in-house, all received images and scan parameters were stored in shared memory. At the beginning of each new experiment, all contents of the shared memory were discarded.

The thermometry and FUS control software have been written in IDL. A subroutine, which is written in C, allows access to shared memory for data retrieval. Data handling is similar to a previous description in chapter 6, with additional support for multi-slice and three-dimensional

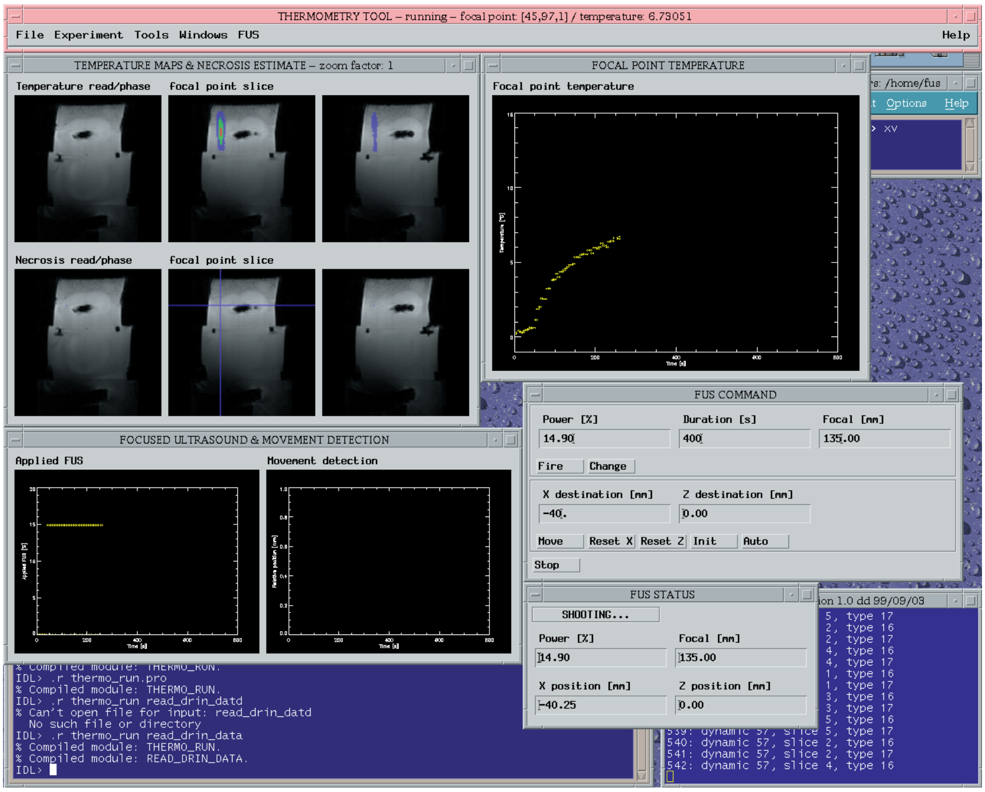
THERMOMETRY TOOL – running – focal point: [45,97,1] / temperature: 6.73051
File Experiment Tools Windows FUS
Help
TEMPERATURE MAPS & NECROSIS ESTIMATE – zoom factor: 1
Temperature read/phase
focal point slice
Necrosis read/phase
focal point slice
FOCAL POINT TEMPERATURE
Focal point temperature
Temperature [°C]
Time [s]
FOCUSED ULTRASOUND & MOVEMENT DETECTION
Applied FUS
Movement detection
Applied FUS [%]
Relative position [mm]
Time [s]
FUS COMMAND
Fire
Change
Move
Reset X
Reset Z
Init
Auto
Stop
FUS STATUS
SHOOTING...
ion 1.0 dd 99/09/03
Options
Help

Power [%] 14.90
Duration [s] 400
Focal [mm] 135.00
X destination [mm] -40.
Z destination [mm] 0.00

Power [%] 14.90
Focal [mm] 135.00
X position [mm] -40.25
Z position [mm] 0.00

```
% Compiled module: THERMO_RUN.
IDL> .r thermo_run.pro
% Compiled module: THERMO_RUN.
IDL> .r thermo_run read_drin_datd
% Can't open file for input: read_drin_datd
  No such file or directory
IDL> .r thermo_run read_drin_data
% Compiled module: THERMO_RUN.
% Compiled module: READ_DRIN_DATA.
IDL>
```

```
5, type 17
2, type 16
2, type 17
4, type 16
4, type 17
1, type 16
1, type 17
3, type 16
3, type 17
5, type 16
539: dynamic 57, slice 5, type 17
540: dynamic 57, slice 2, type 16
541: dynamic 57, slice 2, type 17
542: dynamic 57, slice 4, type 16
```

Figure 9.1: *The user interface of the temperature control software running on the Philips 1.5T system. The interface allows manual setting of the FUS parameters (position, power), and provides information about the focal point temperature history, the current temperature distribution, FUS power applied during the experiment and current FUS parameters.*

MR experiments. Navigator data are not yet available on the PC in real-time, this requires modifications of reconstruction software by Philips Medical Systems, which were not completed at the time of writing. Displacement detection and correction have therefore not yet been implemented.

### 9.4.1 User interface

The user interface of the software developed for the whole body setup is shown in Fig. 9.1. Various functions can be activated from pull-down menus in the main title bar along the top of the screen, comprising: start/stop experiment; reanalysis of data from disk; definition of targeted temperature evolution; selection of region-of-interest/signal intensity threshold for temperature calculation; modify setup/preferences; and quit.

The group of windows on the top-left shows the current temperature distribution (top row), focal point location and necrosis estimate (bottom row). The latest available temperature information is displayed as a transparent three-color overlay on top of the latest available signal intensity data. The current focal point location is indicated in the bottom row by the intersection of three blue lines. In addition, voxels where the applied thermal dose exceeds the limit for tissue necrosis (see chapter 1) are marked in transparent red. The experiment during which Fig. 9.1 was obtained was performed on an agarose gel containing a bone sample. The gel can be observed in the top half of the images (bright area), in which the bone shows up as a low-intensity area just above the center of the image. The bottom part of the gel is suspended in a water reservoir to assure effective transmission of FUS into the gel. The lower part of the reservoir contains the FUS transducer (visible as a curved low-intensity area in the lower part of the image), and is separated from the gel by a protective film of mylar.

The way in which data are presented in these two rows of images depends on the type of MR experiment. In case of a single-slice experiment, only the left-most window of each row is used to display information about the single available slice. In case of multi-slice data, information about the slice containing the current focal point is displayed in the center windows, data from the slice below and above the focal-point slice are presented in the neighboring windows. Finally, during a three-dimensional MR experiment, the left-most window is used to display data from the read-out/phase-encode plane through the focal point. The middle window shows data from the read-out/slice plane through focal point, the right-most window information about the phase-encode/slice plane.

Clicking the left mouse button while the pointer is over one of the six windows will zoom in to the area surrounding the focal point by a factor of two the next time the windows are updated (maximal zoom factor of eight). The zoom factor is reduced by a factor of two when the right mouse button is clicked.

The largest window on the screen is used to display the evolution of focal point temperature as a function of time. MR temperature data are superimposed on the targeted time evolution, if available. Note that the voxel with the highest temperature is taken as focal point. Before the start of FUS application, the "focal point" temperature will thus be determined by the maximum positive noise in the selected region-of-interest. The two windows on the lower-left side of the screen display respectively the outcome of the applied FUS power and navigator analysis (not yet implemented at the time of writing).

The remaining two windows show FUS status (bottom window) and allow modification of FUS settings (top window). During automatic FUS control, only the stop-button is active, all other functions are disabled. During manual FUS heating, FUS power, focal depth and position can be modified on-the-fly.

## 9.5 Heating trajectories

FUS heating in a fixed point in space under control of MR temperature imaging has been implemented, the software is similar to the one described in chapter 8. Since the FUS setup described here allows moving of the focal point during the intervention, larger regions can be heated in a single session. The FUS transducer should follow a trajectory such that a minimal thermal dose is delivered to the entire target volume. The optimal heating trajectory for variously shaped target regions is currently under investigation. Ideally, the entire target volume receives a predefined thermal dose, while damage to surrounding tissues is avoided.

For tumors that approach a spherical or cylindrical shape, a spiral heating trajectory seems advantageous [1]. Starting in the center, the focal point spirals outwards towards the edge of the target zone. The temperature throughout the trajectory can be controlled using an approach similar to the one described in chapter 8. If necessary, multiple spirals applied to different parallel planes can be used to cover a more important volume.

## 9.6 Discussion

It has been demonstrated that FUS heating under MR control is feasible at a standard clinical MR instrument. The Philips scanner-hardware is unmodified, the only modifications to the instrument are a prototype FUS setup which is implemented in the patient-support, and software which transfers a copy of all reconstructed images to subscribed client software, which in this case is running on a PC. At the moment, navigator data are not accessible in real-time on the PC. It is however expected that real-time evaluation of motion is important for future clinical FUS applications.

## References

[1] F. Vimeux, J. de Zwart, R. Salomir, P. Lelong, M. Gauchet, J. Pergrale, N. Grenier, C.T.W. Moonen, MR-guided focused ultrasound: A spiral heating trajectory with real-time temperature mapping in a clinical MR-instrument. “16th Annual Meeting ESMRMB, Sevilla, Spain, 1999”, p. 216

# Part IV

# Applications: Tissue Ablation

# Chapter 10

# On the Feasibility of On-Line Necrosis Prediction

## Contents

**10.1 Introduction** **124**

**10.2 Materials and methods** **124**

  10.2.1 Thermal dose calculation and noise correction 125

**10.3 Results and discussion** **127**

**10.4 Conclusion** **127**

## 10.1 Introduction

As has been discussed in the introduction (chapter 1), the relationship between the product of temperature and time of exposure and tissue necrosis (the applied "thermal dose") is nonlinear. A model describing this relationship, empirically based on data from literature, has been described by Sapareto and Dewey [1]. This concept of thermal dose has been suggested as a good parameter for the estimation of necrosis during the intervention [2], but this is contested in other work [3, 4].

Energy deposition using focused ultrasound (FUS) is highly localized for short periods of FUS-hyperthermia, local induction of tissue necrosis is thus expected, sharply demarcated from surrounding tissue. Clinical trials using FUS have been performed, both for the ablation of hypertrophied prostatic tissue [5, 6] and for treatment of glaucoma [7]. Success of the intervention varied, mainly due to the lack of information about the exact location of the FUS focal point in the tissue, and the unknown temperature evolution (thermal dose). Thermal dose is difficult to predict beforehand, since both FUS-deposition and heat flow around the focal point are tissue dependent. FUS focalization and attenuation characteristics depend on the presence and orientation of interfaces in the beam path, while heat flow around the FUS focal point depends on heat diffusivity and perfusion in the target tissue.

FUS-hyperthermia has received increased attention since combination with magnetic resonance imaging (MRI) was suggested [8]. Magnetic resonance imaging can be used to guide, monitor and control FUS during treatment.

The purpose of this study was to investigate the feasibility of on-line spatially resolved necrosis estimation, based on MR temperature maps [9]. Accurate temperature control [10] and online processing of MR temperature data [11] were employed. Tissue necrosis was evaluated by conventional histology. A similar study has recently been published by Chung et al. [12].

## 10.2 Materials and methods

Male Wistar rats (weight 400-600 g) were used for this study. Anaesthesia was induced with pentobarbital (IM injection of 0,8 ml/kg) and maintained using halothane (1%). Fur on one thigh was first cut and then further removed with hair remover to obtain good contact between skin and water, thus improving the transmission of ultrasound into the tissue. The rat was positioned so that the FUS focal point was approximately 5 mm into the tissue.

MR thermometry experiments were performed using a 4.7 T Bruker Biospec animal instrument with 120 mm shielded gradient insert. MR imaging was performed as was previously described in chapter 5, with a temporal resolution that was generally better than 1 sec, in-plane spatial resolution was typically $1 \times 1$ mm$^2$. The setup in which the animals were placed was previously described in chapter 5, in which also the specifications of the FUS transducer are given. On-line data processing was done using IDL (RSI, Boulder, CO).

Different heating protocols were applied, with target temperatures which varied from 40°C to 65°C. Duration of hyperthermia was in the range from 30 to 180 sec. Temperature control was initially based on the control mechanisms described in chapter 7, whereas in more recent experiments the control software described in chapter 8 was used.

All animals were sacrificed 12 to 15 hours after the intervention. The treated leg was fixed in 10% formalin and thereafter sectioned for histologic examination. Sections were stained with hematoxylin, eosin, and saffron, and examined. Several slices, parallel to the MR imaging plane, approximately 4 mm apart, were analyzed. This means that histology was done in 3D, whereas MR was done in a single slice. Measurements with a morphometric microscope were performed to measure, in each of the acquired slices, the surface of the zone in which tissue necrosis had occurred. Tissue damage was classified by histo-pathologists according to four levels of tissue damage: Level 1, interstitial oedema; level 2, cellular oedema; level 3, intracytoplasmic lesions; and level 4, nuclear lesions. Tissue which was classified as either category 3 or 4 was considered an irreversible lesion, the surface of these regions in all of the slices was summed to obtain a value for the size of the lesion.

### 10.2.1 Thermal dose calculation and noise correction

On-line calculation of the applied thermal dose was based on the empirical equation that has been introduced by Sapareto and Dewey [1], Eq. 1.1:

$$\begin{aligned} t_{eq,T_r} &= \int_0^t R^{T_r - T(t)} dt \\ where: \ & R = 0.25 \ \ (T < 43°C) \\ & R = 0.50 \ \ (T > 43°C) \end{aligned} \tag{10.1}$$

where $t_{eq,T_r}$ is the equivalent time of exposure at a chosen reference temperature $T_r$ for a given temperature evolution in time $T(t)$. Based on this equation, the equivalent time $t_{eq,43}$ ($T_r$=43°C) was calculated for the experiments described here. A threshold of 240 min at 43°C was used for tissue necrosis, identical to previously described experiments in literature [13, 14].

Noise in MR temperature measurements is not negligible, and generally has a normal distribution. Since the relationship between temperature and thermal dose is non-linear (see Eq. 10.1), normally distributed noise in MR temperature data will lead to noise in the thermal dose estimates that does not have a normal distribution. Mathematical analysis shows that normally distributed noise in temperature data will on average lead to an overestimation of the applied thermal dose. This overestimation depends on the standard deviation ($\sigma$) in the temperature measurement only. If the standard deviation in temperature is known, the calculated thermal dose can be corrected:

$$t_{eq} = t_{eq,\sigma} \cdot e^{-0.5\sigma^2 ln^2(2)} \approx t_{eq,\sigma} \cdot e^{-0.24\sigma^2} \tag{10.2}$$

where $t_{eq}$ is the corrected equivalent time, and $t_{eq,\sigma}$ is the equivalent time calculated from Eq. 10.1, using temperature data with noise that has a normal distribution and a standard deviation $\sigma$ (in °C). Fig. 10.1 shows the average overestimation of the thermal dose as a function of the standard deviation in the temperature data. The figure shows that a significant error is made in the thermal dose calculation when noise in the temperature maps exceeds 1°C.

In the experiments described here, noise in the MR data was determined from the data acquired before the start of the heating experiment. Its standard deviation was subsequently applied to correct the thermal dose estimate.

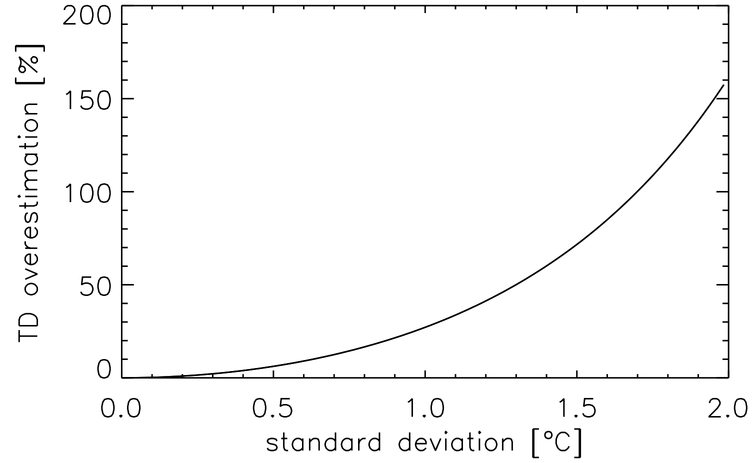

Figure 10.1: *Plot of average overestimation of thermal dose as a function of noise in MR temperature data. See text for more details.*

| Target temperature [°C] | Duration of hyperthermia [s] | Histologic necrosis[a] [mm$^2$] | Necrosis estimate (MRI) [mm$^2$] |
|---|---|---|---|
| 40 | 120 | 0.00 | 0.0 |
| 40 | 120 | 0.00 | 0.0 |
| 45 | 90 | 3.45 | 0.0 |
| 45 | 90 | 7.31 | 0.0 |
| 50 | 90 | 2.20 | 0.0 |
| 52 | 60 | 18.12 | 0.0 |
| 55 | 30 | 0.00 | 0.0 |
| 55 | 90 | 1.26 | 10.0 |
| 55 | 90 | 22.16 | 38.0 |
| 55 | 90 | 48.66 | 7.0 |
| 60 | 90 | 30.08 | 50.0 |
| 60 | 90 | 32.12 | 53.3 |
| 60 | 100 | 51.06 | 30.0 |

[a] The value given in this column is the sum of necrosis in all examined slices.

Table 10.1: *Results of various hyperthermia protocols applied to rat thigh muscle in vivo. Histological findings are compared to an on-line necrosis estimate, based on MR temperature data. Note that the temperature rise to target temperature is included in the duration.*

## 10.3 Results and discussion

Table 10.1 shows the results obtained upon application of different hyperthermia protocols, varying in maximal temperature and duration. The results obtained by histologic examination are compared to a necrosis estimate, which is based on Eq. 10.1, calculated from MR temperature data, corrected for noise in the temperature measurement. Standard deviation in the focal point voxel ranged from 0.33°C to 1.12°C (0.61°C on average), calculated over the temperature data acquired before the start of the heating procedure. Voxels where the calculated thermal dose exceeded an equivalent of 240 minutes at 43°C were labeled as necrosed. The surface given in the column with results based on MR data is the summed in-plane surface of all voxels that had been labeled during the experiment. The "surface" given in the column with histological data is the total area of the tissue-regions that were classified as either level 3 or 4 (see Materials and methods), summed over all slices. Multiple slices were studied, since spatial correlation between the MR data and histology was difficult to achieve. This was mainly due to tissue deformation between MR data-acquisition and preparation of slices, and the lack of adequate spatial markers.

On histologic examination, necrosed tissue was often well delineated, an oedematous border area could be identified (see also Fig. 7.4). Inflammatory changes appeared with the presence of leucocytes between treated and untreated areas. However, scattered spots of tissue necrosis surrounding the actual focal point lesion were found in histology. The size of these spots was inferior to the diameter of the FUS focal point. This effect was not predicted on the basis of thermal dose calculation, and scattering of the focal point beam was not observed using MR thermometry. This effect might be due to variations in the sensitivity of tissue for heat shock, or related to differences in local perfusion. The potential role of perfusion could not be reduced by fast thermometry, since the transducer used did not allow high temperature rises during short ultrasound pulses (a few seconds).

Over thirty animals were used in this study. Various animals were excluded from table 10.1 because of three reasons: (a) insufficient control of temperature with initial control mechanisms [9], an improved temperature control mechanism has been developed [10]; (b) problems with anesthesia; and (c) movements during thermometry, since on-line displacement correction was only recently implemented (see chapter 6).

A separate group of animals was treated using similar protocols, after which tissue necrosis was monitored several times over a period of 2-3 days using $T_1$-sensitive MR sequences. Gadolinium was injected intravenously to enhance contrast. The $T_1$-sensitized MR images, which had a spatial resolution comparable to the resolution of the MR temperature maps, showed a single, well-defined area of $T_1$-change (results not shown).

Table 10.1 indicates that, as was expected from experiments in literature, both a low maximal temperature (e.g. 40°C) as well as higher temperature for a short period of time (e.g. 55°C for 30 sec) did not induce tissue necrosis. This was predicted on the basis of MR thermometry, and confirmed using histology. Sixty-degree hyperthermia for 90 sec induced significant tissue necrosis in all cases.

## 10.4 Conclusion

Taking into account that histology was performed on the complete muscle (3D), whereas MR temperature mapping was limited to a single slice (2D), reasonable macroscopic agreement is found between MR-predicted necrosis and actual necrosis. However, this agreement appears to fail on a microscopic level. Although three-dimensional MR temperature imaging will allow better comparison of histology data and thermal dose calculation, small scattered spots of tissue necrosis cannot be predicted using this method. This is due not only to limitations in spatial resolution of MR temperature images, but probably due to variations in the sensitivity of tissue for heat shock. Development of a reliable method for on-line necrosis prediction based on MR data necessitates investigation of: (a) fast temperature rises to limit the role of perfusion; (b) different sensitivity of tissues to necrosis and apoptosis; and (c) recommendation for heating procedures.

## References

[1] S.A. Sapareto, W.C. Dewey, Thermal dose determination in cancer therapy. *Int. J. Radiation Oncology Biol. Phys.* **10**, 787-800 (1984)

[2] C. Damianou, K. Hynynen, The effect of various physical parameters on the size and the shape of necrosed tissue volume during ultrasound surgery. *J. Acoust. Soc. Amer.* **95**, 1641-1649 (1994)

[3] S.B. Field, Studies relevant to a means of quantifying the effect of hyperthermia. *Int. J. Hyperther.* **3**, 291-296 (1987)

[4] E.W. Gerner, Thermal dose and time-temperature factors for biological response to heat shock. *Int. J. Hyperther.* **3**, 319-327 (1987)

[5] G. Valancien, M. Harouni, B. Veillon, A. Mombet, D. Prapotnich, J.M. Brisset, J. Bougaran, Focused extracorporeal pyrotherapy: feasibility study in man. *J. Endourology* **6**, 173-180 (1992)

[6] A. Gelet, J.Y. Chapelon, R. Bouvier, R. Souchon, C. Pangaud, A.F. Abdelrahim, D. Cathignol, Treatment of prostate cancer with transrectal focused ultrasound: early clinical experience. *Eur. Urol.* **29**, 174-183 (1996)

[7] D. Coleman, F.L. Lizzi, J. Driller, A.L. Rosado, S. Ghang, T. Iwamoto, D. Rosenthal, Therapeutic ultrasound in the treatment of glaucoma. *Ophthalmology* **92**, 339-346 (1985)

[8] F.A. Jolesz, P.D. Jakab, Acoustic pressure wave generation within an MR imaging system: potential medical applications. *Magn. Res. Imag.* **1**, 609-613 (1991)

[9] F.C. Vimeux, J.A. de Zwart, J. Palussière, R. Fawaz, C. Delalande, P. Canioni, N. Grenier, C.T.W. Moonen, Real-time control of focused ultrasound heating based on rapid MR thermometry. *Invest. Radiol.* **34**, 190-193 (1999)

[10] R. Salomir, F.C. Vimeux, J.A. de Zwart, N. Grenier, C.T.W. Moonen, Hyperthermia by MR-guided focused ultrasound: accurate temperature control based on fast MRI and a physical model of local energy deposition and heat conduction. *Magn. Reson. Med.* **43**, 342-347 (2000)

[11] J.A. de Zwart, F.C. Vimeux, J. Palussière, C. Delalande, C.T.W. Moonen, Rapid MR temperature imaging for real-time visualization and control of focused ultrasound tissue heating. in "Proc., ISMRM, 7th annual meeting, Philadelphia, PA, USA, 1999", p. 401

[12] A.H. Chung, F.A. Jolesz, K. Hynynen, Thermal dosimetry of a focused ultrasound beam in vivo by magnetic resonance imaging. *Med. Phys.* **26**, 2017-2026 (1999)

[13] N. McDannold, K. Hynynen, D. Wolf, G. Wolf, F. Jolesz, MRI evaluation of thermal ablation of tumors with focused ultrasound. *J. Magn. Reson. Imaging* **8**, 91-100 (1998)

[14] H.E. Cline, K. Hynynen, C.J. Hardy, R.D. Watkins, J.F. Schenck, F.A. Jolesz, MR temperature mapping of focused ultrasound surgery. *Magn. Reson. Med.* **31**, 628-636 (1994)

# Part V

# Applications: Induction of Gene Therapy

# Chapter 11

# Induction of gene expression

## Contents

**11.1 Introduction** **135**

**11.2 Methods** **135**

**11.3 Results** **137**

  11.3.1 MRI/FUS 137

  11.3.2 Induction of hsp expression 137

**11.4 Discussion** **138**

David P. Madio, Peter van Gelderen, Daryl DesPres, Alan W. Olson, Jacco A. de Zwart, Timothy W. Fawcett, Nikki Holbrook, Myrna Mandel, Chrit T.W. Moonen
”On the feasibility of MRI-guided focused ultrasound for local induction of gene expression”
*Journal of Magnetic Resonance Imaging* **8**, 101-104 (1998)

## Abstract

Gene therapy is a promising approach to the treatment of many forms of disease, including cancer. Of critical concern in its implementation is the ability to control the location, duration, and level of expression of the therapeutic gene. Here, we propose the use of local heat in combination with a heat-sensitive promotor to help accomplish this. Certain members of the family of heat shock protein (hsp) promoters display a regulation that depends strongly on temperature. We present a study of natural hsp70 induction in rat leg by MRI-guided focused ultrasound to investigate the hsp70 promotor as possible candidate for use in control of gene expression with local heat. A temperature increase of 5-8°C in the focal region for 45 minutes led to a differential expression of the hsp70 mRNA between the focal region and the surrounding tissue ranging from a factor 3 to 67.

## 11.1 Introduction

A critical concern in gene therapy is controlling where, when, for how long, and at what level the exogenous gene will be expressed in the patient. One possible approach is to use a heat-inducible promotor to regulate expression based on local heating for a set interval.

Heat shock proteins (hsp) are found almost universally in living systems. They function to protect the organism against stress [1]. In mammalian systems, expression of some hsp is tightly coupled to temperature. In particular, the gene for the heat-inducible hsp70, under control of the hsp70 promotor, shows a very low constitutive expression and a strong induction on a temperature increase of only a few degrees [2]. This makes hsp70 a suitable candidate for targeting expression of a foreign gene for use in gene therapy.

Local temperature elevation by focused ultrasound (FUS) is already recognized to have medical benefits, for example, in tumor ablation. MRI can provide temperature images [3] for adjustment of FUS power levels and accurate focusing on the target location. Therefore, the MRI/FUS combination seems promising for tumor ablation [4] and, in this application, controlled heating for gene therapy using the hsp promotor.

This study investigates the feasibility of using MRI-guided FUS to control the expression of natural hsp70 spatially in rat leg muscle in vivo. Tissue samples at and near the focal point region are analyzed for the amount of hsp70 messenger ribonucleic acid (mRNA) present.

## 11.2 Methods

A polycarbonate rat holder was constructed that contained both the FUS transducer and an MR surface coil. The holder was placed in a fiberglass tube that was partially filled with water. The ultrasound passes through a 38-mm aperture in the platform supporting the animal. The holder was inclined to ensure that the rat hind leg was underwater while maintaining its head at a safe level above the water. The leg was supported by four 2-0 braided polyester fiber sutures forming a grid across the aperture. The FUS transducer was positioned so that the focus was 5 mm into the rat thigh. Transmitting the ultrasound directly through water to the leg was found to be more effective than other methods that used a combination of ultrasound gel and water contained in a balloon or condom. The FUS transducer (Specialty Engineering Associates, Soquel, CA) is 38 mm in diameter with a radius of curvature and nominal focal length of 25 mm. Its resonance frequency is 1.459 MHz. The predicted focal region, based on geometry and defined as the full-width-half-maximum intensity area [5], is an ellipsoid with a major axis of 6 mm oriented along the transducer axis and a minor axis of 1 mm. The radiofrequency (RF) surface coil was potted with epoxy in a 58-mm-diameter channel cut in the platform around the FUS aperture. Tuning and matching capacitors were housed out of the water above the rat.

Harlan Sprague-Dawley rats (*n*=6) with a mass of 428 ± 48 g were studied under an approved National Institutes of Health animal protocol. The relatively large size of the rats ensures that the focused ultrasound will focus deep within the biceps femoris muscle in the rat's right hind leg. Earlier tests with high intensity FUS performed on rats and on fresh chicken legs had indicated that focusing close to the skin may cause burns to the skin. The rat was anesthetized with an intraperitoneal administration of ketamine and xylazine. Three additional steps were taken to minimize the reflection and disruption of the ultrasound caused by acoustic impedance mismatches at interfaces. First, the right leg was shaved front and back with electric shears. Shaving also helped reduce potential sources of ribonucleic acid (RNA) degradation in the harvesting of the tissue. The skin was then cleaned with alcohol swabs and wet with a surfactant to reduce the retention of air microbubbles along the skin. Finally, after the rat had been immersed in water, large air bubbles under the leg were released. The rat was securely positioned on its right side on the platform, and care was taken to ensure that the focal region of the ultrasound was not close to any bones in the leg. Respiration was monitored to maintain a proper level of sedation. Body temperature was measured rectally with a pair of fiberoptic temperature probes (Luxtron Fluoroptic Model SMM, Santa Clara, CA). Another pair of probes monitored the temperature of the water bath. The bath temperature was controlled by heat exchange with a recirculating water heater. The target rectal temperature was 37 to 38°C. Deionized water was used for the bath because it was free of microbubbles that could interfere with the ultrasound.

Experiments were performed on a 4.7-T magnet controlled with an Inova console (Varian NMR Instruments, Palo Alto, CA). MR temperature mapping was performed using RF spoiled gradient echo imaging [6, 7]. The gradient echo data allowed phase difference maps to be reconstructed. The hydrogen nuclei in water demonstrate a temperature-dependent chemical shift that allows one to calculate temperature changes from these phase differences. TE and TR were 12 and 75 msec, respectively. Five slices with a thickness of 2 mm and a spacing of 3.5 mm were acquired sequentially in an interleaved fashion. They were initially centered around the nominal focal point; $128 \times 128$ maps were calculated for the $10 \times 10$ cm$^2$ field of view. Temperature resolution was approximately 0.15°C in vivo as determined from the SD in temperature of an unheated region in the rat leg distant from the region of heating. The results were in good agreement with what was reported by de Zwart et al [7].

An initial "cold" reference image was acquired after the rat was properly positioned in the magnet and its temperature was stabilized in the target range. This image was used to calculate the temperature changes in subsequent maps. Then, the ultrasound was turned on at low level ($\sim$ 1 W electric) just long enough to acquire a set of five slices. Data were exported to a Sun workstation (Sun Microsystems, Mountain View, CA), where user-written IDL code was used to construct temperature maps (see also ref. 7). From the maps, the focal point region was identified. If necessary, adjustments to the slice locations were made to center the focus in one slice. Heating of the leg muscle by continuous FUS then occurred for 45 minutes. Real-time temperature maps were used to keep the focal region elevated by 8°C at its center, giving approximately a 5°C rise at the edge of the region. Therefore, the focal region was heated to 42-45°C. Expression of the hsp70 gene continued for an additional 45 minutes after the heating period while MRI monitored the leg temperature. Throughout the experiment, the rat's core body temperature, as measured by the rectal probes, was maintained within 1° of the target range, and respiration was monitored to ensure proper anesthesia.

The rat was euthanized with pentobarbital and the right leg muscle was frozen using a freeze clamp cooled in liquid nitrogen (-196°C). The frozen sample was transported in a sterile specimen jar immersed in liquid nitrogen to a laboratory, where the tissue samples were prepared for analysis. The samples were taken from a $3 \times 3$ grid centered on the nominal axis of the FUS beam. The center sample was subdivided by depth into three, giving a total of 11 samples. The size of each muscle sample was approximately $4 \times 4 \times 2$ mm$^3$.

The samples were kept frozen until they were placed in Eppendorf tubes containing 0.5 ml of Trizol solution (Life Technologies, Gaithersburg, MD) and homogenized. The solution and homogenized tissue were then stored at -80°C until RNA was extracted. The RNA (30 $\mu$g of sample per lane) was separated by gel electrophoresis [8] and transferred to a nylon membrane. The integrity of the mRNA was assessed by visualization of the ethidium bromide-

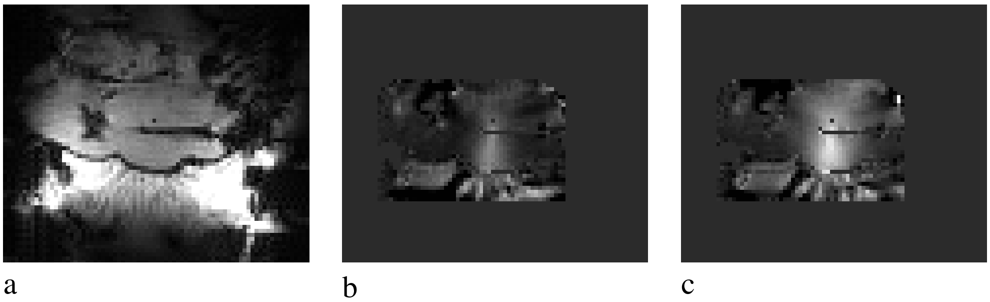

Figure 11.1: *(a) An intensity image of the rat leg in the focal plane showing, from bottom to top, the transducer (in part), the water bath with a high signal intensity (in the middle the inclined table with the aperture for FUS can be seen), and finally the rat leg. (b) Temperature change map for the same slice after 1 minute of heating. (c) Temperature change after 3 minutes of heating. Thermal diffusion is apparent. This state was maintained throughout the 45-minute heating interval. Temperature images were obtained during FUS application.*

stained RNA after transfer. The membranes were hybridized with a $^{32}$P-labeled cDNA that is complementary to the inducible hsp70 mRNA. Autoradiographs were created and analyzed for amount of inducible hsp70 in each sample.

## 11.3 Results

### 11.3.1 MRI/FUS

A special rat holder was constructed that incorporated the FUS transducer in a water bath, ensuring an uninterrupted pathway for the ultrasound. An intensity image of the slice containing the focal region is shown in Figure 11.1a. Figure 11.1b shows the temperature change in the same slice of the rat leg after 1 minute of heating. The field of view is identical to Figure 11.1a, but temperatures were calculated in a smaller region of interest only. In addition, pixels falling below a threshold intensity were not calculated because of poor signal-to-noise ratio and appear black. Based on Figure 11.1b, the size of the focal point region is approximately 4 mm parallel to the transducer plane and 8 mm along the transducer axis. This is affected by the properties of the transducer and diffusion and perfusion of the heated tissue. Figure 11.1c is a temperature map acquired after approximately 3 minutes of heating. Thermal diffusion is apparent, and subsequent data showed that an approximately steady state had been reached.

### 11.3.2 Induction of hsp expression

The induction of expression of hsp70 was analyzed with standard Northern blotting techniques. Figure 11.2 shows the Northern blot of total RNA prepared from rat thigh muscle after exposure to MRI-guided FUS and reacted with a random primed labeled human hsp70 stress inducible gene probe. The probe hybridizes strongly in lane 5 at a position of approximately 2.3 kb (Fig. 11.2, arrow), as expected for a 70,000-dalton protein. RNA loaded into lanes 8 and 11 was somewhat degraded. Measurements show that the differential expression of heat-inducible

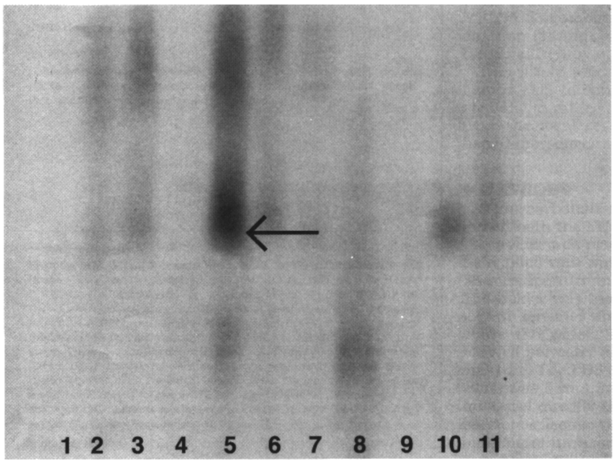

Figure 11.2: *Results of a Northern blot of locally heated rat leg. Lanes 5, 6, and 7 are of samples taken from the ultrasound focal region. Lane 5 shows markedly higher expression of RNA at approximately 2.3 kb (arrow). Differential expression between this sample and the surrounding samples ranges from a factor of 3 to 67.*

hsp70 in the focal region ranges from a factor of 3 to 67.

## 11.4 Discussion

This initial study has demonstrated that low level continuous FUS can be used to elevate the expression of endogenous hsp70 mRNA in vivo. The Northern blotting methods used here did not permit a distinction between the inducible and constitutive heat shock protein (generally indicated as hsp70 and hsc70, respectively). Therefore, the results shown here only give a lower limit of the differential induction of hsp70. Further studies are planned using distinction between hsp70 and hsc70 based on monoclonal antibodies. These preliminary studies demonstrate that the hsp70 promotor is a suitable target for use in control of foreign gene expression based on local heat. Such a system could be useful for a large variety of genes. One of our first objectives will be the local control of lymphokine production such as the tumor necrosis factor alpha (TNF$\alpha$). Despite the high efficiency of TNF$\alpha$ in murine tumors, systematic application in humans has been severely hampered by the high toxicity [9]. Therefore, controlled local production of TNF$\alpha$ seems to be a promising approach. The current study also shows that MRI can provide interactive temperature maps for monitoring local heating of in vivo tissue by FUS. In addition, incorporation of three-dimensional fast imaging methods such as PRESTO should allow for faster temperature maps [7].

## Acknowledgements

The authors thank Scott Chesnick for his assistance in the design and construction of the rat holder with incorporated ultrasound and RF surface coil.

# References

[1] H.J. Yost, R.B. Petersen, S. Lindquist, RNA metabolism: strategies for regulation in heat shock response. *Trends Genet.* **6**, 223-227 (1990)

[2] R. Voellmy, Transduction of the stress signal and mechanisms of transcriptional regulation of heat shock/stress protein gene expression in higher eukaryotes. *Crit. Rev. Eukaryot. Gene Expr.* **4**, 357-401 (1994)

[3] D.L. Parker, V. Smith, P. Sheldon, L.E. Crooks, L. Fussell, Temperature distribution measurements in two-dimensional NMR imaging. *Med. Phys.* **10**, 321-325 (1983)

[4] F.A. Jolesz, P.D. Jakab, Acoustic pressure wave generation within an MR imaging system: potential medical applications. *Magn. Reson. Imaging* **1**, 609-613 (1991)

[5] J.C. Bamber, M. Tristam, Diagnostic ultrasound. In: S. Webb, ed. "The physics of medical imaging." Bristol: Adam Hilger, 328-334 (1988)

[6] J. de Poorter, C. de Wagter, Y. de Deene, C. Thomsen, F. Ståhlberg, E. Achten, Noninvasive MRI thermometry with the proton resonance frequency (PRF) method: in vivo results in human muscle. *Magn. reson. Med.* **33**, 74-81 (1995)

[7] J.A. de Zwart, P. van Gelderen, D.J. Kelly, C.T.W. Moonen, Fast magnetic-resonance temperature imaging. *J. Magn. Reson. B* **112**, 86-90 (1996)

[8] J. Sambrook, E.F. Fritsch, T. Maniatis, Molecular cloning, a laboratory manual. 2nd ed. New York: Cold Spring Harbor (1989)

[9] M. Blick, S.A. Sherwin, M. Rosenblum, J. Gutterman, Phase I study of recombinant tumor necrosis factor in cancer patients. *Cancer Res.* **147**, 2986-2989 (1987)

# Chapter 12

# Induction of Localized Exogenous Gene Expression In Vivo

## Contents

**12.1 Introduction** **142**

**12.2 Materials and methods** **142**

- 12.2.1 Gene construct 142
- 12.2.2 Hyperthermia experiments 142
- 12.2.3 Analysis of tumor samples 143

**12.3 Results and discussion** **144**

- 12.3.1 Immuno-deficient mice 144
- 12.3.2 Induction of gene expression in the rat 145

**12.4 Conclusion** **147**

## 12.1 Introduction

In the previous chapter, the feasibility of induction of endogenous hsp using focused ultrasound has been demonstrated. In addition, in vitro experiments performed in our laboratory have demonstrated that the induction of the expression of an exogenous gene under control of a heat sensitive promoter in cells in culture is possible. These experiments were performed using an hsp-GFP gene construct (gene for green fluorescent protein under control of the minimal human hsp70-promoter), which was inserted in the genome of the C6-tumor cell line (stable transfection). Different heat shock protocols, varying in both temperature and duration, were applied in vitro [2]. Results are summarized in Fig. 12.1 (data taken from reference 2). In this chapter, the same modified cell line is used for preliminary in vivo MRI/FUS heating experiments. There experiments were carried out to demonstrate feasibility of local induction of GFP-expression in vivo upon FUS application [3]. FUS is applied under control of MR thermometry to achieve the desired temperature trajectory.

## 12.2 Materials and methods

### 12.2.1 Gene construct

EGFP, green fluorescent protein, was chosen as a reporter gene. The minimal human hsp70-promoter [5] (see Fig. 1.1b), where the major part of the regulating sequences was excluded, but the heat shock elements were conserved, was taken from the plasmid pD3SX (Stressgen Biotechnologies Corp., Victoria, BC, Canada). Under experimental conditions described here, this promoter was therefore only heat-regulated. The EGFP-gene was obtained from plasmid pEGFP-N1 (Clontech Laboratories, Palo Alto, CA). A rat glioblastoma-derived C6 tumor cell line [6] was used, in which the gene construct was implemented. Expression of this gene can be evaluated by measuring fluorescence of GFP [4]. For more details see ref. 2.

Tumor cells were implanted in immuno-deficient mice and wistar rats. In case of immuno-deficient mice (RAG2 $C^{-/-}/\gamma C^{-}$), approximately $15\times10^6$ cells were injected subcutaneously at the top of the shoulder [2]. In experiments performed using male Wistar rats ($n = 10$, weight approximately 150 g), the tumor was implanted subcutaneously in the thigh (approximately $4\times10^7$ cells).

After two weeks, the subcutaneous tumor reached a volume of 2-3 ml. Local hyperthermia was then applied. The animals were sacrificed 24 hours after the intervention.

### 12.2.2 Hyperthermia experiments

Hyperthermia experiments were performed on a 4.7T Bruker Biospec animal MR instrument with 12 cm gradient insert, using the setup described earlier [1]. Typical scan parameters for mouse experiments were: FLASH; 80 msec TR; 10 msec TE; $64 \times 60$ matrix; $64 \times 60$ mm$^2$ FOV; 5 mm slice-thickness; and 370 dynamic scans. For in vivo experiments on rats, scan parameters were: 16 msec TR; 10 msec TE; 384 dynamic scans; $64 \times 64$ matrix; 3 mm slice thickness; $64 \times 64$ mm$^2$ FOV, resulting in voxels of $1 \times 1 \times 3$ mm$^3$; and lipid suppression (see chapter 5), $\tau = 2236$ $\mu$sec. In all cases, localized shimming of the target zone was performed on the basis of phase information in a 3D gradient echo sequence (see chapter 5 for more details).

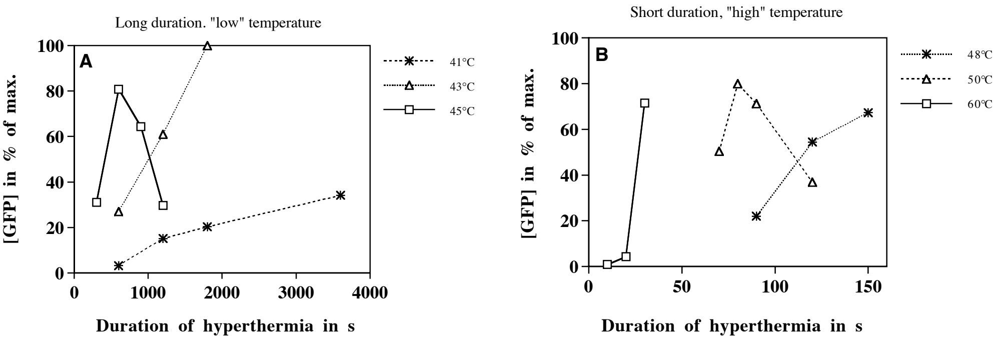

a b

Figure 12.1: *GFP expression, estimated by flow cytometry 24 hours after heat shock for different heat shock conditions. GFP-levels were normalized to the maximally observed level. Tubes with cell suspension were placed in a water bath at constant temperature. The results represent the mean of three independent experiments. a) Low temperature heat shock at waterbath temperatures of 41°C, 43°C and 45°C, respectively. b) High temperature heat shock at waterbath temperatures of 48°C, 50°C and 60°C, where final test tube temperature was 48°C in all three cases. Note that final temperature was reached faster for higher bath temperatures (data obtained from ref. 2)*

In mouse-experiments, hyperthermia was applied for 25 minutes, with a targeted temperature rise to 44°C, temperature was controlled using the mechanisms described in chapter 7. In rat-experiments, the duration of hyperthermia was 230 sec (50 sec rise to target temperature, followed by 180 sec constant temperature, see chapter 8) in all cases. Target temperature was varied, ranging from 42°C to 50°C, and was controlled using the control software described in chapter 8. The setup in which the animals were placed and the characteristics of the FUS transducer used are described in chapter 5.

### 12.2.3 Analysis of tumor samples

Protein expression in mouse tumors was determined using western blotting. Cells in tumor slices were lysed in Tris-HCl (10 mM, pH = 8)-triton-X-100 (0.3%), and the resulting solution was treated with DNAse I (Sigma, France). Proteins were then fractionated on 12% SDS-PAGE mini-gels, and alternatively stained or transferred on Immobilon P membranes (Bio-Rad, France). Anti-GFP or anti-hsp70 antibodies (Vector Laboratories, Inc., Burlingame, CA) were used for labeling, detection was performed using chemiluminescence blotting substrate (Boehringer Mannheim, Germany). Analysis is described in more detail in ref. 2.

Slices with a thickness of approximately 5-10 $\mu$m were collected in various locations in the subcutaneous rat-thigh tumors. In each of these locations, three consecutive slices were analyzed differently to label for respectively glial fibilary acidic protein (GFAP, specifically expressed by mature astrocytes and the C6 cell line), endogenous hsp and exogenous GFP. This was performed by immunohistochemistry.

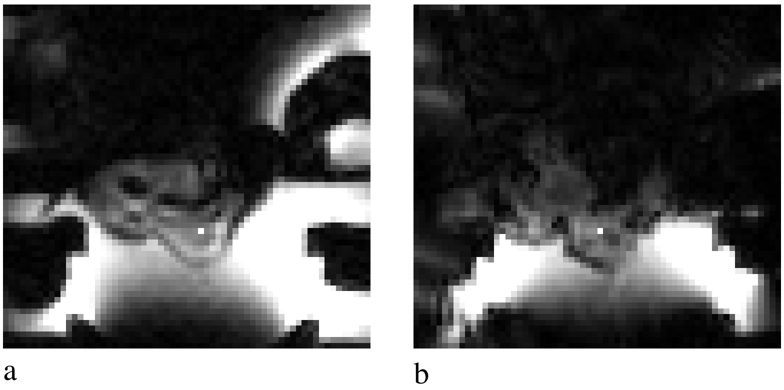

Figure 12.2: *$T_2^*$-weighted images through a C6 glioma tumor containing a gene construct with expression of GFP under control of a human hsp70-promoter. The focal point voxel is shown in white. a) Transverse scan plane, the plane in which temperature was measured. b) Sagittal scan plane.*

## 12.3 Results and discussion

### 12.3.1 Immuno-deficient mice

The focal point location inside the tumor on one of the immuno-deficient mice is shown in Fig. 12.2. The bright area in the lower part of the image represents the water in the reservoir. The mouse is located in the middle of the image. The animal was placed on its back, with the tumor placed directly in the path of the ultrasound beam. The location of the focal point during the heating experiment is indicated with a bright white spot (artificial, no increased signal intensity), just above the center of the tumor. Fig. 12.2a shows the focal point location with respect to the transverse scan plane through the focal point (read-out along the horizontal axis) in which temperature was monitored. Fig. 12.2b shows the perpendicular sagittal scan plane through the focal point.

Fig. 12.3 shows the measured focal point temperature trajectory during localized hyperthermia in the same animal. Reference temperature, measured using a thermocouple (endorectal), was 34.1°C. Temperature during FUS heating was controlled as was described in chapter 7. The target temperature was kept constant for 25 minutes. The standard deviation in focal point temperature between 200 and 1600 sec into the experiment was 0.58°C.

Fig. 12.4a shows a temperature profile parallel to the transducer plane, taken from a transverse temperature map acquired approximately 1630 sec into the experiment, just before the end of FUS application. Twenty-four hours after treatment, the tumor was dissected. The tumor was cut into 6 slices, perpendicular to both the imaging and the transducer plane, as is shown in Fig. 12.4b. The lower part of Fig. 12.4b shows the result of western blot analysis of the slices, showing both the amount of GFP and hsp found.

Note that a preliminary version of the control software was used for control of the hyperthermia procedure. In this software, the focal point position was determined before the start of the experiment, using a pilot experiment in which a 3-4°C temperature rise was applied to detect the focal point (see chapter 7). During the actual hyperthermia procedure, FUS control

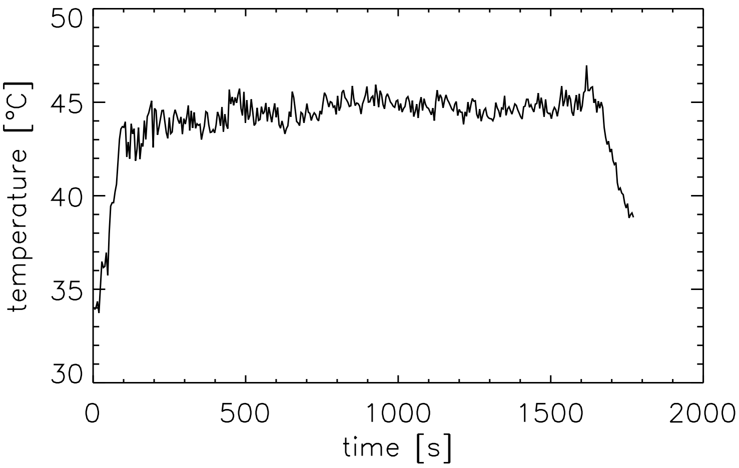

Figure 12.3: *Focal point temperature evolution during FUS heating of a subcutaneous tumor, implanted on the back of an immuno-deficient mouse. The focal point location within the tumor is shown in Fig. 12.2.*

was performed on the basis of the temperature in the focal point voxel found in the pilot experiment only. During the 25-minute heating experiment described here, the focal point had shifted approximately 2 mm in the plane of the FUS transducer (determined using post-processing of the MR data). The focal point found with the pilot experiment was possibly incorrect (for example due to noise in the MR measurement), also the FUS focal point might have shifted due to hyperthermia-induced changes in tissue composition, although such a shift occurs generally in the direction perpendicular to the transducer (see chapter 3).

The presence of higher temperature away from the "focal point" used for FUS control can be seen in Fig. 12.4a, where the maximal temperature in the profile exceeds the "focal point" temperature shown in Fig. 12.3 by approximately 2°C. In more recent versions of the control software, the location of the hottest voxel is determined from each new temperature map, using the coordinates of the hottest voxel.

### 12.3.2 Induction of gene expression in the rat

Fig. 12.5a shows the location of the focal point within the tumor of a rat that was subject to hyperthermia at 42°C. The transverse, $T_2^*$-weighted intensity image was acquired in the slice in which temperature was monitored. The tumor appears as a small bump in the center of the image, showing little contrast with healthy thigh-muscle tissue (above the tumor in the image). In the lower part of the image the FUS transducer can be seen (dark area), as well as the water in the reservoir (high signal intensity area between transducer and animal).

The focal point temperature trajectory in the same animal is shown in Fig. 12.5b. Reference temperature was 34.4°C, measured using a thermocouple. Measured data are depicted on top of the desired temperature evolution in time, which was determined before the start of the experiment. After a 60-sec period of gradual temperature rise, started 10 sec after the start of MR data acquisition, the target temperature was kept constant for 180 sec. FUS was controlled

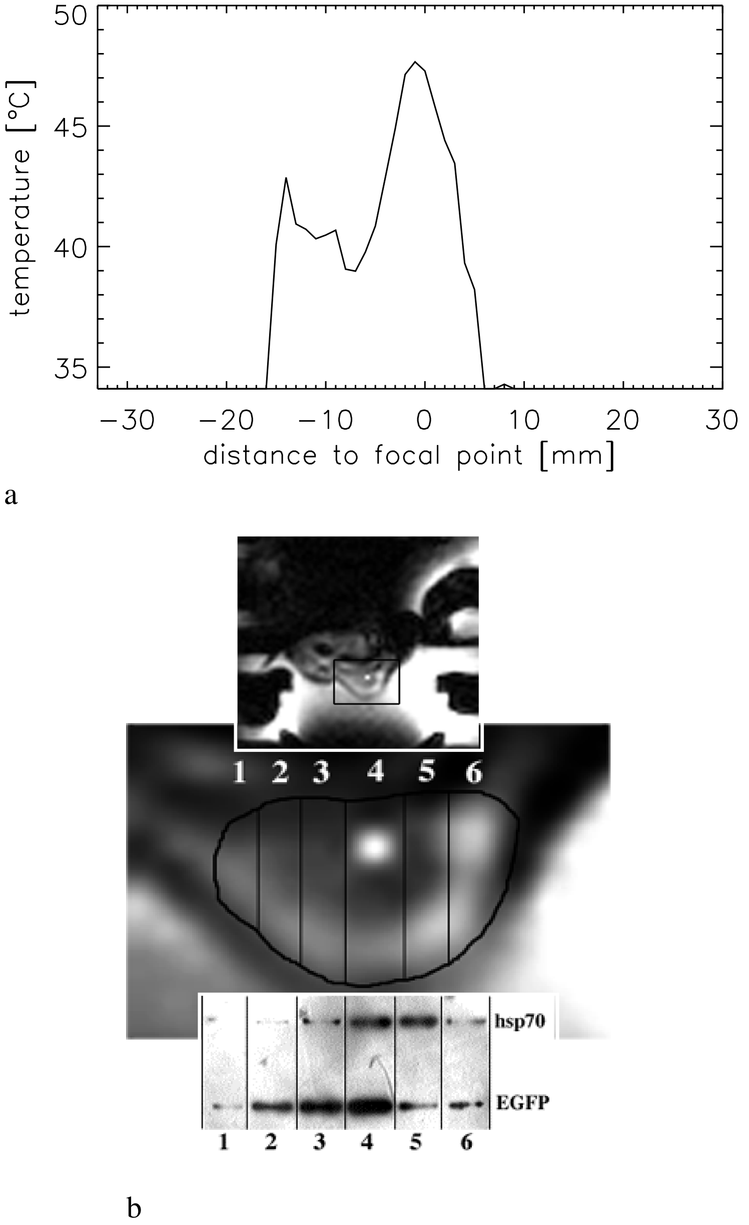

Figure 12.4: *a) Temperature profile through focal point, parallel to transducer, after 1620 sec of FUS heating. b) Composite image showing the orientation of six tumor slices that were analyzed using western blotting. The location of the six slices with respect to the MR image shown in Fig. 12.2a is indicated.*

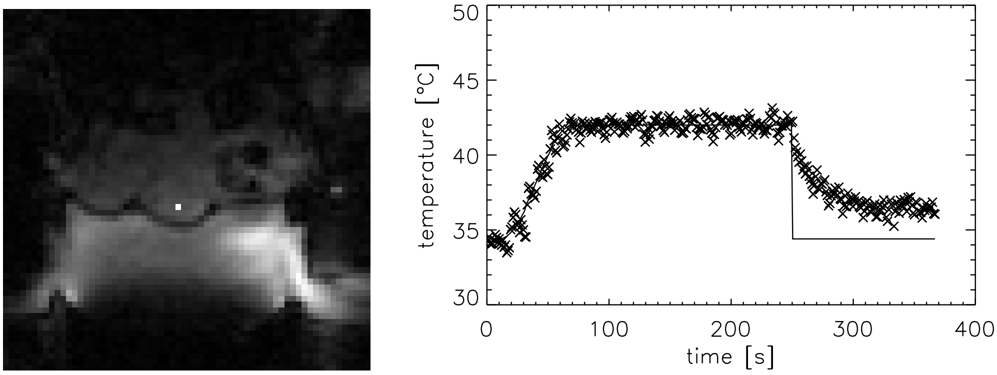

a b

Figure 12.5: *a) Focal point location within a subcutaneous tumor on the thigh of a male Wistar rat. b) Measured focal point temperature (×), superimposed on the pre-defined desired focal point temperature evolution (solid line).*

using the control mechanism described in chapter 8. The average temperature in the constant part of the heating curve (between 74 and 240 sec after the start of the experiment) was 42.0°C, with a standard deviation of 0.44°C. For the same voxel, the standard deviation in the measured temperature before FUS application was 0.23°C (determined over the first 10 temperature maps, before the start of FUS heating).

Animals were sacrificed 12-16 hours after hyperthermia, and the tumors removed. Slices showing the resulting GFAP-, hsp70- and GFP-expression after hyperthermia at 42°, 44° and 50°C are shown in the figures 12.6, 12.7, and 12.8, respectively. The top image in all three figures shows GFAP-expression, the center image a map of hsp-expression, and the bottom image the detected GFP.

In all three tumors, the C6-glioma cells, containing the gene construct, can bee seen to be more or less evenly distributed over the tumor, judging from the respective GFAP-maps (top images, C6-cells show in dark-blue). Following hyperthermia at 42°C, no significant hsp- and GFP-expression is found. After heat-shock at 44°C, hsp- and GFP-expression are found in a certain region of the tumor, showing up as a C-shaped area in the middle of the images given in Fig. 12.7. Finally, after hyperthermia at 50°C, significant hsp-expression can be seen throughout the central area of the image, while GFP-positive cells are found all over the image.

## 12.4 Conclusion

The experiments demonstrate that the induction of exogenous gene expression under control of a heat-sensitive, minimal hsp70-promoter is feasible in vivo using FUS under MR control. Experiments performed at different temperatures indicate that a certain threshold should be exceeded to induce significant expression of the exogenous gene. Additional studies are needed to investigate spatial distribution of GFP with respect to the FUS focal point, together with a better understanding of the relationship between temperature, time of exposure and the distribution of induced gene expression.

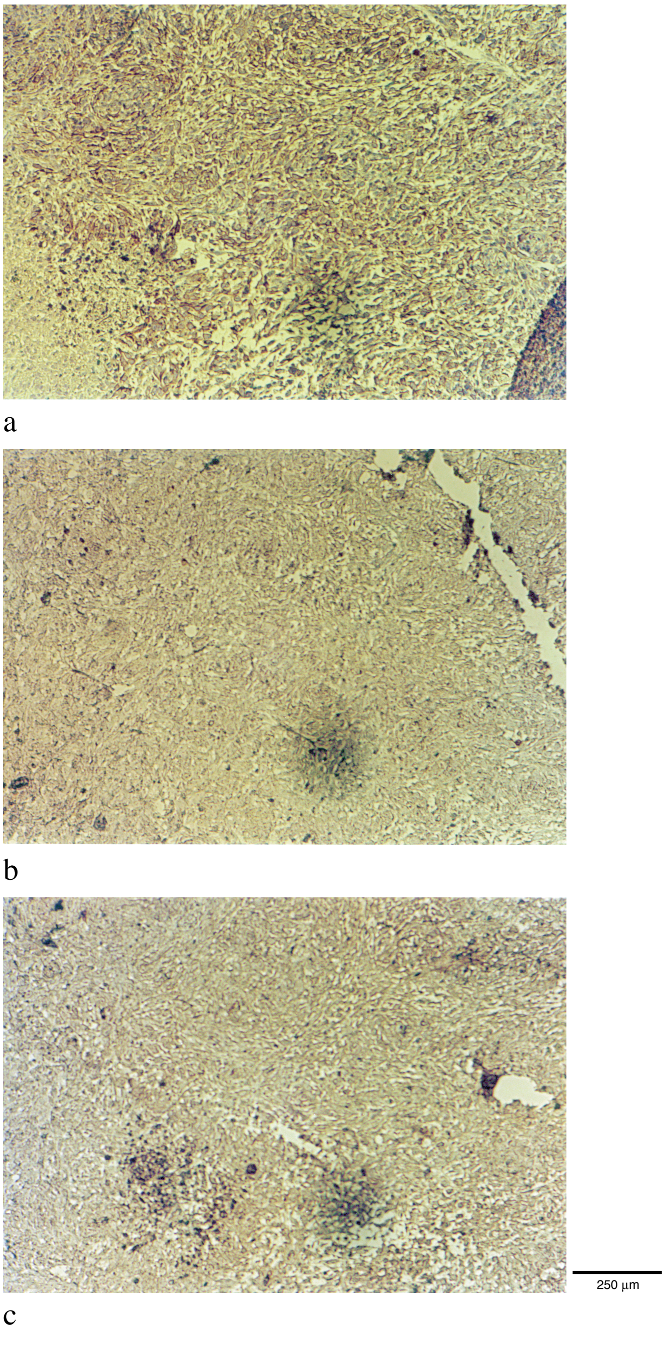

Figure 12.6: *Expression maps after 42°C hyperthermia for 3 min: (a) GFAP; (b) hsp70; (c) GFP. For more details see text. Note that the shadow just right of the center in the lower part of the images is an artifact.*

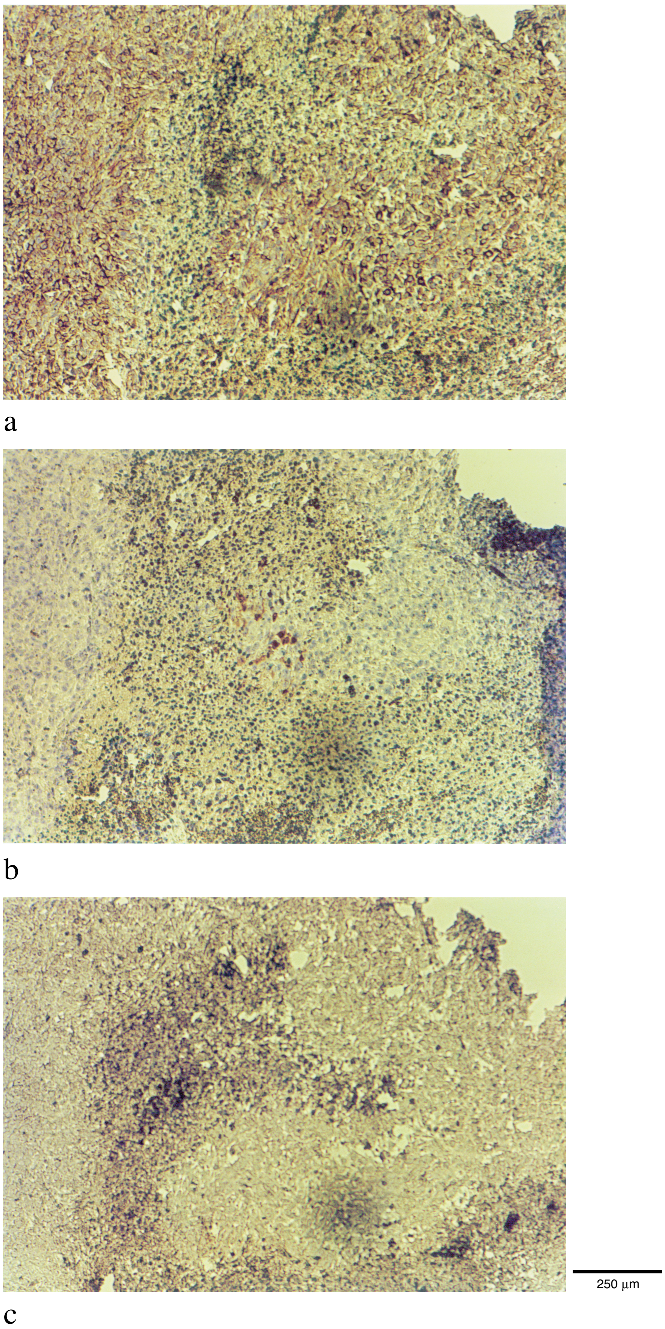

Figure 12.7: *Expression maps after 44°C hyperthermia for 3 min: (a) GFAP; (b) hsp70; (c) GFP. For more details see text. Note that the shadow just right of the center in the lower part of the images is an artifact.*

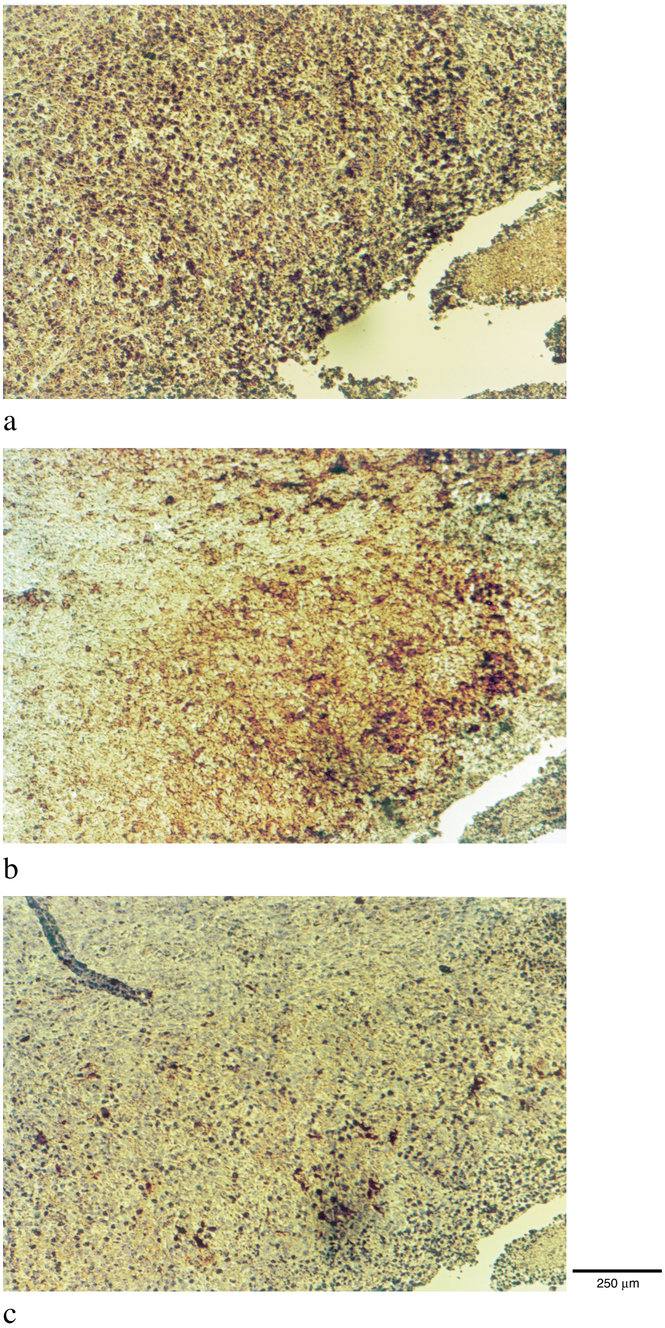

Figure 12.8: *Expression maps after 50°C hyperthermia for 3 min: (a) GFAP; (b) hsp70; (c) GFP. For more details see text. Note that the shadow just right of the center in the lower part of the images is an artifact.*

## References

[1] D.P. Madio, P. van Gelderen, D. DesPres, A. Olson, J.A. de Zwart, T.W. Fawcett, N.J. Holbrook, M. Mandel, C.T.W. Moonen, On the feasibility of MRI-guided focused ultrasound for local induction of gene expression. *J. Magn. Res. Imaging* **8**, 101-104 (1998)

[2] A. Vekris, C. Maurange, C. Moonen, F. Mazurier, H. De Verneuil, P. Canioni, P. Voisin, Control of transgene expression using local hyperthermia in combination with a heat-sensitive promoter. *J. Gene Medicine*, [in press]

[3] C. Moonen, A. Vekris, P. Voisin, J. de Zwart, C. Maurange, F. Vimeux, P. Canioni, Spatial and temporal control of transgene expression with heat-sensitive promoter and MRI guided focused ultrasound, in "Proc., ISMRM, 7th annual meeting, Philadelphia, PA, USA, 1999", 402

[4] T. Misteli, D. Spector, Applications of the green fluorescent protein in cell biology and biotechnology. *Nature Biotechnology* **15**, 961-963 (1997)

[5] R. Voellmy, Transduction of the stress signal mechanisms of transcriptional regulation of heat shock/stress protein gene expression in higher eukaryotes. *Critical Reviews in Eukaryotic Gene Expression* **4(4)**, 357-401 (1994)

[6] P. Benda, J. Lightbody, G. Sato, L. Levine, W. Sweet, Differentiated rat glial cell strain in tissue culture. *Science* **161**, 370-371 (1968)

# Part VI

# Applications: Local Drug Delivery

# Chapter 13

# Thermo-sensitive liposomes for local drug delivery

## Contents

**13.1 Introduction** **156**

**13.2 Materials and methods** **156**

**13.3 Results and discussion** **157**

**13.4 Conclusions** **158**

Adapted from:
Jacco A. de Zwart, Rares Salomir, Frédéric Vimeux, Jo Klaveness, Chrit T.W. Moonen
”On the feasibility of local drug delivery using thermo-sensitive liposomes and MR-guided focused ultrasound”
ISMRM, 8th scientific meeting and exhibition, Denver, CO, USA, April 1-7, 2000, p. 43

## 13.1 Introduction

Two decades ago, Weinstein et al. proposed the use of liposomes in combination with local hyperthermia for drug delivery [1]. The method exploits the characteristic of lipid bilayer membranes to become "leaky" when they pass through their liquid-cristalline transition temperature ($T_c$). This is a property which depends on the phospholipid-composition of the bilayer membrane. At temperatures well below their $T_c$, liposomes are relatively stable, but as $T_c$ is approached the phase transition of its membrane renders them "leaky" for small molecules. Liposomes with a $T_c$ a few degrees above body temperature can therefore be used for local drug delivery if the target zone is locally heated.

Focused ultrasound appears a good candidate for the induction of drug release from thermosensitive liposomes. FUS non-invasively heats tissue locally. Under control of magnetic resonance imaging, it allows well controlled local heat deposit [2], thus providing the required spatial and temporal control of tissue temperature. Application of FUS-MRI to tissue ablation [3] and localized gene therapy [4] is currently under investigation. Here, the feasibility of local release of gadolinium from thermosensitive liposomes using FUS-MRI is demonstrated.

## 13.2 Materials and methods

Gadolinium diethylenetriamine penta-acetic acid bis(methylamide) (GdDTPA-BMA) was encapsulated in liposomes, consisting of a phospholipid blend of 95% (w/w) dipalmitoylphosphatidylcholine (DPPC) and 5% dipalmitoylphosphatidylglycerol (DPPG). Liposome preparation was done using a protocol similar to the one described in ref. 5. The liposomes have a 42°C $T_c$ and were uniformly incorporated in a hardening agarose gel at temperatures well below liposome-$T_c$. The gel was placed in the FUS setup developed for in vivo experiments on rat thigh [6].

MR experiments were performed on a 4.7 T Bruker Biospec animal instrument. After positioning of the sample in the isocenter of the 120 mm shielded gradient insert, localized shimming was applied, based on phase information in a predefined volume of interest, repetitively measured using a fast 3D gradient-echo sequence [6]. A multi-shot echo-planar imaging (MS-EPI) sequence was modified for inversion recovery (IR) imaging. A hyperbolic secant adiabatic prepulse pulse [7] preceded the standard three-lobed sinc-pulse, the pulses were separated by an inversion recovery delay. Initially, multiple experiments with different inversion recovery delays were performed to determine the $T_1$ of the liposome-containing gel. Thereafter, FUS heating was applied, monitored on-line using MR thermometry [8].

Thermometry data were acquired using: FLASH; $64 \times 64$ matrix; $80 \times 80$ mm$^2$ field-of-view; 20 msec TR; 8 msec TE; 384 dynamic scans; and 1280 msec imaging time. Constant amplitude FUS heating was applied (approximately 11.4 W electrical power for the experiment with rise to 42°C), FUS was manually started approximately 20 sec after the start of the MR data acquisition, and interrupted when target temperature was reached. Heating experiments were performed with target temperatures of 32 and 42°C, respectively below and at liposome $T_c$.

Gadolinium release from the liposomes was demonstrated using an inversion recovery multi-shot gradient-echo EPI sequence (3 lines/TR): 147 sec imaging time; $64 \times 63$ matrix; $64 \times 64$ mm$^2$ field-of-view; and 1150 msec IR-time (corresponding to the zero-crossing of non-heated gel). IR-maps were acquired before FUS heating and after each FUS heating procedure to

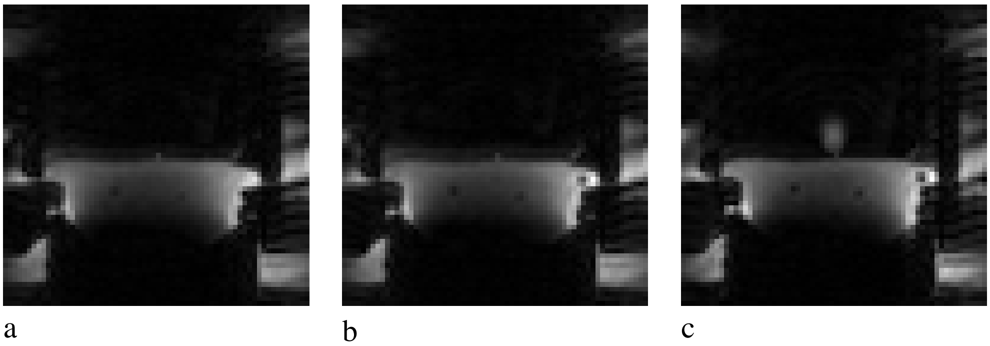

Figure 13.1: *Inversion recovery maps of gel containing gadolinium encapsulated in liposomes with a phase transition temperature of 42°C. The bottom half of the images represents the FUS transducer, immersed in water (visible as a bright region below the center of the image), the top half the agarose gel. The inversion recovery time used to acquire all three images was 1150 msec. (a) Reference map, acquired before FUS heating. (b) IR-map acquired after FUS heating to 32°C and successive cooling. (c) IR-map acquired 15 minutes after FUS heating to approximately 42°C. Local, FUS-induced gadolinium release shows as a bright region in the center of the image.*

detect changes in $T_1$-relaxation time due to gadolinium release. A 15-minute cooling period was implemented after each heating cycle before $T_1$-weighted imaging to reestablish reference temperature in the FUS focal region.

## 13.3 Results and discussion

Fig. 13.1a shows an MS-EPI inversion recovery image, acquired with an IR-time of 1150 msec before FUS heating (reference image). The dark region in the lower part of the image represents the FUS transducer, the bright region just below the center the water in the reservoir, the dark region in the top half of the image the agarose gel. Gel-signal can be seen to be suppressed equally.

The bottom curve in Fig. 13.2 shows the focal point temperature-time trajectory during a FUS heating experiment conducted to investigate the influence of FUS on liposome stability. The maximally achieved temperature of 32°C is well below liposome-$T_c$, no temperature-induced gadolinium release is to be expected. The corresponding IR-map, acquired after a 15-minute cooling period, is shown in Fig. 13.1b. No signal changes could be observed, indicating that no gadolinium release occurred in the FUS focal point region during heating, suggesting that liposomes are not disturbed by ultrasound pressure waves [9].

Heating the gel to approximately 42°C did invoke local release of gadolinium in the FUS focal point region, as can be seen from Fig. 13.1c, acquired 15 minutes after the FUS heating experiment. The region around the FUS focal point, just above the center of the image, shows significant signal increase, indicating a local decrease of $T_1$ due to release of gadolinium from the liposomes. The focal point temperature trajectory, used to induce this release, is shown in Fig. 13.2.

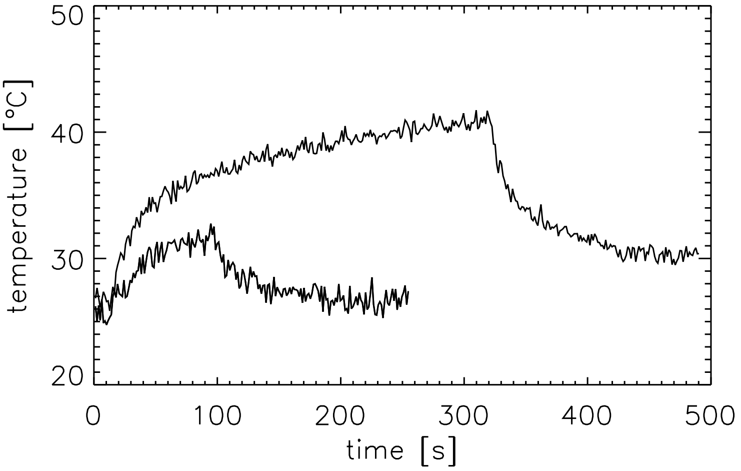

Figure 13.2: *Focal point temperature trajectory during experiment with 32°C target temperature, well below liposome $T_c$ (lower curve), and focal point temperature trajectory applied to induce local release of gadolinium from liposomes (top curve). Constant-power FUS was applied manually.*

## 13.4 Conclusions

The preliminary experiments described here demonstrate that MR-controlled focused ultrasound heating to temperatures a few degrees above body temperature allows controlled local release of agents from temperature sensitive liposomes.

## References

[1] J.N. Weinstein, R.L. Magin, M.B. Yatvin, D.S. Zaharko, Liposomes and local hyperthermia: selective delivery of methotrexate to heated tumors. *Science* **204**, 188-191 (1979)

[2] R. Salomir, F.C. Vimeux, J.A. de Zwart, N. Grenier, C.T.W. Moonen, Hyperthermia by MR-guided focused ultrasound: accurate temperature control based on fast MRI and a physical model of local energy deposition and heat conduction. *Magn. Reson. Med.* **43**, 342-347 (2000)

[3] H.E. Cline, K. Hynynen, C.J. Hardy, R.D. Watkins, J.F. Schenck, F.A. Jolesz, MR temperature mapping of focused ultrasound surgery. *Magn. Reson. Med.* **31**, 628-636 (1994)

[4] D.P. Madio, P. van Gelderen, D. DesPres, A. Olson, J.A. de Zwart, T.W. Fawcett, N.J. Holbrook, M. Mandel, C.T.W. Moonen, On the feasibility of MRI-guided focused ultrasound for local induction of gene expression. *J. Magn. Res. Imaging* **8**, 101-104 (1998)

[5] S.L. Fossheim, A.K. Fahlvik, J. Klaveness, R.N. Muller, Paramagnetic liposomes as MRI contrast agents: influence of liposomal physicochemical properties on the in vitro relaxivity. *Magn. Reson. Imaging* **17**, 83-89 (1999)

[6] J.A. de Zwart, F.C. Vimeux, C. Delalande, P. Canioni, C.T.W. Moonen, Fast lipid suppressed MR temperature mapping with echo-shifted gradient echo imaging and spectral-spatial excitation. *Magn. Reson. Med.* **42**, 53-59 (1999)

[7] M.S. Silver, R.I. Joseph, C.H. Chen, V.J. Sank, D.I. Hoult, Selective population inversion in NMR. *Nature* **310**, 681-683 (1984)

[8] J.A. de Zwart, F.C. Vimeux, J. Palussière, Christophe Delalande, Chrit T.W. Moonen, Rapid MR temperature imaging for real-time visualization and control of focused ultrasound tissue heating. in "Proc., ISMRM, 7th annual meeting, Philadelphia, PA, USA, 1999", p. 401

[9] E.C. Unger, K. Ugurbil, R.E. Latchaw, Contrast agents for cerebral perfusion MR imaging. *J. Magn. Reson. Imaging* **4**, 829-836 (1994)

# Part VII

# Conclusion

# Chapter 14

# Concluding Discussion

## Contents

14.1 Temperature dependent magnetic susceptibility changes 165

14.2 Spatial and temporal resolution of temperature imaging 165

14.3 Phased-array FUS transducers 165

Throughout this thesis, the potential of PRF-based MR thermometry for the control of focused ultrasound during hyperthermia has been demonstrated. Improvements in speed and accuracy of MR thermometry have been discussed, precise control of the heating procedure has been demonstrated. However, some details merit further attention in anticipation of clinical feasibility studies. In this chapter, those issues are briefly discussed.

## 14.1 Temperature dependent magnetic susceptibility changes

In the introduction, the temperature dependence of the chemical shift of water protons is described (see Eq. 2.19), assuming that the magnetic susceptibility does not change with temperature. In the work described in this thesis, temperature dependent susceptibility changes have not been taken into account. In early work by Von Hermann the temperature dependence of water magnetic susceptibility was investigated [2]. Initial work on the influence of changes in volume susceptibility on PRF-based MR thermometry was performed by De Poorter [1]. In more recent work by Peters et al. [3], the influence of the spatial temperature distribution has been discussed. This work demonstrates that the apparent temperature dependence of the PRF is determined by the temperature distribution in the entire object, and its orientation with respect to the $B_0$-field. In recent work from our laboratory, a method for the on-line evaluation and correction of such temperature dependent susceptibility changes is proposed [4], which has yet to be tested in vivo.

## 14.2 Spatial and temporal resolution of temperature imaging

The temporal resolution of temperature mapping should mainly depend on the energy deposition to allow reliable control over the heating procedure. In addition, to provide sufficiently accurate volumetric temperature information, the spatial resolution of the thermometry method should be on the order of or better than the focal point dimensions (full-width half-max of the focal point), ideally of the order of the ultrasound wavelength.

During a hyperthermia intervention, dynamic changes in temperature occur only in the target area and surrounding tissue. Because of the way MR data are acquired however, the field-of-view used in the imaging experiment must cover the part of the object in the selected slice completely. Otherwise, regions of the object outside the field-of-view will “fold back” due to undersampling of the MR signal (Nyquist principle), although oversampling in the read-direction is generally employed to avoid this. As long as the fold-back does not cover the target region, this might be acceptable, otherwise sufficient data should be acquired to avoid such artifact at the cost of increased imaging time.

Selective excitation of spins in the target region appears to be a more elegant approach. Existing methods of selective excitation are however either rather time consuming, like 2D RF pulses [9], or exploit the formation of spin-echoes, as in LOLO-like sequences [8]. A recently proposed alternative to decrease of scan time are imaging techniques which exploit signal acquired using multiple parallel receiver coils, like the simultaneous acquisition of spatial harmonics (SMASH) [6] and sensitivity encoding (SENSE) [7] methods.

## 14.3 Phased-array FUS transducers

The principle of phased-array FUS transducers has been discussed shortly in the introduction. Phased-array FUS transducers allow focalization of the FUS beam even in an inhomogeneous object, since phase and amplitude of each element can be adjusted individually to obtain the desired focal point. For a large number of elements however, determination of the individual phase for each of the elements is complicated, although time-reversed acoustics appear to be the solution to this problem [10].

Recent work from our laboratory demonstrated that, when an object is moved in the vicinity of the target area, and its magnetic susceptibility differs from that of the surrounding medium, MR thermometry is affected [5]. The moving object (e.g. FUS transducer) causes a perturbation of the volume magnetic susceptibility in the target area, leading to errors in the calculated temperature maps. The effect of such a movement can be predicted and a correction can thus be applied [5]. However, the use of a fixed, phased-array FUS transducer would overcome the problem altogether.

## References

[1] J. De Poorter, Noninvasive MRI thermometry with the proton resonance frequency method: study of susceptibility effects. *Magn. Reson. Med.* **34**, 359-367 (1995)

[2] A. Von Hermann, Die absolute magnetische suszeptibilität des wassers und ihre temperaturabhängigkeit. *Ann. Physik* **18**, 593-612 (1933)

[3] R.D. Peters, R.S. Hinks, R.M. Henkelman, Heat-source orientation and geometry dependence in proton-resonance frequency shift magnetic resonance thermometry. *Magn. Reson. Med.* **41**, 909-918 (1999)

[4] R. Salomir, J.A. de Zwart, F.C. Vimeux, B. Quesson, C.T.W. Moonen, Temperature-induced changes in magnetic susceptibility in local hyperthermia: correction of MR thermometry. “ISMRM, 8th annual meeting, Denver, CO, USA, 2000”, p. 1349

[5] R. Salomir, B. Quesson, J.A. de Zwart, F.C. Vimeux, C.T.W. Moonen, MR guided focused ultrasound hyperthermia: $B_0$ field dynamic perturbation due to a moving transducer. “ISMRM, 8th annual meeting, Denver, CO, USA, 2000” p. 1360

[6] D.K. Sodickson, W.J. Manning, Simultaneous acquisition of spatial harmonics (SMASH): fast imaging with radiofrequency coil arrays. *Magn. Reson. Med.* **38**, 591-603 (1997)

[7] K.P. Pruessmann, M. Weiger, M.B. Scheidegger, P. Boesinger, SENSE: sensitivity encoding for fast MRI. *Magn. Reson. Med.* **42**, 952-962 (1999)

[8] J.B. Weaver, R.D. Harris, P.K. Spiegel, Limited field of view spin echo MR imaging. *Magn. Reson. Imag.* **9**, 389-394 (1991)

[9] J. Pauly, D. Nishimura, A. Macovski, A k-space analysis of small tip angle excitation. *J. Magn. Reson.* **81**, 43 (1989)

[10] M. Fink, Time reversed Acoustics. *Physics Today* **20**, 34-40 (1997)

# Part VIII

# Curriculum Vitae and Publications

# Curriculum Vitae

Jacobus Adrianus (Jacco) de Zwart was born in Rheden, the Netherlands, on September 26, 1971 as the elder son of Hendrikus de Zwart and Gerda Mensie Minkman - de Zwart.

After passing elementary school at “de Akker” in Dieren (NL) and pre-university education (VWO) at the “Baudartius College” in Zutphen (NL), Jacco started a study Molecular Sciences (Moleculaire Wetenschappen) at the Wageningen Agricultural University in the Netherlands in 1989. Even though his initial intension was to work in the molecular biology field, he graduated in 1995 with the specialization “Physical-Chemical” on the basis of three theses, all physics-oriented. The first discusses work performed on magnetic resonance diffusion and perfusion measurements (“Diffusie en Perfusiemetingen - PFG NMR & NMR Imaging”, department of Molecular Physics). The second thesis discusses his contribution to the development of a fluorescence lifetime imaging microscopy platform at the department of Biochemistry (“Time Resolved Imaging Microscopy in Wageningen”). Finally, a third thesis (“Fast MRI Thermometry”) concluded his six-month stay at the *In Vivo* NMR Research Center of the National Institutes of Health in Bethesda, Maryland, USA.

After graduation and a long summer vacation, during which he met his girlfriend, he returned to the NIH in the end of September 1995 to continue working on MR thermometry for six months.

In November 1996 he started his Ph.D.-research on the same topic at the department Résonance Magnétique des Systèmes Biologiques at Victor Segalen university in Bordeaux, France.

# Papers

Jacco A. de Zwart, Peter van Gelderen, Dan J. Kelly, Chrit T.W. Moonen, Ultra-fast Magnetic Resonance Temperature Imaging. *J. Magn. Reson. B* **112**, 86-90 (1996)

David P. Madio, Peter van Gelderen, Daryl DesPres, Alan W. Olson, Jacco A. de Zwart, Timothy W. Fawcett, Nikki J. Holbrook, Myrna Mandel, Chrit T.W. Moonen, On the Feasibility of MRI-Guided Focused Ultrasound for Local Induction of Gene Expression. *J. Magn. Res. Imaging* **8**, 101-104 (1998)

Frédéric C. Vimeux, Jacco A. de Zwart, Jean Palussière, Rabia Fawaz, Christophe Delalande, Paul Canioni, Nicolas Grenier, Chrit T.W. Moonen, Real-time control of focused ultrasound heating based on rapid MR thermometry. *Invest. Radiol.* **34**, 190-193 (1999)

Christophe Delalande, Jacco A. de Zwart, Hervé Trillaud, Nicolas Grenier, Chrit T.W. Moonen, An echo-shifted gradient echo MRI method for efficient diffusion weighting. *Magn. Reson. Med.* **41**, 1000-1008 (1999)

Jacco A. de Zwart, Frédéric C. Vimeux, Christophe Delalande, Paul Canioni, Chrit T.W. Moonen, Fast lipid-suppressed MR temperature mapping with echo-shifted gradient-echo imaging and spectral-spatial excitation. *Magn. Reson. Med.* **42**, 53-59 (1999)

Rares Salomir, Frédéric C. Vimeux, Jacco A. de Zwart, Nicolas Grenier, Chrit T.W. Moonen, Hyperthermia by MR-guided focused ultrasound: accurate temperature control based on fast MRI and a physical model of local energy deposition and heat conduction. *Magn. Reson. Med.* **43**, 342-347 (2000)

Jacco A. de Zwart, Frédéric C. Vimeux, Jean Palussière, Rares Salomir, Christophe Delalande, Chrit T.W. Moonen, Real-time correction and visualization of motion during MR-controlled FUS hyperthermia. *Magn. Reson. Med.* [submitted]

# Peer-Reviewed Abstracts

Jacco A. de Zwart, Peter van Gelderen, Dan J. Kelly, Chrit T.W. Moonen, Ultra fast MRI thermometry. “ISMRM, 4th scientific meeting and exhibition, New York, NY, USA”, 1750 (1996)

Jacco A. de Zwart, Christophe Delalande, Chrit T. W. Moonen, Combination of echo shifting with binomial pulse excitation for lipid suppressed MR temperature imaging. “ESMRMB 14th annual meeting, Brussels, Belgium”, 230 (1997)

Jacco A. de Zwart, Frédéric C. Vimeux, Christophe Delalande, Chrit T. W. Moonen, Fast lipid suppressed temperature mapping for the motinoring of focused ultrasound heated tissue. “ISMRM 6th scientific meeting and exhibition, Sydney, Australia”, 350 (1998)

Jacco A. de Zwart, Frédéric C. Vimeux, Christophe Delalande, Nicolas Grenier, Chrit T. W. Moonen, Control of focused ultrasound heating based on rapid MR thermometry and on-line data processing. “ISMRM 6th scientific meeting and exhibition, Sydney, Australia”, 694 (1998)

Jacco de Zwart, Frédéric Vimeux, Jean Palussière, Nicolas Grenier, Chrit Moonen, Monitorage de la température en temps réel par IRM. “Journées Françaises de Radiologie, Paris”, 1208 (1998)

Jacco A. de Zwart, Frédéric C. Vimeux, Jean Palussière, Christophe Delalande, Chrit T.W. Moonen, Rapid MR temperature imaging for real-time visualization and control of focused ultrasound tissue heating. “ISMRM, 7th scientific meeting and exhibition, Philadelphia, PA, USA”, 401 (1999)

Jacco A. de Zwart, Rares Salomir, Frédéric Vimeux, Jo Klaveness, Chrit T.W. Moonen, On the feasibility of local drug delivery using thermo-sensitive liposomes and MR-guided focused ultrasound “ISMRM, 8th scientific meeting and exhibition, Denver, CO, USA”, 43 (2000)

Jacco A. de Zwart, Frédéric C. Vimeux, Rares Salomir, Jean Palussière, Chrit T.W. Moonen, Real-time correction and visualization of motion during MR-controlled FUS hyperthermia. “3rd interventional MRI symposium, Leipzig, Germany”, P-58 (2000)

# Part IX

# Summaries

# Summary

This thesis describes developments in MR thermometry methodology and data handling, intended to increase speed and reliability of MR temperature imaging for the control and monitoring of hyperthermia interventions in vivo. Feasibility studies were performed to investigate the use of MR controlled hyperthermia for three potential medical applications: (a) thermal ablation of tissue, (b) local induction of the expression of genes under control of a heat-sensitive promotor, and (c) the induction of controlled local substance release from thermosensitive liposomes.

In the introduction, these three applications are described (chapter 1), followed by an introduction to MR temperature imaging (chapter 2) and focused ultrasound (FUS) (chapter 3), which is used to induce hyperthermia in the experiments described in this thesis.

MR thermometry can be based on the temperature dependence of the water proton resonance frequency (PRF). A shift in resonance frequency, resulting from temperature change, can be mapped using the phase information in RF-spoiled gradient-echo images. A reference image is used to compensate for other factors that contribute to image phase, like magnetic field homogeneity. For a given temperature rise, the measured phase difference increases linearly with the echo time (TE) of the experiment. However, the signal-to-noise ratio of the phase images decreases exponentially with time constant $T_2^*$. It can be derived that optimal temperature sensitivity exists when TE equals $T_2^*$. In conventional MR imaging, the TE is smaller than the repetition time (TR) of the experiment, a compromise between fast imaging (short TR) and optimal temperature sensitivity (relatively long TE, $\sim T_2^*$) is therefore necessary. Chapter 4 describes how echo shifting, which allows formation of gradient echoes one or more TR periods after signal excitation (thus: TE $>$ TR), can be employed for fast temperature imaging with a TE leading to optimal temperature sensitivity. Temperature measurements with a standard deviation of 0.1-0.2°C with an temporal resolution of 144 msec and a spatial resolution of 0.56 mm have been demonstrated using echo-shifted gradient-echo imaging in phantoms at 4.7 T.

The resonance frequencies of lipids are not temperature dependent and have an average offset of 3.5 ppm with respect to the water resonance. Lipid signals affect image phase, and thus cause errors in the calculated temperature maps. Such errors are difficult to predict beforehand, since they depend on fat content, echo time, spectrometer reference frequency and temperature. Therefore, lipid signals should be suppressed to assure accurate temperature mapping. In chapter 5, a binomial spectral-spatial pulse in combination with local shimming of the target zone is proposed for lipid suppression. The spectral-spatial pulse selectively excites water hydrogens, in addition to being spatially selective due to simultaneous execution of field gradients. A binomial pulse was chosen for its small time penalty (approximately 2 msec at 1.5 T field strength). In combination with echo shifting, fast, lipid-suppressed, temperature mapping has been demonstrated during in vivo FUS heating in rat thigh muscle tissue at 4.7 T with a standard deviation of 0.37°C, and with a temporal resolution of 438 msec.

None of the MR temperature mapping methods discussed in this thesis permit calculation of absolute temperature. Typically, a reference image, acquired before the start of the hyperthermia procedure, is used. This makes MR thermometry methods highly motion sensitive. Artifacts in the obtained temperature maps not only originate during the acquisition of an image from irregular scanning of k-space, but also arise from the use of an incorrect spatial reference. Since reliable MR temperature data should be available on-line to allow control of the hyperthermia device on the basis of the measured temperature evolution in the target tissue, on-the-fly motion evaluation is important. A method for on-line displacement correction of MR images is presented in chapter 6, based on the cyclic navigator echoes. An alternative approach for the calculation of phase difference images is proposed, which is exploited for displacement correction. Instead of direct calculation of phase difference images with respect to a reference image (typically the first image of a series of dynamics), the phase difference between successive images is calculated. Summing of these phase difference images leads again to the phase difference with respect to the reference image, but problems related to the periodicity of phase are reduced. Navigator data are analysed on-line, based on matching of the profiles with a reference profile. If a displacement is detected that exceeds a predefined threshold (typically three times the standard deviation of displacement detection, about one-fourth of the voxel-size), motion correction is applied automatically, based on the regridding of the available subtotal of phase difference images, to which subsequent phase difference maps are added. The method was validated on meat-samples which were displaced manually, leading to motion detection with an accuracy of about 0.02 mm, and correct calculation of temperature maps after displacement.

The two chapters that follow describe the development of mechanisms that exploit MR temperature data for the control of focused ultrasound during the hyperthermia procedure. Chapter 7 describes the establishment of a link between the MR and ultrasound devices, which allows, in combination with on-line analysis of MR data, automatic control of the hyperthermia intervention. A more accurate control mechanism is described in chapter 8, based on a physical model of heat deposition and heat flow. It should be noted that these control methods can be used for any form of MR-controlled local hyperthermia, whatever the heating mechanism is.

Most of the current hyperthermia investigations target non- or less-invasive ablation of tissue, aiming to completely destroy diseased tissue without damaging nearby healthy tissue. In several studies, the effect of the applied temperature evolution is evaluated using an empirical formula which calculates the applied thermal dose. This formula, described in literature in the eighties, describes the non-linear relationship between the product of time of exposure and temperature on cell death. In the work described in chapter 10, experiments were carried out in which necrosis estimates, calculated on the basis of MR thermometry data using the thermal-dose equation, were compared to histological findings. These experiments were performed on rat thigh muscle tissue in vivo. The experiments indicate that general correspondence between thermal dose and cell death exists. Surrounding the focal point, scattered necrosis spots are found at a scale much smaller than both the FUS focal point diameter and the spatial resolution of MR images. This effect might be due to variations in perfusion or temperature sensitivity, and should be further investigated.

Chapter 11 demonstrates that it is feasible to locally induce expression of endogenous heat-shock proteins upon application of FUS, monitored by MRI. Based on these findings, chapter 12 describes experiments in which an exogenous gene, under control of a heat-sensitive promotor, is brought to expression in transgenic tumors in vivo using FUS under MR control. Preliminary results suggest that a certain thermal dose should be exceeded in order to induce gene expression. Additional experiments are needed to investigate the correspondence between spatial variations in temperature and gene expression, taking into account local variations in tumor physiology.

Liposomes have been proposed as a vehicle for drug transportation. Directing the liposomes to the target site and inducing local release of their contents has been found difficult to achieve. Local hyperthermia has been proposed for drug release from liposomes, exploiting a change in membrane permeability when liposomes pass through their liquid-crystalline transition temperature. In this thesis, the feasibility of local release from temperature-sensitive liposomes, induced using FUS, monitored by MR temperature imaging, has been investigated using temperature sensitive liposomes, filled with a gadolinium MR contrast agent. Upon heating of the liposomes to approximately 42°C, their liquid-crystalline transition temperature, local release of gadolinium has been demonstrated, thus providing proof of principle that local release of small molecules from liposomes is feasible with MR-controlled hyperthermia.

The thesis is concluded with a discussion of issues which remain to be investigated to further improve reliability of PRF-based MR temperature imaging for medical applications, comprising: (a) effects of temperature dependent changes in volume susceptibility on thermometry; (b) feasibility of volume-selective temperature imaging; and (c) phased-array FUS transducers.

# Résumé

Cette thèse décrit des développements méthodologiques en imagerie par résonance magnétique (IRM) de température et en traitement de ces données, elle a pour but d'augmenter la vitesse et la fiabilité de l'IRM de température pour le contrôle et le monitorage de l'hyperthermie in vivo. Des études de faisabilité ont été réalisées pour étudier l'adéquation de l'hyperthermie sous contrôle d'IRM de température avec trois applications médicales potentielles: (a) l'ablation thermique du tissu; (b) l'induction locale de l'expression des gènes sous contrôle d'un promoteur sensible à la chaleur; et (c) l'induction de la libération locale d'une substance à partir des liposomes thermo-sensibles.

En introduction de cette thèse ces trois applications sont décrites (chapitre 1), suivie par une introduction de l'IRM de température (chapitre 2) et des ultrasons focalisés (chapitre 3) qui sont la méthode utilisée pour induire une hyperthermie dans les expériences décrites dans cette thèse.

La thermométrie par IRM peut être basée sur le décalage de la fréquence de résonance des protons de l'eau en fonction de la température. Un décalage en fréquence de résonance, résultant d'un changement de température, peut être cartographié en utilisant l'information de phase dans des images d'écho de gradient "RF-spoiled". Une image de référence est utilisée pour compenser les autres facteurs qui contribuent à la phase dans l'image, comme l'homogénéité du champ magnétique. Pour une augmentation de température donnée, la différence de phase mesurée augmente avec le temps d'écho (TE) de l'expérience. Par contre, le rapport signal sur bruit des images de phase diminue exponentiellement avec une constante de temps $T_2^*$. On peut en déduire que la sensibilité optimale pour la température existe quand le TE est égal à $T_2^*$. En IRM conventionnelle le TE est inférieur au temps de répétition (TR) de l'expérience, un compromis entre imagerie rapide (TR court) et sensibilité pour la température (TE relativement long, $\sim T_2^*$) est donc nécessaire. Le chapitre 4 décrit comment un décalage d'écho (echo shifting), qui permet la formation des échos de gradient un ou plusieurs TR après l'excitation du signal (donc: TE > TR), peut être utilisé pour l'imagerie rapide avec un TE qui engendre une sensibilité optimale pour la température. Des mesures de température ont été réalisées à 4,7 T sur des fantômes en utilisant l'imagerie en écho gradient décalé, avec un écart-type de 0,1-0,2°C, une résolution temporelle de 144 msec et une résolution spatiale de 0,55 mm.

Les fréquences de résonance des lipides ne dépendent pas de la température et ont un décalage moyen de 3,5 ppm par rapport à la résonance de l'eau. Les signaux des lipides affectent la phase de l'image et causent donc des erreurs dans les cartes de température. Ces erreurs sont difficilement prédictibles, car elles dépendent de la quantité de graisse, du temps d'écho, de la fréquence de résonance du spectromètre et de la température. C'est pour cela que les signaux des lipides doivent être supprimés pour assurer une imagerie de température fiable. Dans le chapitre 5, une impulsion binomiale spectrale-spatiale en combinaison avec une homogénéisation locale du champ magnétique est proposée pour la suppression des lipides. A côté d'être spatialement sélective grâce à une exécution simultanée avec des gradients de champs, l'impulsion spectrale-spatiale excite sélectivement les noyaux d'hydrogènes de l'eau. Une impulsion binomiale a été choisie pour sa courte durée (approximativement 2 msec à un champs de 1,5 T) en combinaison avec l'acquisition du décalage d'écho. Cela permet de démontrer la faisabilité de la cartographie de température rapide avec suppression des lipides pendant le chauffage aux ultrasons focalisés in vivo dans le muscle d'une cuisse de rat à 4,7 T, avec un écart-type de 0,37°C et une résolution temporelle de 438 msec.

Aucune des méthodes de cartographie de température discutées dans cette thèse permet de calculer la température absolue. En général une image de référence, acquise avant le début de l'hyperthermie, est utilisée. Ceci rend l'imagerie de température fortement sensible aux mouvements. Des artefacts dans les cartes de température obtenues n'apparaissent pas seulement pendant l'acquisition irrégulière de l'espace-k, mais aussi à cause de l'usage d'une référence spatiale incorrecte. Depuis que l'imagerie de température en temps réel est nécessaire pour le contrôle d'hyperthermie à partir de la température mesurée dans le tissu, l'évaluation des mouvements en temps réel devient importante. Une méthode pour la correction des mouvements en temps réel est présentée au chapitre 6, basée sur des échos de navigateur cyclique. Une méthode alternative pour calculer des cartes de différence de phase a été proposée et exploitée pour la correction des mouvements. Au lieu de calculer la différence de phase par rapport à l'image de référence (généralement la première image d'une série de dynamiques), la différence de phase entre des images successives est calculée. Par sommation de ces cartes de différence de phase, la différence de phase par rapport à la référence est de nouveau obtenue, mais les problèmes liés à la périodicité de phase sont réduits. Les échos navigateurs sont analysés en temps réel grâce à une comparaison des profils avec un profil de référence. Quand un déplacement détecté dépasse un seuil prédéfini (typiquement trois fois l'écart-type de la détection de mouvement, c'est à dire approximativement un quart de la taille d'un voxel), la correction des mouvements est appliquée automatiquement, basée sur un recalage de la somme actuelle de la différence de phase à laquelle on rajoute les différences de phase qui suivent. Cette méthode a été validée sur des morceaux de viande qui ont été déplacés manuellement. La détection de mouvements a été validée avec un écart-type de 0.02 mm, et les cartes de température sont calculées correctement indépendamment des déplacements.

Les deux chapitres suivants décrivent le développement des mécanismes de contrôle qui exploite les données d' IRM par température pour gérer les ultrasons focalisés appliqués pendant l'hyperthermie. Le Chapitre 7 décrit l'établissement d'un lien entre l'IRM et les appareils qui génèrent les ultrasons, permettant, en combinaison avec l'analyse des données IRM en temps réel, un contrôle automatique de l'intervention. Un mécanisme de contrôle plus précis est décrit au chapitre 8. Ce mécanisme est basé sur un modèle physique de déposition et de flux de chaleur, ces méthodes sont capables de contrôler l'hyperthermie locale indépendamment du générateur d'hyperthermie.

La plupart des recherches effectuées sur les applications de l'hyperthermie proposent une ablation moins invasive pour cibler la destruction du tissu bénin sans affecter le tissu sain à proximité. Dans plusieurs de ces études, l'effet de l'évolution de la température donnée est évalué en utilisant une formule empirique pour calculer la dose thermique appliquée. Cette formule, présentée dans les années 80, décrit la relation non-linéaire entre la mort cellulaire et le produit temps d'exposition-température. Le travail décrit dans le chapitre 10 discute des expériences où les estimations des doses thermiques, basées sur des données IRM de température, ont été comparées avec des données histologiques. Ces expériences ont été réalisées in vivo dans le muscle d'une cuisse de rat. Les expériences indiquent une correspondance générale entre la dose thermique et la mort cellulaire. Autour du point focal, des régions nécrosées sont dispersées sur une échelle largement inférieure à la taille du point focal et à la résolution spatiale des cartes de température. Cet effet lié peut-être aux variations de la perfusion locale ou à une sensibilité différente du tissu pour la température, doit être étudié plus en détail.

Le chapitre 11 démontre la faisabilité de l'induction locale de l'expression des protéines de choc thermique endogène, grâce à l'application des ultrasons focalisés sous monitorage par IRM. A la base de ces résultats le chapitre 12 décrit des expériences qui montrent l'induction in vivo de l'expression dans une tumeur transgénique d'un gène exogène sous contrôle d'un promoteur thermo-sensible en utilisant des ultrasons focalisés sous contrôle d'IRM de température. Les résultats préliminaires suggèrent qu'une certaine dose thermique minimale est nécessaire pour induire l'expression. Des expériences additionnelles sont nécessaires pour examiner la correspondance entre les variations spatiales de température et l'expression génétique, prenant en compte les variations locales dans la physiologie de la tumeur.

Des liposomes ont été proposés comme véhicule pour le transport des médicaments. Le guidage des liposomes vers la cible et l'induction de libération locale du contenu est généralement difficile. L'hyperthermie locale a été proposée pour la libération des médicaments, exploitant un changement de la perméabilité de la membrane qui apparaît quand le liposome traverse sa température de transition liquide-cristalline. Dans cette thèse, la faisabilité de la libération locale des molécules à partir des liposomes thermo-sensibles contenant un agent de contraste IRM a été étudiée. La libération se fait sous contrôle des ultrasons focalisés avec monitorage par IRM de température. Quand les liposomes ont été chauffés à 42°C, leur température de transition liquide-cristalline, il s'en suit une libération locale de gadolinium qui montre qu'une telle libération de petites molécules à partir des liposomes est réalisable avec hyperthermie sous contrôle d'IRM.

Cette thèse est conclue par une discussion sur les investigations à mener pour améliorer encore la fiabilité de l'imagerie de température basée sur la fréquence de résonance des protons d'eau, à savoir: (a) les effets des changements de la susceptibilité volumique sur l'imagerie de température; (b) la faisabilité d'imagerie d'une volume spécifique; et (c) les transducteurs ultrasons en réseau.

# Samenvatting

In dit proefschrift worden ontwikkelingen op het gebied van MR temperatuurimaging methodologie en MR dataverwerking beschreven, die verhoging van de snelheid en betrouwbaarheid van MR temperatuurimaging voor de controle en observatie van hyperthermie interventies in vivo beogen. Studies werden uitgevoerd om de toepasbaarheid van door middel van MR temperatuurimaging gecontroleerde hyperthermie voor drie medische toepassingen te onderzoeken: (a) thermische ablatie van weefsel, (b) locale inductie van de expressie van genen onder controle van een warmtegevoelige promotor, en (c) de inductie van gecontroleerde locale afgifte van medicamenten uit warmtegevoelige liposomen.

In de introductie worden allereerst deze drie toepassingen beschreven (hoofdstuk 1), gevolgd door een introductie van MR temperatuurimaging (hoofdstuk 2) en gefocuseerde ultrasound (FUS) (hoofdstuk 3), de techniek waarmee hyperthermie werd geïnduceerd in de experimenten die in dit proefschrift zijn beschreven.

MR-thermometrie kan worden gebaseerd op de temperatuursafhankelijkheid van de resonantiefrequentie van protonen in water (PRF). Een verschuiving in resonantiefrequentie ten gevolge van een temperatuursverandering kan worden afgebeeld door gebruik te maken van de faseinformatie in zogenaamde RF-spoiled gradiënt-echo images. Met behulp van een referentieimage worden andere fasebijdragen gecompenseerd, bijvoorbeeld gerelateerd aan de homogeniteit van het magnetische veld. Voor een gegeven temperatuurstijging neemt het gemeten faseverschil lineair toe met de echotijd (TE) van het experiment. Daarentegen neemt de signaal-ruisverhouding exponentieel af met een tijdconstante $T_2^*$. Hieruit kan worden afgeleid dat optimale temperatuursgevoeligheid bestaat wanneer de TE gelijk is aan $T_2^*$. In conventionele gradiënt-echo MR imaging is de TE kleiner dan de repetitietijd (TR) van het experiment. Een compromis tussen snel imagen (korte TR) en optimale temperatuursgevoeligheid (relatief lange TE, $\sim T_2^*$) is daarom noodzakelijk. Hoofdstuk 4 beschrijft hoe echoverschuiving ("echo shifting"), waarbij gradiënt-echo's één of meerdere TR periodes na hun excitatie worden gevormd (dus: TE $>$ TR), kan worden gebruikt voor snelle temperatuursimaging met een TE die tot optimale temperatuursgevoeligheid leidt. Temperatuurmetingen met een standaardafwijking van 0,1-0,2°C, een tijdresolutie van 144 msec en een ruimtelijke resolutie van 0.56 mm zijn aangetoond in fantomen bij 4,7 T.

De resonantiefrequenties van lipiden zijn niet temperatuurafhankelijk en hebben een gemiddelde verschuiving van 3,5 ppm ten opzichte van de waterresonantie. Lipidesignalen beinvloeden de fase van het image en veroorzaken daardoor fouten in de berekende temperatuurmappen. Deze fouten zijn moeilijk voorspelbaar omdat ze afhangen van het vetpercentage, de echotijd, de referentiefrequentie van de MR apparatuur en de temperatuur. Lipidesignalen moeten daarom worden onderdrukt om de temperatuurverdeling nauwkeurig in kaart te kunnen brengen. In hoofdstuk 5 wordt een binomiale spectraal-ruimtelijke puls in combinatie met locale veldhomogenisatie voorgesteld ter onderdrukking van het lipidesignaal. De spectraal-ruimtelijke puls slaat selectief waterprotonen aan en is tevens ruimtelijk selectief door simultane toepassing van veldgradiënten. De keuze voor een binomiale puls werd gemaakt op grond van zijn geringe “timepenalty” (ongeveer 2 msec bij 1,5T). In combinatie met echo shifting is snelle, vetonderdrukte temperatuurimaging met een standaardafwijking van 0,37°C en een tijdresolutie van 438 msec aangetoond tijdens in vivo FUS-verhitting in de dijbeenspier van ratten bij 4.7 T.

Geen van de in dit proefschrift besproken temperatuurimagingmethodes maakt het mogelijk absolute temperatuurmetingen te verrichten. Gewoonlijk wordt een referentie-image gebruikt die is opgenomen voor de start van de hyperthermie-procedure. Hierdoor zijn MR temperatuurmetingen erg bewegingsgevoelig. Afwijkingen in de verkregen temperatuurmappen ontstaan niet alleen tijdens acquisitie van een image doordat k-ruimte onregelmatig wordt opgenomen, maar tevens door het gebruik van incorrecte ruimtelijke referentie. Betrouwbare MR temperatuurdata moeten direct beschikbaar zijn om, op basis van de gemeten temperatuurinformatie, controle van het hyperthermie-instrument mogelijk te maken. Hierdoor is “on-the-fly” evaluatie van beweging belangrijk. Een methode voor de “on-line” correctie van beweging in MR images, die is gebaseerd op cyclische navigator-echo’s, is voorgesteld in hoofdstuk 6. Een alternatieve benadering voor het berekenen van fase-images wordt geintroduceerd, waarvan gebruik wordt gemaakt tijdens bewegingscorrectie. In plaats van het direct berekenen van het faseverschil met betrekking tot het referentie-image (normaal gesproken het eerste image uit een serie dynamische scans) wordt het faseverschil tussen opeenvolgende images berekend. Optelling van deze faseverschilmappen leidt opnieuw tot het faseverschil met betrekking tot de referentie. Problemen ten gevolge van de periodiciteit van de fase worden echter verminderd. Navigator-data worden on-line geanalyseerd, gebaseerd op een vergelijking van de profielen met een referentie-profiel. Wanneer een beweging wordt gedetecteerd die een vooraf bepaalde grenswaarde overschrijdt (normaal gesproken drie maal de standaardafwijking, ongeveer eenvierde deel van de voxelafmeting), wordt bewegingscorrectie automatisch toegepast op basis van het verschuiven van de beschikbare subtotaal faseverschilmap, waarbij daarna de erop volgende faseverschilmappen worden opgeteld. De methode werd geëvalueerd met handmatig verplaatste vleesmonsters, waarbij beweging gemeten werd met een nauwkeurigheid van ongeveer 0.02 mm terwijl temperatuurmappen ook na beweging correct werden berekend.

De twee hoofdstukken die hierop volgen beschrijven de ontwikkeling van technieken die tijdens de hyperthermieprocedure, gebruikmakend van MR temperatuurdata, de gefocuseerde ultrasound controleren. Hoofdstuk 7 beschrijft de totstandkoming van een verbinding tussen de MR- en de ultrasound-apparatuur, waardoor, in combinatie met de on-line analyse van MR data, automatische controle van de hyperthermie-interventie mogelijk werd. Een nauwkeuriger controlemechanisme wordt beschreven in hoofdstuk 8, dat is gebaseerd op een fysisch model van hittedepositie en warmtespreiding. Hierbij moet worden opgemerkt dat deze controlemechanismen kunnen worden toegepast bij iedere mogelijke vorm van MR-gecontroleerde hyperthermie, onafhankelijk van het toegepaste verhittingsmechanisme.

De meeste van de huidige onderzoeken naar hyperthermie hebben niet- of minder-invasieve weefselablatie voor ogen. In verscheidene studies wordt het effect van de toegepaste temperatuurevolutie geëvalueerd met behulp van een empirische formule die de toegepaste thermische dosis berekent. Deze formule, in de literatuur beschreven in de jaren tachtig, beschrijft de nietlineaire relatie tussen celdood en het product van exposieduur en temperatuur. In het werk dat wordt beschreven in hoofdstuk 10, werden experimenten uitgevoerd waarin necroseschattingen, die op basis van MR-thermometrische data werden berekend met behulp van de thermische dosisformule, vergeleken met histologische bevindingen. Deze experimenten werden uitgevoerd op dijbeenspierweefsel in ratten in vivo. De experimenten wijzen op een algemene overeenkomst tussen thermische dosis en celdood. Rondom het focus werden verspreide necrosispunten aangetroffen, die afmetingen hebben op een schaal die klein is ten opzichte van zowel de FUS-focaaldiameter als de ruimtelijke resolutie van de MR beelden. Dit effect kan een gevolg zijn van verschillen in perfusie of temperatuurgevoeligheid, waarnaar nader onderzoek vereist is.

Hoofdstuk 11 toont aan dat het mogelijk is om door middel van FUS-hyperthermie, in beeld gebracht door MRI, lokaal expressie van endogene hitteschokeiwitten te induceren. Op basis van deze bevindingen worden in hoofdstuk 12 experimenten beschreven waarbij een exogeen gen, dat onder controle staat van een soortgelijke hittegevoelige promotor, tot expressie is gebracht in transgene tumoren in vivo. Hierbij wordt gebruik gemaakt van MR-gecontroleerde FUS. Initiële experimenten suggereren dat een bepaalde thermische dosis moet worden overschreden om genexpressie te induceren. Aanvullende parameters zijn vereist om de overeenkomst tussen ruimtelijke temperatuursvariaties en genexpressie te onderzoeken, waarbij locale variaties in tumorfysiologie moeten worden betrokken.

Het gebruik van liposomen als transporteur van medicamenten is reeds voorgesteld. Het dirigeren van de liposomen naar de beoogde locatie en het aldaar induceren van locale afgifte van medicamenten blijkt echter moeilijk. Locale hyperthermie is voorgesteld om dit te bewerkstelligen, daarbij gebruikmakend van een verandering in membraanpermeabiliteit die optreedt wanneer liposomen hun vloeistof-kristallijn-overgangstemperatuur overschrijden. In dit proefschrift wordt de mogelijkheid van locale gadolinium MR-contrastmiddelafgifte uit temperatuurgevoelige liposomen onderzocht, die geïnduceerd is met FUS en in beeld gebracht met MR temperatuurimaging. Er werd aangetoond dat locale afgifte van gadolinium optreedt wanneer deze liposomen werden verhit tot ongeveer 42°C, hun vloeistof-kristallijn-overgangstemperatuur. Dit bewijst dat locale afgifte van kleine moleculen uit liposomen mogelijk is met MR-gecontroleerde hyperthermie.

Dit proefschrift wordt afgeloten met een discussie aangaande kwesties die nader onderzocht dienen te worden om de betrouwbaarheid van op PRF-gebaseerde MR temperatuurimaging voor medische doeleinden te vergroten, waaronder: (a) effecten van temperatuursafhakelijke veranderingen in volume susceptibiliteit op thermometrie; (b) de mogelijkheid van volumeselectieve excitatie; en (c) “phased-array” FUS transducers.